QUEENSLAND WATER MODELLING NETWORK

Climate change and variability

Between a hot place and hypoxia:

Modelling fish-kill risk in Queensland waterholes

Final Report

For Queensland Water Modelling Network

Queensland Government

The Queensland Water Modelling Network (QWMN) is an initiative of the Queensland Government that aims to improve the state's capacity to model its surface water and groundwater resources and their quality. The QWMN is led by the Department of Environment and Science with key links across industry, research and government.

Citation

Zhai, SY., Huang, P., Marshall, JC., Lobegeiger, J., Cramp, RL., Parisi, MA., McPhee, DL., Franklin, CE., Prior, A., Kurucz, K., Hipsey, MR., 2022. Between a hot place and hypoxia: Modelling fish-kill risk in Queensland waterholes. Report prepared for the Queensland Water Modelling Network, Department of Environment and Science, Queensland Government, Brisbane, Australia.

Executive Summary

Dryland rivers that cease to flow for extended periods and exist as disconnected waterholes are widespread throughout the world's arid and semi-arid regions. These waterholes provide critical aquatic habitats and serve as refugia during drought disturbances. However, the quality of these waterholes can often be severely compromised by hypoxic conditions which, when combined with adverse weather conditions, can lead to mass fish kills and loss of biodiversity.

Led by The University of Western Australia in collaboration with The University of Queensland and the Queensland Department of Environment and Science, this project sought to develop new modelling capability to identify risks to fish occupying waterhole refuges and to support appropriate management responses. Existing models used for river management have not been designed to resolve the subtle but important variability in water stratification which determines how periods of low-oxygen (hypoxia) develop.

In this study, we developed a river waterhole-scale ecohydrology model using the open-source General Lake Model (GLM) coupled with the Aquatic Ecodynamics (AED) water quality model for modelling thermal stratification and dissolved oxygen regimes during prolonged drought periods in the northern Murray-Darling Basin rivers in Queensland, Australia. The model was tested through application to six waterholes in the Condamine-Balonne and Moonie rivers where thermistor and oxygen chains were deployed to collect high-resolution data-sets.

The models were tailored to take into account weather and river conditions in order to predict when low oxygen events occur and for how long. Simulations in all six waterholes successfully predicted the prolonged stratification and hypoxia in these shallow waterholes. The degree of local wind-sheltering and solar-shading in each site was found to be important in capturing individual waterhole dynamics.

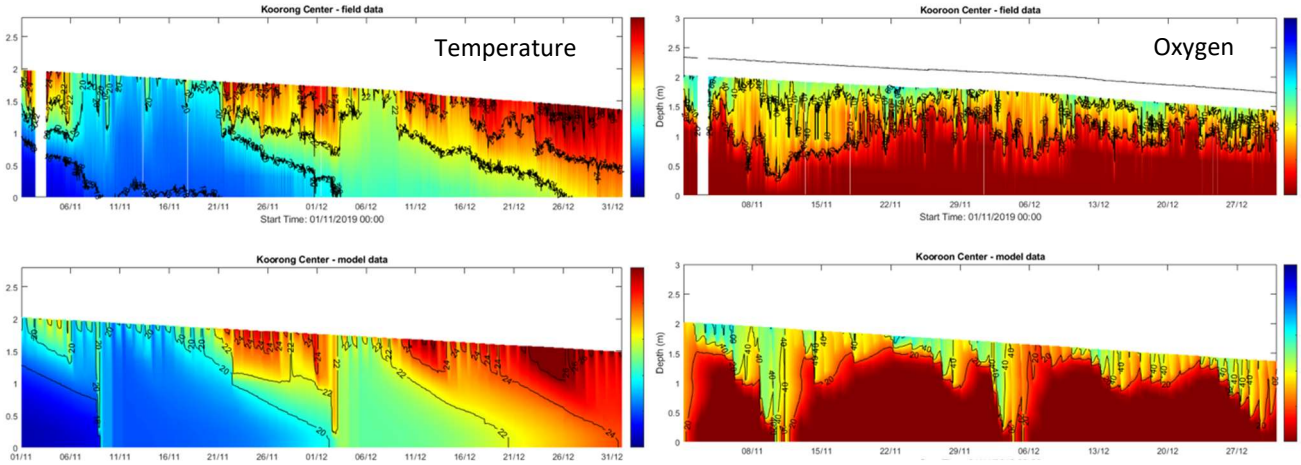

Example of measured waterhole temperature and oxygen data (top) and the GLM-AED model predictions (bottom).

As different fish species have variable sensitivity to environmental conditions, we sought to extend the model to provide an estimate of habitat quality. Therefore, in order to understand the threshold levels of oxygen fish can tolerate, we undertook a series of physiological tests on several major fish species typical of the region (carp, Murray cod, Bony bream and Golden perch) in the laboratory. This created a dataset of critical temperature and oxygen limits (including interactive effects) for the selected species.

By combining the laboratory data and our waterhole model predictions of temperature and oxygen, we developed a new *fish habitat index* quantifying the degree to which the water at any given time is within a suitable range for fish metabolism. This was used to estimate how the "habitable volume" changes over time for each waterhole (Fig. 4). Results indicated considerable variations in habitat conditions between sites and through time, and were used to infer fish-kill risks under given environmental conditions. An increased risk of a fish-kill event occurs when the habitable volume of a waterhole gets reduced to a critically low level. This is linked to specific patterns in weather conditions and hydrology.

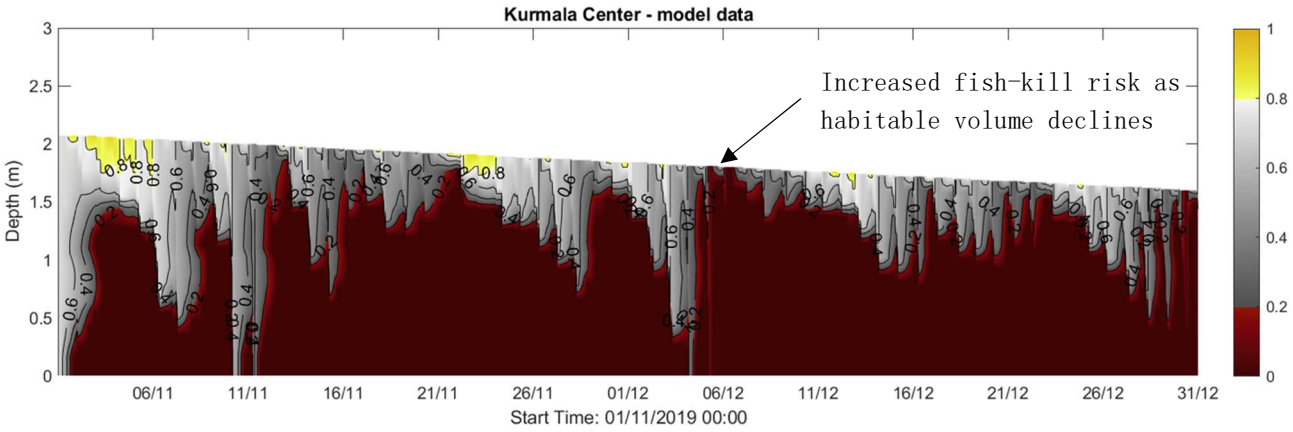

Waterhole habitat condition categorised into marginal (red), suitable (grey), and optimal (yellow).

The habitable volume was shown to be different for each species, and concerningly carp were found to be the most tolerant of poor water quality conditions and native species were more likely to suffer from rapid reductions in habitat volume, which could lead to fish-kill events.

Overall, the project has provided new thermal and acute hypoxia tolerance threshold data for three key native fish species and the highly invasive Carp. While the upper maximum thermal tolerances of all species were well above those recorded in the natural waterholes, the very low dissolved oxygen levels recorded the field has the potential to push the native fish species (but not carp) close to their minimum tolerable oxygen limits, particularly in warmer waters. Importantly, waterhole oxygen data and predictions showed that for most of the available volume, waterholes were highly hypoxic, being ≤2 mgL^{-1} DO (25% air saturation) for extended periods of time, resulting in very low habitat quality indices. Future work to extend the approach to be able to account for chronic hypoxia exposure histories within waterholes, and important fish behavioural adaptations is recommended.

In the last part of the study we present a conceptual framework outlining the ways waterholes will be impacted by a warming climate. For a selected example waterhole and climate change forecast, the model was then used to illustrate the mechanisms by which climate change will alter waterhole stratification regimes and hypoxia frequency. This analysis showed that habitat quantity and quality for all studied species is expected to decrease under the anticipated future climate, with increased risks of fish-kill events for native species during drought as habitable volume falls to zero more frequently.

The model and assessment approach developed here is a first step towards building a reliable tool that managers can use for assessment of waterhole hypoxia and fish-kill risks. Recommendations for how future applications of the model can help to inform future water management decisions and climate adaptation strategies are provided.

Table of Contents

1. Introduction

1.1. Dryland rivers, drought and hypoxia

Fish populations in dryland rivers, such as many of those in the northern Murray-Darling Basin, are subject to frequent hydrological drought disturbances (Marshall et al., 2021). Flow stops and most of the river channels dry, with remaining water restricted to deeper, in-channel features, commonly termed waterholes (Knighton and Nanson, 2000). During these drought disturbance events, fish populations resist drought by utilising waterholes as drought refugia. After drought breaks with the return of flow, fish dispersal, reproduction and recruitment (and possibly artificial fish stocking) allow surviving fish to repopulate denuded river reaches making their populations resilient. The high prevalence of drought disturbances in dryland rivers means that fish populations frequently cycle through periods of resistance conferred by refugia and resilience conferred by dispersal, reproduction and recruitment. Both resistance and resilience are prerequisites for continuing fish population viability (Marshall et al., 2016).

The longer a drought continues, the fewer waterholes persist, meaning that fish population resistance diminishes over time. Theoretically, the fewer refuge waterholes available to support regional populations of fish during drought, the greater is the risk of regional extinctions (Bond *et al*., 2015, Figure 1). The hydrological drought from 2018-January 2020 was one of the longest periods, (in some rivers the longest), without river flow on record for many northern MDB rivers. Evaporative water loss and the lack of inflow meant availability of waterholes as drought refugia was very limited. Furthermore, the quality of these refugia was severely compromised by hypoxic to anoxic conditions, exacerbating as they contracted with increasing drought duration (Figure 2). This compromised fish population resistance, with likely local to regional scale extinctions (Negus, 2019).

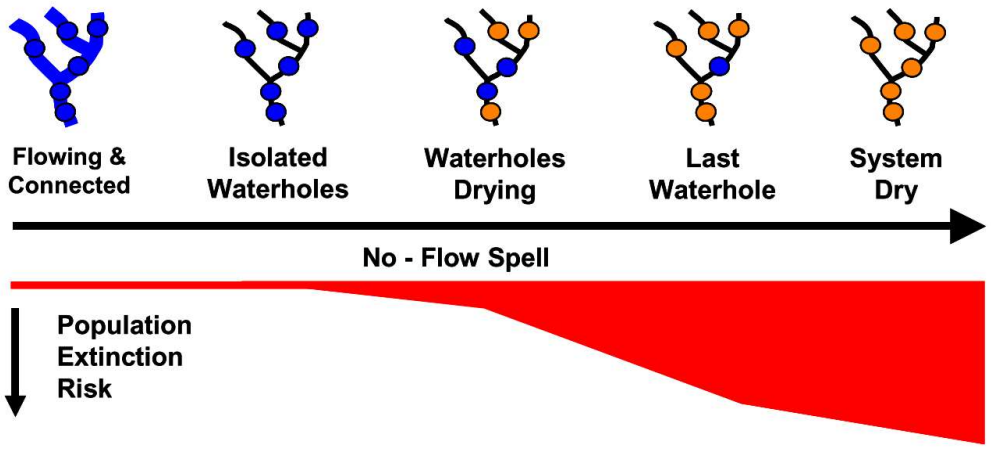

Figure 1: The longer a spell without river flow continues in dryland rivers, the fewer refuge waterholes persist and the greater is the risk of regional extinctions of fish populations.

From mid-January 2020 flow returned to many MDB rivers following widespread rainfall, ending a long hydrological drought (Figure 3). The 'first flush' of new flow caused prolonged anoxia in persisting waterholes (Figure 2), acting as a classic 'blackwater event'. Anoxia results from the mobilisation of dissolved organic carbon accumulated during drought, and subsequent bacterial respiration as they feed on this carbon, utilising all available dissolved oxygen (King *et al*., 2012). The associated input of nutrients associated with flow events and their subsequent accumulation in and re-release from sediments further elevates anoxia risk by fuelling

algal blooms that cause an imbalance of diel oxygen cycles. Any fish that survived the drought may not survive these conditions.

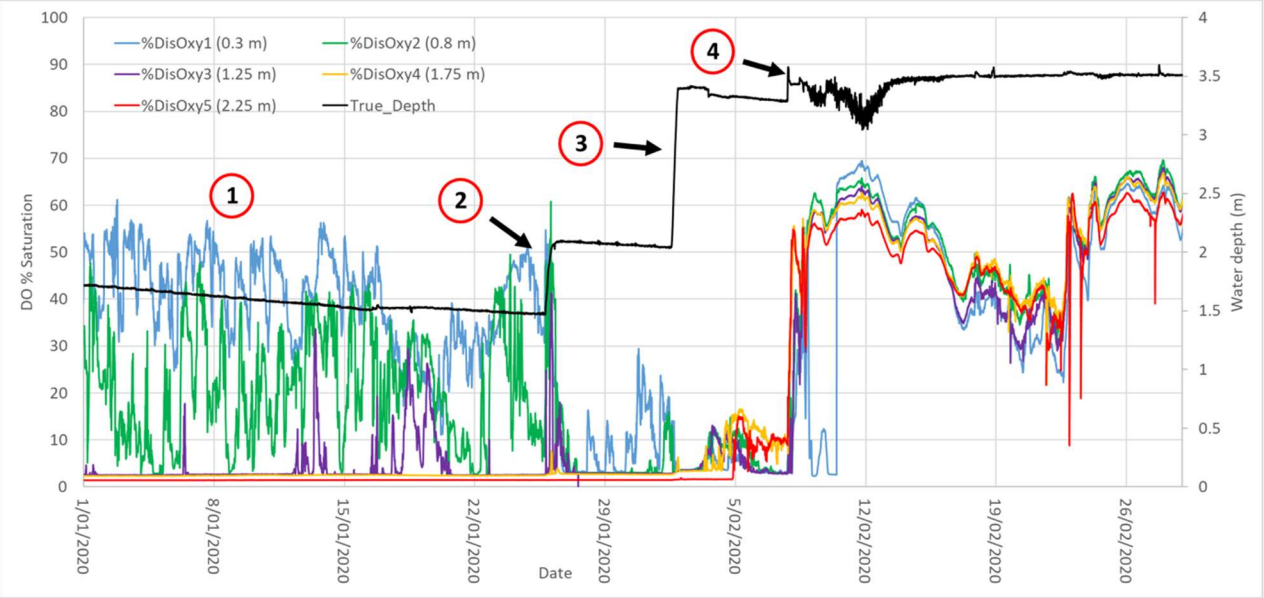

Figure 2: Dissolved oxygen (DO) saturation profile for Kooroon Waterhole in the Moonie River from January-February 2020. The black line indicates water depth and coloured lines DO at different depths indicated in the figure legend. Period 1 represents the end of a long period without flow. Dissolved oxygen is low and variable and stratification is pronounced. Period 2 has increase in water depth but no river flow (i.e. inflow but no outflow) and no mixing. Dissolved oxygen crashes, probably associated with a black water event. Period 3 represents the first small flow event that lasted several days and resulted in mixing. Dissolved oxygen crashes, probably associated with a black water event. Period 4 represents the commencement of a larger, sustained flow event. Dissolved oxygen recovers but remains low and stratification recommences.

1.2. Assessing fish-kill risk

The impacts of anoxia upon fish in dryland river waterholes was graphically demonstrated by the well-publicised, mass fish kills in the Darling River in northern New South Wales over the summer of 2018-2019. These events were caused by the combined influences of drought, waterhole stratification, extreme heatwaves and possible local weather impacts, resulting in rapid and prolonged anoxia (Vertessy *et al*., 2019). Climate change threatens to increase the frequency and severity of extreme events like droughts and heat waves in the dryland rivers of the northern MDB (MDBA, 2019), though as yet it remains unclear to what extent these changes will impact upon the quality of waterhole refugia and their role in maintaining viable native fish populations. As a response to the issue, WaterNSW have developed a Fish Health Risk Indicator using real-time river flow, stream depth, algal biomass and predicted temperature/weather changes to infer the conditions that could lead to mass fish deaths (Davie and Pera, 2022). However, to date no mechanistic based models have been developed able to reliably resolve the key interactions between hydrology, oxygen and fish kill likelihood.

The objective of this project is to develop a new modelling capability for assessing the responses of dissolved oxygen regimes in refuge waterholes during periods without flow, the influences of varied hydrologic and weather conditions, and the threats this might pose to the fish which rely upon these waterholes for their survival. This modelling capacity can be used to help plan for future adaptation strategies.

To date, modelling of river dynamics focuses on capturing the flows and floods; that is, they seek to capture how much water propagates downstream following rainfall events or flow releases. Models used for this purpose include Source, MIKE-FLOOD, TUFLOW and MDBA's BIGMOD. Traditionally, the low flow dynamics

are usually poorly resolved in river or catchment modelling activities and river waterholes are considered predominantly as a storage, or transmission loss, that must be filled before water can progress downstream. This is of course necessary given the demands for water accounting and supporting water allocation activities, however, this means that as the river transitions from lotic (riverine) to lentic (lacustrine), the waterhole dynamics remain largely unresolved. For example, for the rivers of the Queensland MDB, a threshold of 5 ML/day has been applied to represent cessation of flow in model outputs (e.g. DES, 2018), and the better representation of zero flow is a recognised science need for better water planning in Queensland (Anon, 2014).

Figure 3: Photo of MDB Moonie River waterhole, and end-stage fish-kill.

1.3. Project aims and scope

In this project we aimed to build upon recent work linked to the National Carp Control Plan (NCCP, 2020) water quality risk-assessment modelling (Brookes and Hipsey, 2019), to fill the capability gap in our current modelling toolkit, and produce a flexible and adaptable river waterhole ecohydrology model. To this end, we created a river-reach and waterhole-scale implementation of the 1D (vertical) GLM linked with the AED water quality model. This approach is suitable for waterhole-scale research as during dry conditions the vertical stratification is the key hydrologic feature shaping the deoxygenation events.

During the NCCP assessment, we trialled applying vertically resolved models to river reaches and wetlands within the MDB with some success simulating water flow and floodplain inundation, water temperature and oxygen (Brookes and Hipsey, 2019). Whilst the model was run in 3D, to resolve vertical stratification, the focus was not on waterhole stratification, and there was limited data available from inland river waterholes by which the model could be assessed in detail (Figure 4). We have also undertaken assessments of river pool dynamics in Fitzroy River in the Kimberley region of Western Australia (Gleiss *et al*., 2021), and have developed advanced simulations of stratification and diurnal oxygen dynamics in several shallow lakes in Perth (Vilas *et al*., 2017; Lui *et al*., 2020).

The aim of this project was the model waterhole hypoxia and fish habitat condition in six waterholes within Queensland which have recently been intensively monitored by the Queensland Government (DES and DNRME), and for which bathymetry is available. The study objectives were :

1. To model the waterhole water balance and resolve waterhole stratification dynamics for both temperature and oxygen. Solar radiation attenuation was included, by implementing an unpublished empirical model made by DES linking turbidity to light attenuation. The role of riparian vegetation on water shading and wind-sheltering (where relevant) was considered in the model simulations, plus a

sediment oxygen demand model. The model was configured to run using available hydrologic and meteorological data and calibrated against the newly available high-frequency monitoring data collected by DES and DNRME. This includes thermistor and oxygen chains collected over a range of flow and weather conditions (Section 2).

2. To undertake physiological tests on temperature and hypoxia tolerances of relevant fish species, comparing native species and common carp, and to use this data to parameterise a fish habitat suitability model. The habitat suitability model accounts for the waterhole specific changes in temperature and oxygen that occur in response to hydro-climatological variability and is used to demonstrate the likely conditions that can lead to fish-kill events (Section 3).

3. To develop a conceptual understanding of how climate change may change the risks of fish-kill events, considering changes to stratification and fish habitat, and to demonstrate how the model developed above can be used to support climate change risk assessment and adaptation strategies. A scenario is modelled to show how a warming climate will lead to changes to stratification, increased hypoxia and more frequent conditions that may lead to fish-kills (Section 4).

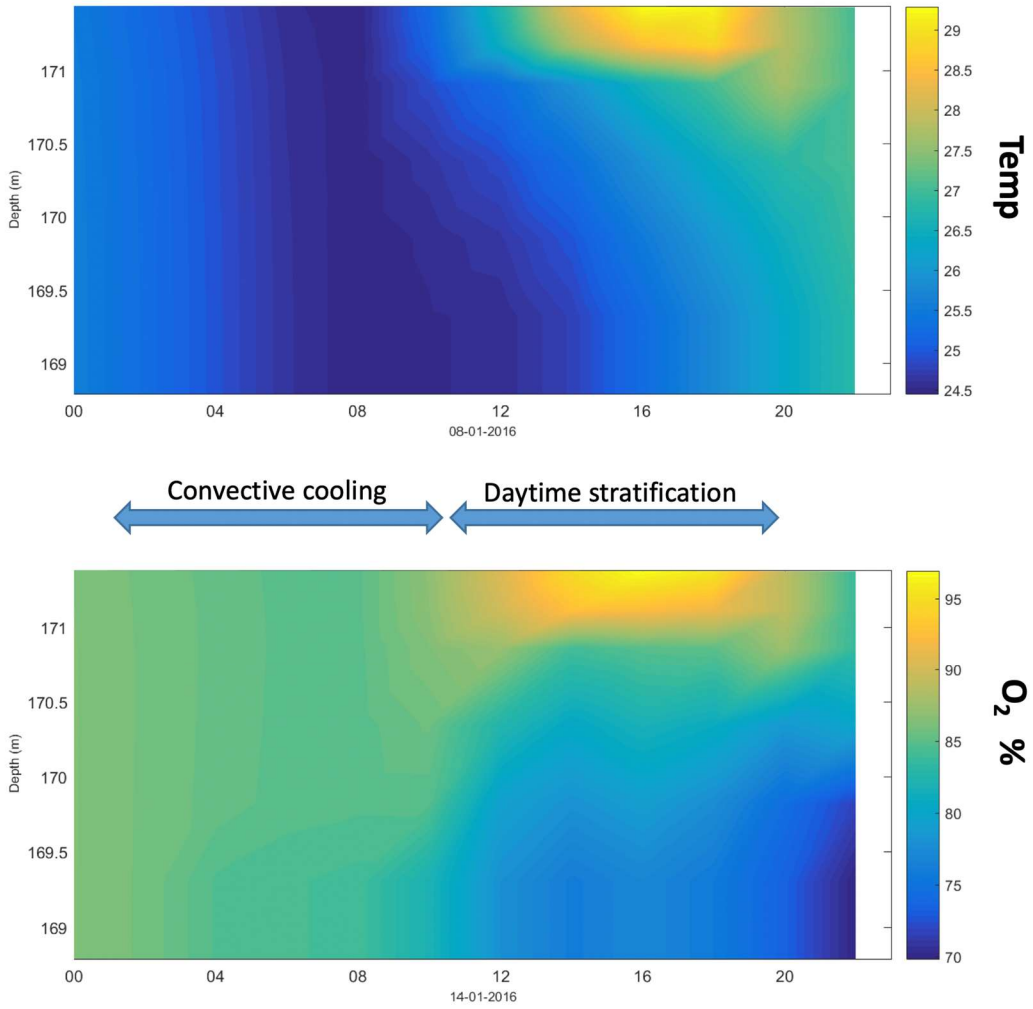

Figure 4: Example river waterhole temperature and oxygen daily profile evolution, based on an initial simulation of the Moonie River under low flow conditions (from Brookes and Hipsey, 2019). Note depths are the vertical position in m AHD.

2. Modelling stratification and hypoxia in inland river waterholes

2.1. Introduction

Ecohydrological modelling is the basis of water planning decisions in Queensland (Mcgregor *et al*., 2017) and elsewhere within Australia. Hydrology and temperature monitoring and modelling has been reported for ten waterholes in each of the Flinders and Gilbert River catchments (Waltham *et al*., 2013; Wallace *et al*., 2015; Wallace *et al*., 2017). These have provided key insights of the limnology and ecology of the waterholes, and formed a basis for assessing the potential impact of climate change on the waterholes. However, the vertical temperature stratification and hypoxia levels have not been assessed in these modelling studies, which are of critical importance to the fish habitats in our study sites as the fish are able to migrate vertically to avoid fish kills. Other than these reports, at present there has been very limited modelling of the quality aspects in dryland river waterholes in Australia that could be used as a template by managers and policy makers in Queensland for planning effective environmental flow policy or climate adaptation strategies to support their function as effective drought refugia for fish. Extension of most river models is questionable as flow ceases; in this case river waterholes become shallow lentic environments with extended periods of low mixing and the potential for persistent stratification.

Given the ecological value of weakly-connected or disconnected river waterholes, as outlined in Section 1, there is an urgent need that we can more confidently describe the important quality features of waterhole ecohydrology at a resolution relevant to management and which can be used to design and plan for both emergency interventions and longer-term restoration strategies (Anon, 2014). Important attributes include the subtle effects of controls on the water balance, such as ground-water seepage, wind-sheltering effects on evaporation, vertical temperature stratification, oxygen variability and turbidity. In particular, the role that wind and light attenuation play in shaping diurnal and longer-term patterns of thermal stratification and hypoxia (as indicated in Figure 25) is critical to establish the functional requirements for waterholes to act as effective drought refugia.

Shallow waterbodies are not typically thought to be associated with stratification as only a small amount of wind or evaporative cooling can drive water column turnover. However, river waterholes in particular are subject to substantial wind-sheltering and shading effects from the riparian vegetation on both sides of the rivers (Figure 5) which creates a relatively steady environment for stratification. The localization of weather conditions obtained from the nearby weather stations is therefore important to account for wind-sheltering and shading effects on the water stability.

2.2. Study sites and field data collection

In this study we focus model development around six waterholes in the northern MDB where data were available. The six sites, Kooroon, Kurmala, Brenda Weirpool, Weribone, Reilly's Weir and Trafalgar, are located approximately between 300 km to 500 km inland from Brisbane, Queensland (Figure 6, Table 1). A range of bathymetric, meteorological, hydrological, and limnological data were compiled and summarised below.

The bathymetry of each waterhole was surveyed using a gridded network of depth, position and time every two seconds recorded by a boat mounted sonar and GPS system. Each survey consisted of a longitudinal section, a near-perimeter trace and 40 cross sections. Perimeters were hand drawn to encompass the survey points, and fit available base maps. Waterhole volume and surface area were calculated and tabulated at 0.01 m depth intervals from full DEM extent to empty (ArcGIS, 10.4.1, 3d analyst tools, ESRI).

Figure 5: Photograph of one of the study sites: Reilly's Weir, showing dense vegetation surrounding the waterhole.

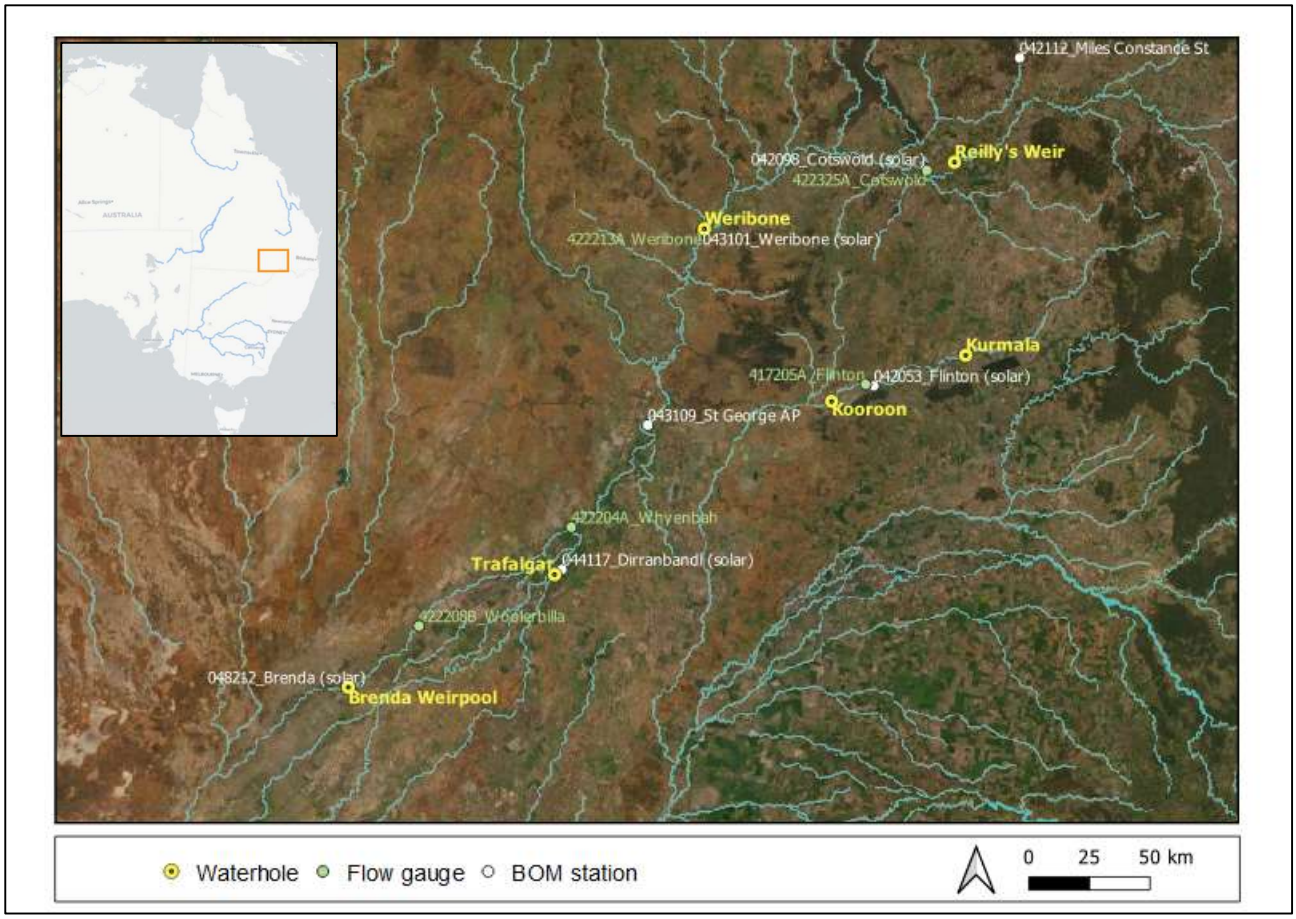

Figure 6: Map of six waterholes, their nearby flow gauges and BOM weather stations.

Table 1: Study sites' GPS coordinates and their closest flow gauges.

Site name	Lat	Long	Flow gauge
Kooroon (DES 4172018)	-27.95914	149.38060	417205A Moonie River at Flinton
Kurmala (DES 4172022)	-27.78507	149.95186	417205A Moonie River at Flinton
Brenda Weirpool (DES)	-29.03805	147.31230	422208B Culgoa River at Woolerbilla Rd
Weirbone (DNRME)	-27.30717	148.83769	422213A Balonne River at Weribone
Reilly's Weir (DNRME)	-27.05396	149.90398	422325A Condamine River at Cotswold
Trafalgar (DNRME)	-28.60903	148.19824	422204A Culgoa River at Whyenbah

Bathymetric data as described above was linearly interpolated onto the mesh created in Surface-water Modelling System Version 12.3 (*Figure 7-9*), and used to generate hypsographic curves for GLM.

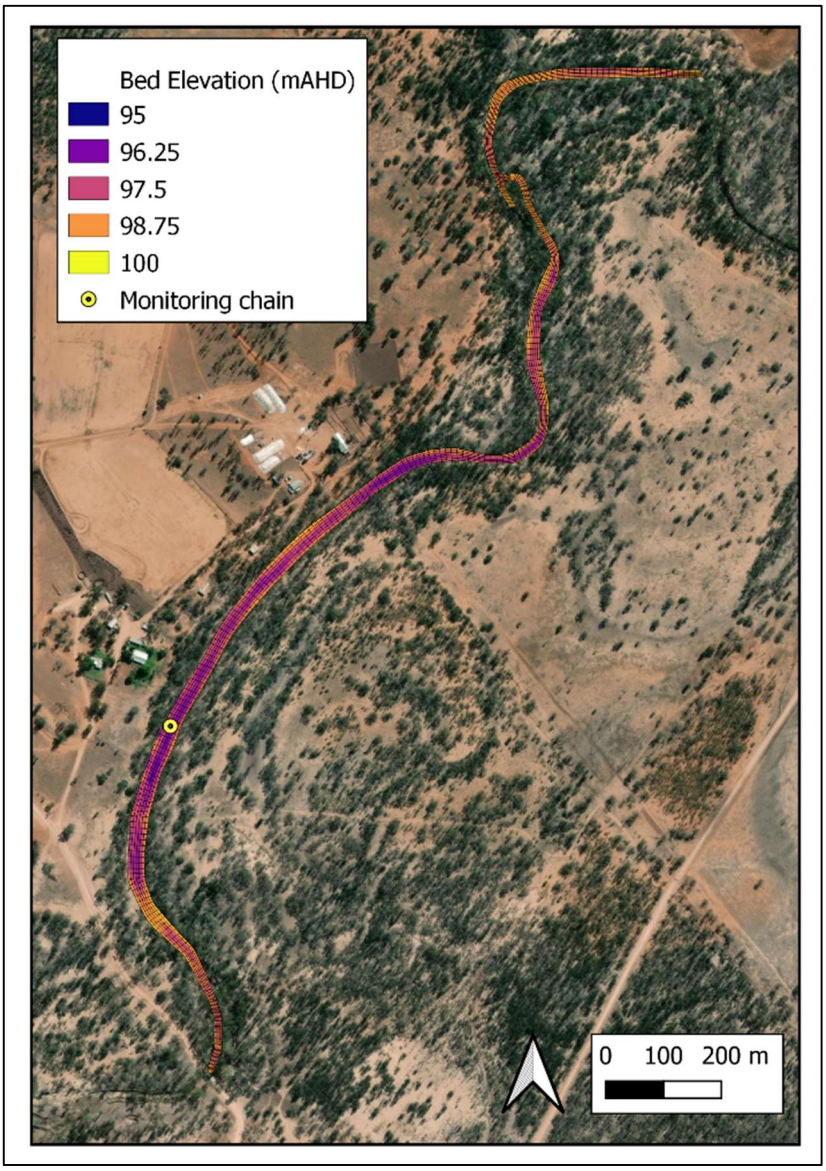

Figure 7: Model mesh for Kooroon.

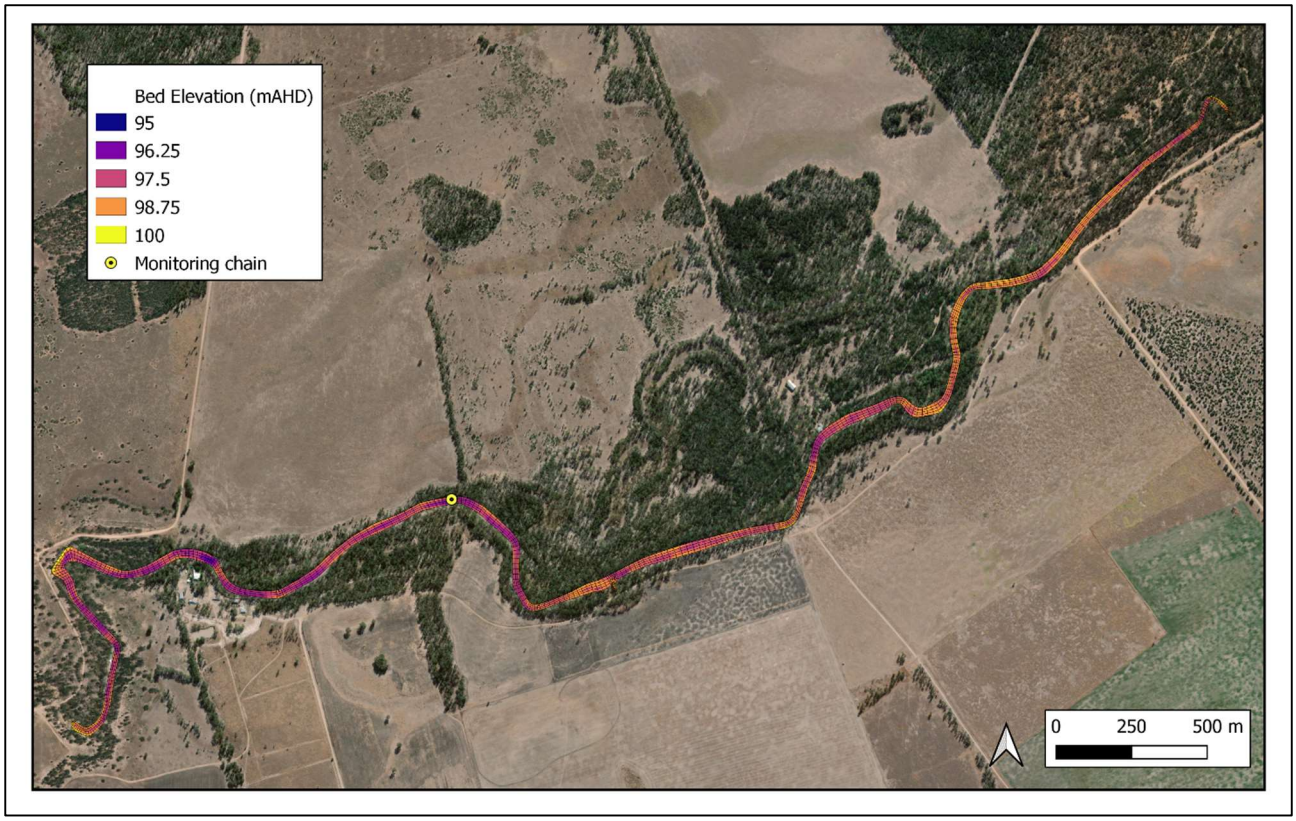

Figure 8: Model mesh for Kurmala.

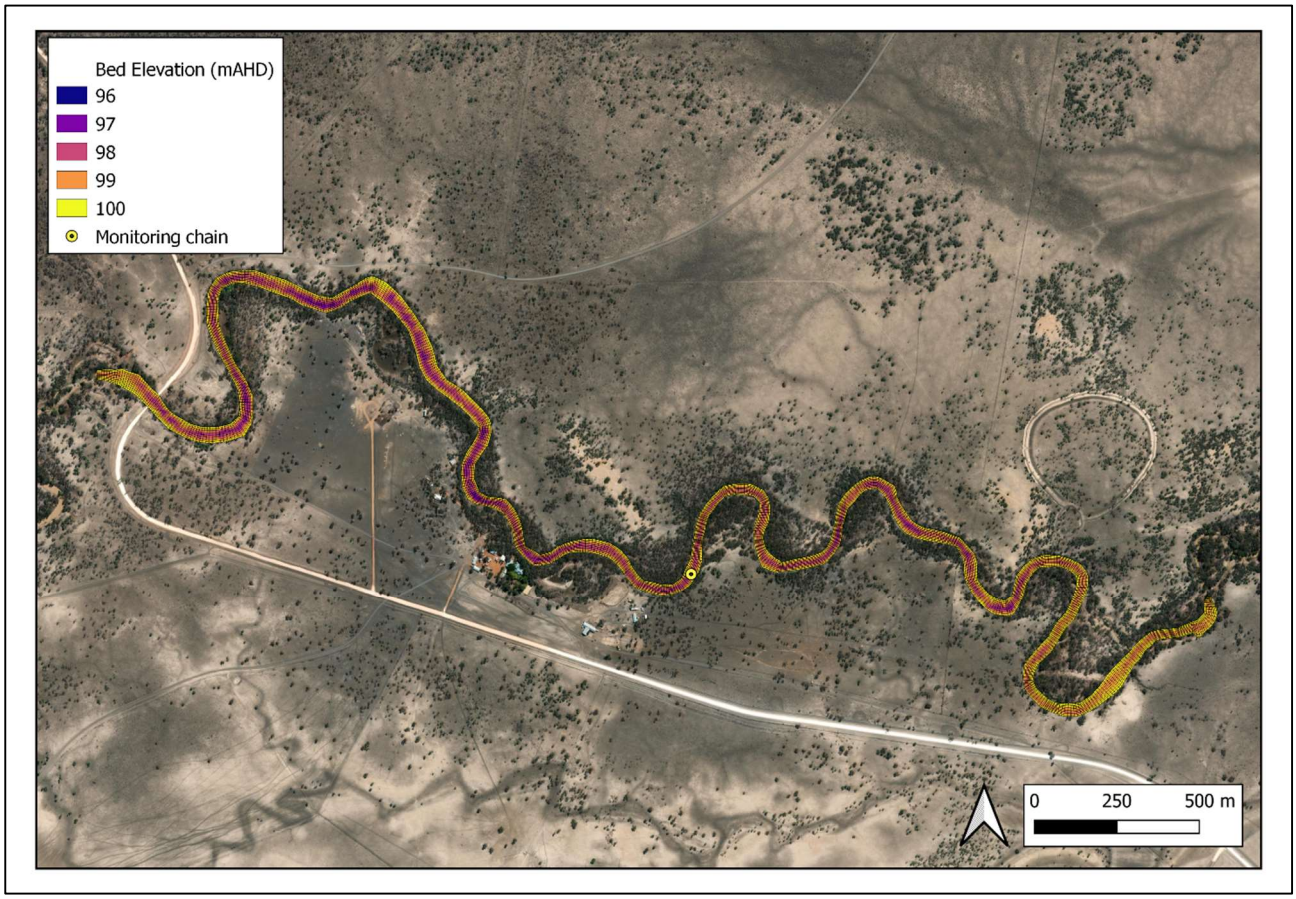

Figure 9: Model mesh for Brenda Weirpool.

Flow data reaching each pool was approximated from data that was obtained from Queensland Water Monitoring Information Portal (https://water-monitoring.information.qld.gov.au/) for the nearest flow monitoring station (Table 1). Flow gauges were selected based on distance from study sites regardless of upstream or downstream due to limited options.

Weather data were acquired from Bureau of Meteorology (BoM) for the nearest weather station with the most complete data. The weather datasets included air temperature, humidity, wind speed and direction, and shortwave that were imported and used for hydrodynamic model forcing. An example dataset at the St George Airport station (ID 043109) is shown in Figure 10 which indicates a relatively strong diurnal variation in the weather records.

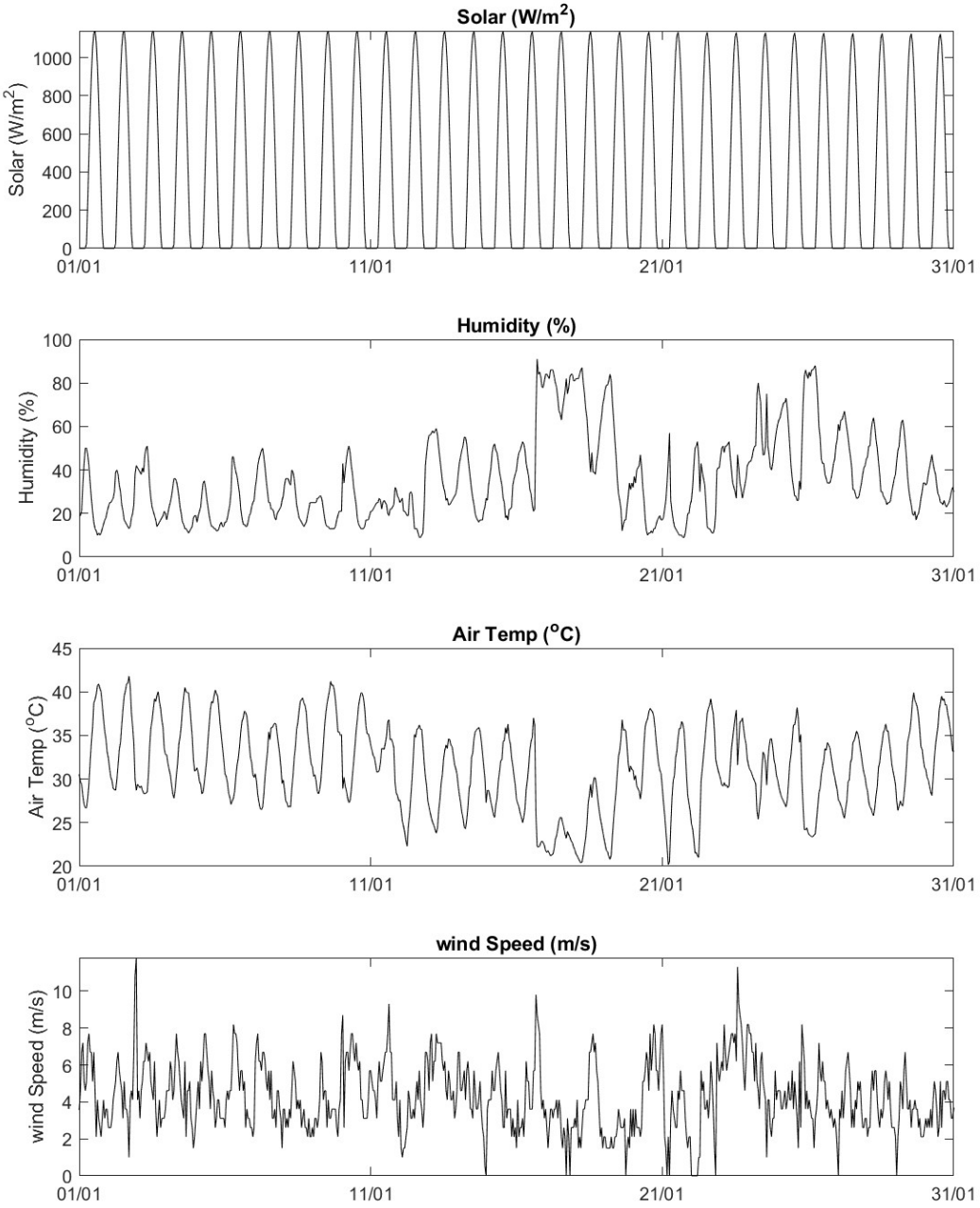

Figure 10: Example of weather record at the St George Airport BoM station in a selected period of January 2020.

Monitoring chain data was collected by Department of Environment and Science (DES) and Department of Natural Resources, Mines and Energy (DNRME). Water temperature and dissolved oxygen were recorded every 10 minutes at various depths in the water column at each pool from mid-2019 to late 2020 (Table 2). Water depth (barometric compensated pressure) was recorded at 10-minute (Kooroon, Kurmala and Brenda) or 30-minute (Weribone, Reilly's Weir and Trafalgar) intervals in each pool. Loggers were lost during the flood in March 2020 at Brenda Weirpool.

Table 2: Dissolved oxygen and water temperature data availability at six pools.

Site	Date	DO/temp logger node depth (m)	Frequency
Kooroon (DES)	10/2019 - 11/2020	0.3, 0.8, 1.25, 1.75, 2.25, 3.2, 4.2, 5.2 (from surface)	10 min
Kurmala (DES)	10/2019 - 9/2020	0.3, 0.8, 1.25, 1.75, 2.25, 3.2, 4.2, 5.2 (from surface)	10 min
Brenda Weirpool (DES)	8/2019 - 3/2020	0.3, 0.8, 1.25, 1.75, 2.25, 3.2, 4.2, 5.2 (from surface)	10 min
Weirbone (DNRME)	9/2019 - 9/2020	2.4, 2.2, 2.0, 1.8, 1.6, 1.4, 1.0, 0.8, 0.6, 0.4, 0.2 (from substrate)	10 min
Reilly's Weir (DNRME)	5/2019 - 7/2020	1.8, 1.3, 0.8, 0.6, 0.4, 0.2 (from substrate)	10 min
Trafalgar (DNRME)	5/2019 - 8/2020	1.2, 1.0, 0.8, 0.6, 0.4, 0.2 (from substrate)	10 min

For Kooroon, Kurmala and Brenda, logger chains were fixed to a floating station (Figure 11), therefore node depths are indicated as distance from water surface. This means the lower nodes would be lying on/buried in the substrate when water level falls. These waterholes were chosen, based on past bathymetry information, to be the deepest/most persistent in their river sections. Within the waterholes, the deepest locations were chosen for sensor deployment within constraints of proximity to river access points and suitable sites for base stations. Sensors were shaded from direct sunlight by the buoys from which they were suspended and by the light attenuation influence of high turbidity. Loggers were maintained and cleaned as often as logistics permitted and the data were scrutinised for signs of fouling interference and suspicious data was removed prior to analysis and modelling.

For Weribone, Reilly's Weir and Trafalgar, chains are fixed to the substrate and the node depths are indicated as distance from substrate. Therefore, the top nodes would be logging in air when water level drops sufficiently.

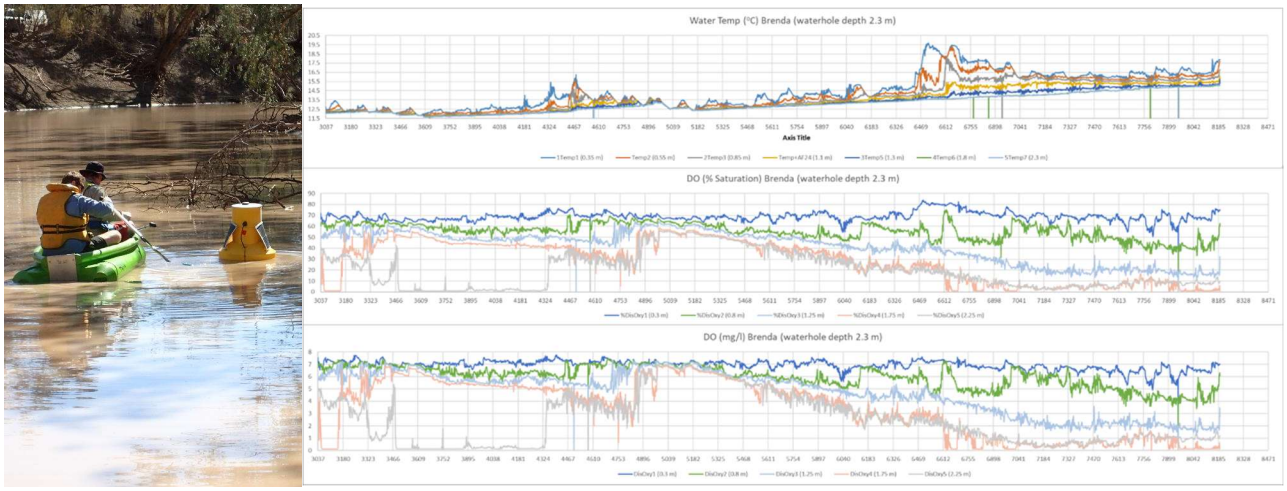

Figure 11: Example of the temperature and oxygen mooring (left) and associated monitoring chain data demonstrating periods of mixing and periods of stratification (right).

All data points where logger nodes were above water surface or in sediment were removed. Periods with node(s) above surface are indicated by its percent saturation DO hovering around 100% at all times, and its temperature oscillating dramatically (Figure 12). Data points with zero or negative values, or within periods when logging became intermittent towards the end were also removed. Percent saturation DO were computed using the R package 'LakeMetabolizer' for Weirbone, Reilly's Weir and Trafalgar.

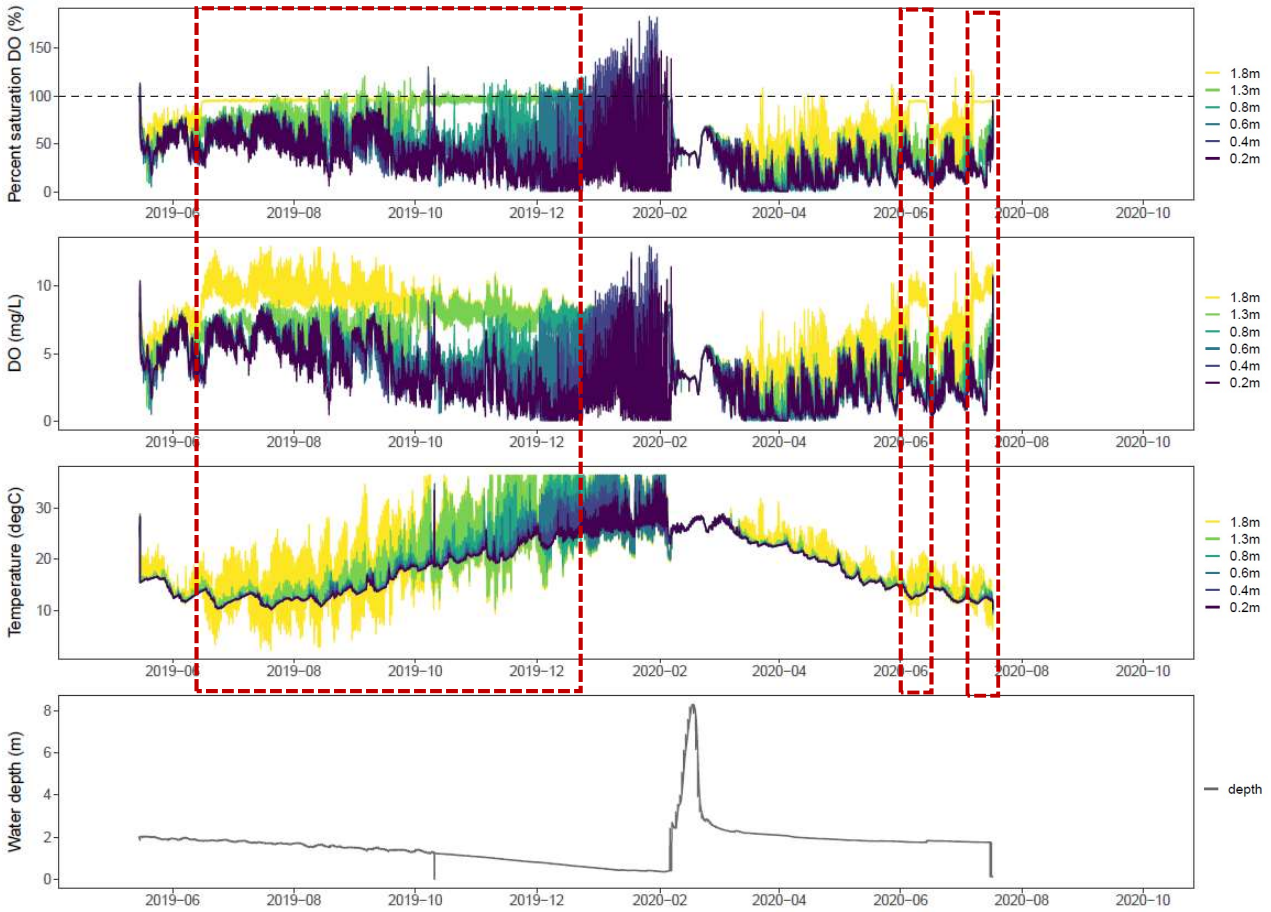

Figure 12: Temperature and DO plot from the raw data at Reilly's Weir – an example showing periods when top logger nodes (1.8m and 1.3m) were above water surface (within red rectangles).

2.3. Pool hydrology, stratification and oxygen analysis

2.3.1. Stratification dynamics

Thermal stratification was pronounced in all pools prior to receiving major inflows in Jan-Feb 2020, except Trafalgar where it was completely dried out in Aug 2019 shortly after a flow event in May 2019 (Figure 13 to Figure 17).

At Kooroon and Reilly's Weir, water column remained well-mixed for about a month since the start of major flows, after which stratification recommenced. For Kooroon, stratification was relatively mild through to late

Aug 2020, and became pronounced again from Sep 2020. For Reilly's Weir, however, stratification quickly returned to the pre-flooding strength as its water level decreases rapidly.

At Weribone, waters remained well-mixed for over three months, possibly due to the major flood event. Similar to Kooroon, stratification then developed slowly and strengthened from Sep 2020.

In contrast, stratification lasted for over a month at Kurmala since the start of inflow in late Jan 2020, although less pronounced than the preceding period. Water column remained relatively well-mixed from late Apr through to Sep 2020.

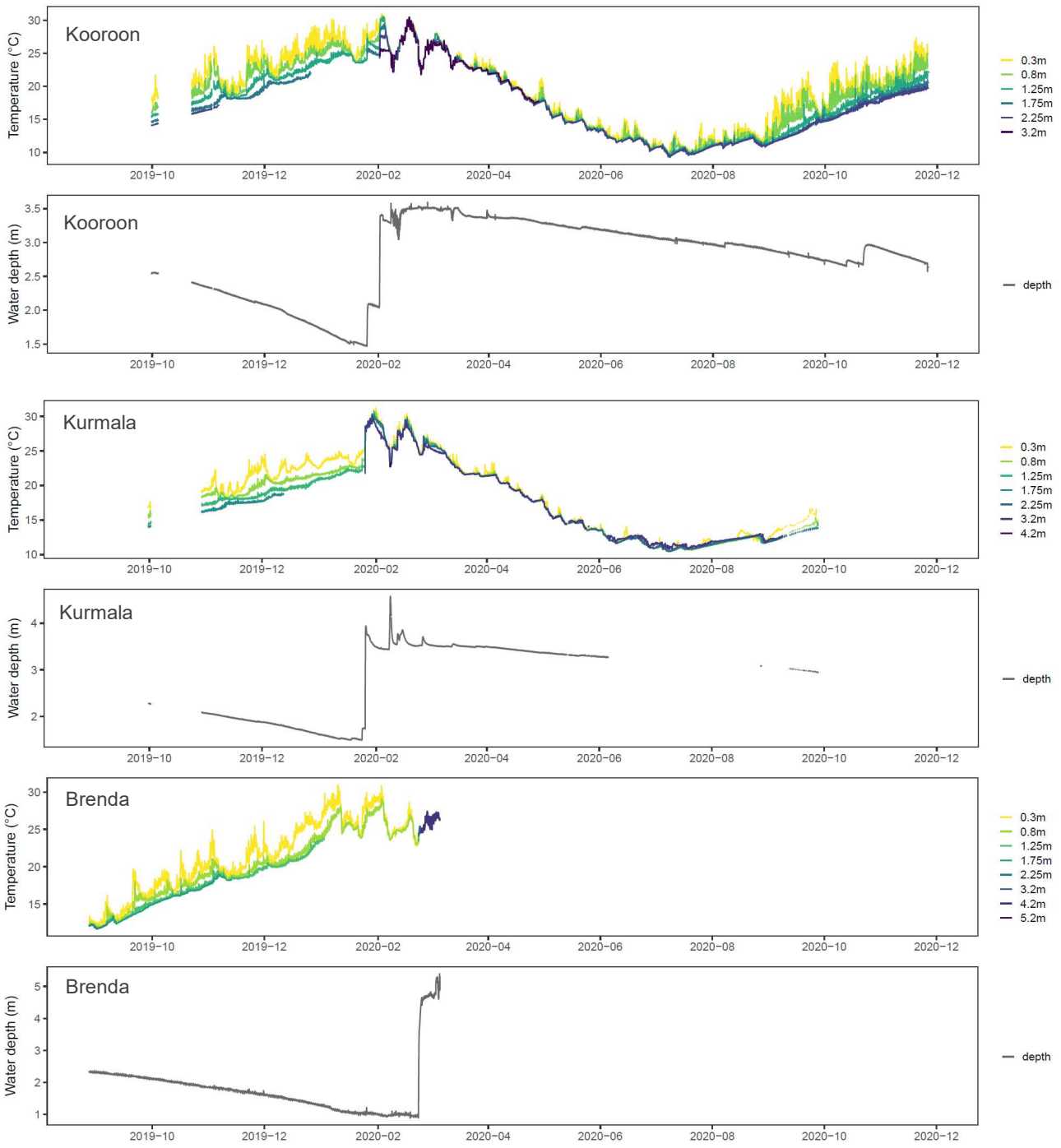

Figure 13: Water temperature and depth time-series of Kooroon, Kurmala and Brenda pools. Logger chain node depths in the legend are distance from water surface.

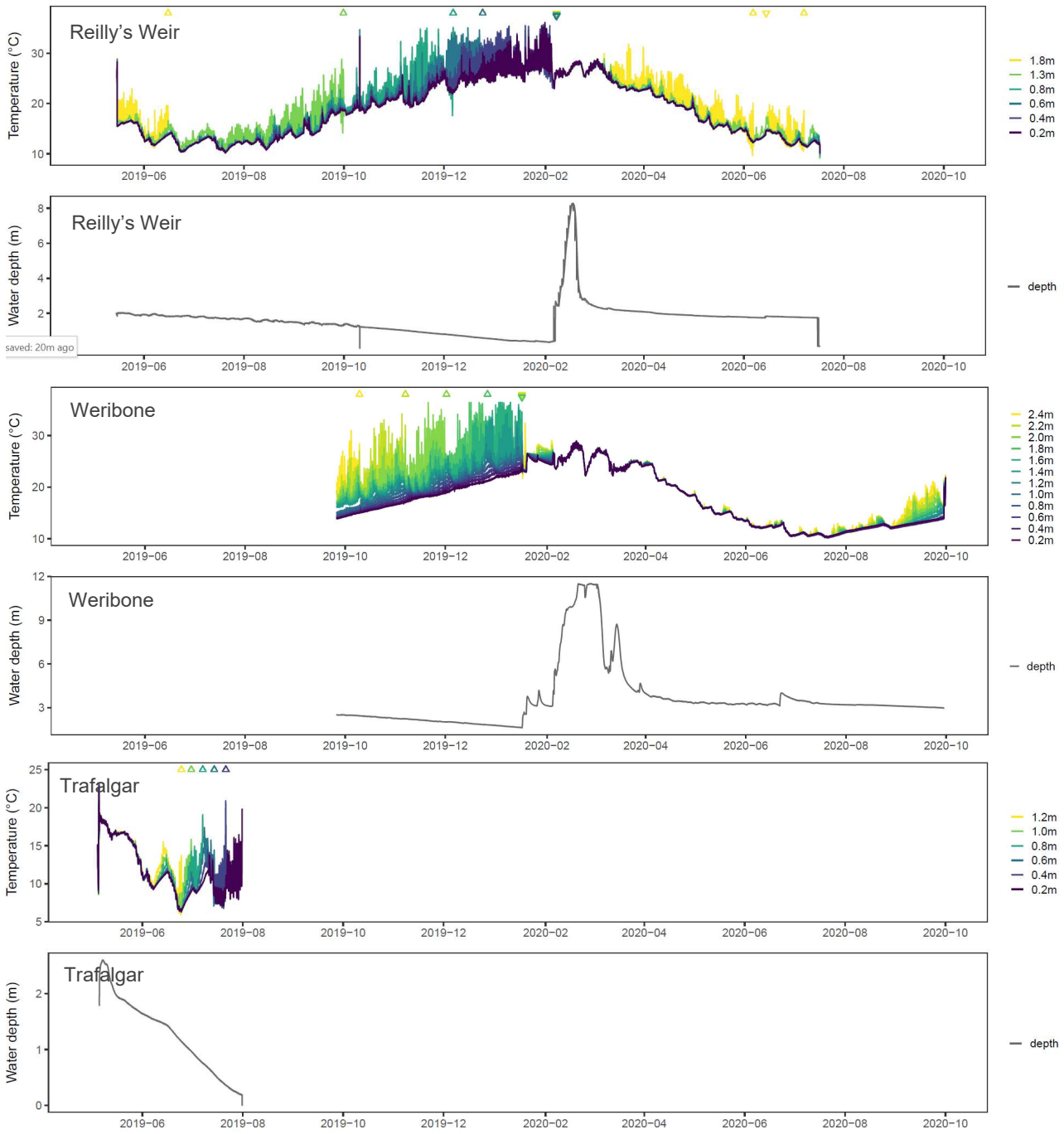

Figure 14: Water temperature and depth time-series of Reilly's Weir, Weribone and Trafalgar pools. Logger chain node depths in the legend are distance from substrate. Periods when particular logger node(s) were above water level (data point removed) are indicated between a triangle (△) and an upside-down triangle (▽) on top of each graph.

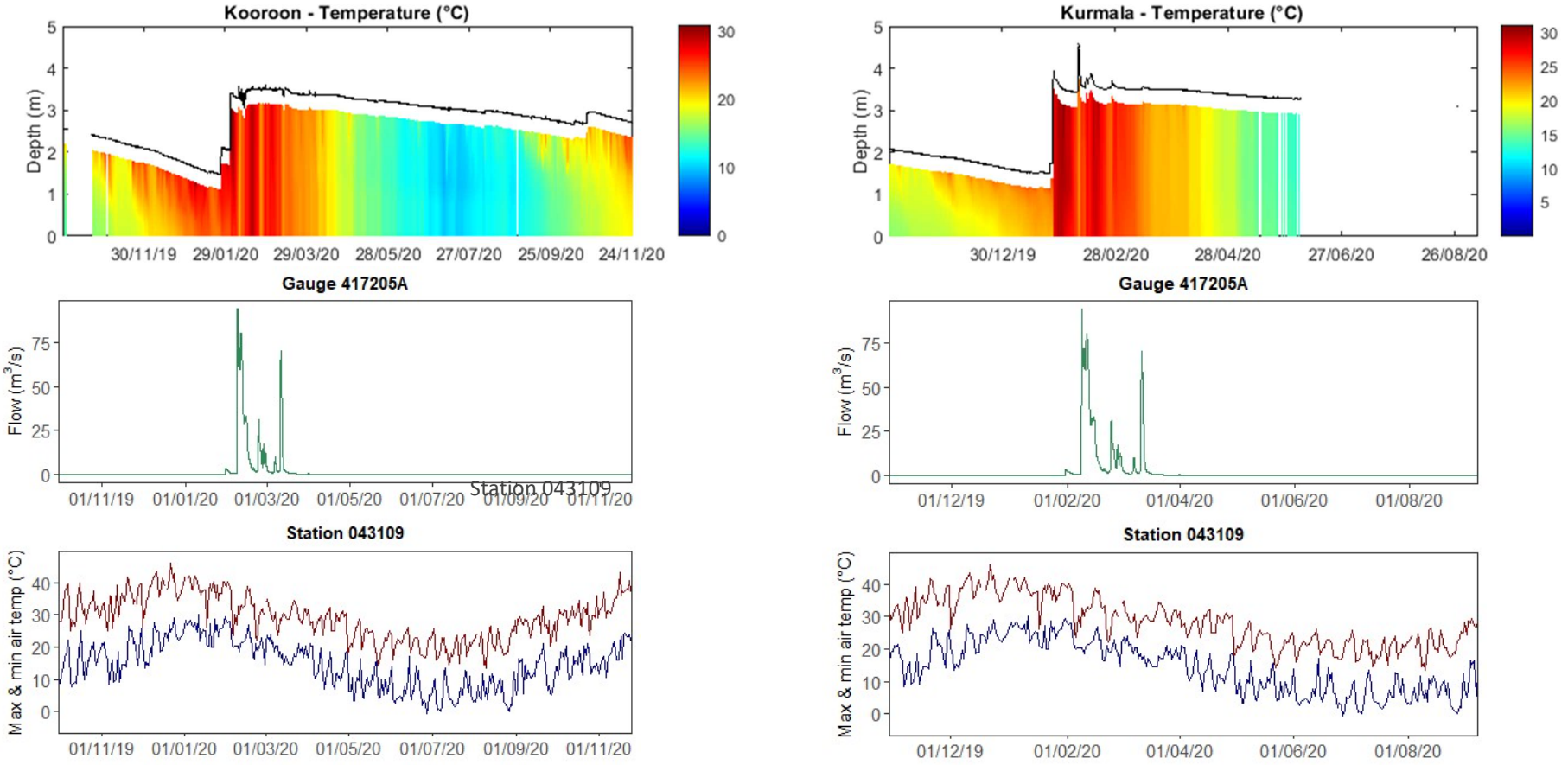

Figure 15: Filled contour plots of water temperature at Kooroon (left) and Kurmala (right), and flow rate and air temperatures from nearby gauges/stations. Black line in contour plot indicates water level. The gap in contour plot between late June to late August at Kurmala was due to water level logger failure.

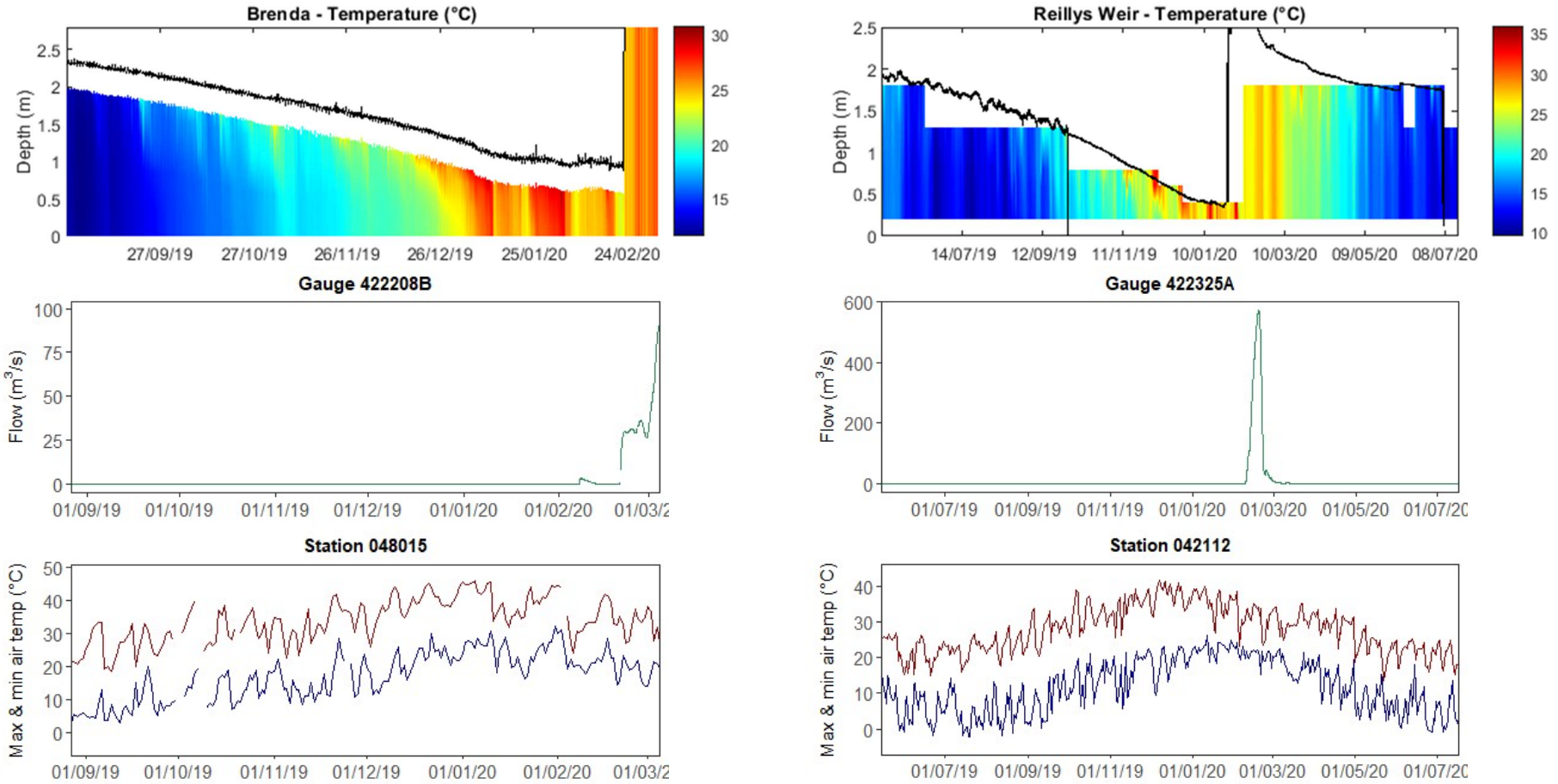

Figure 16: Filled contour plots of water temperature at Brenda (left) and Reilly's Weir (right), and flow rate and air temperatures from nearby gauges/stations. Black line in contour plot indicates water level.

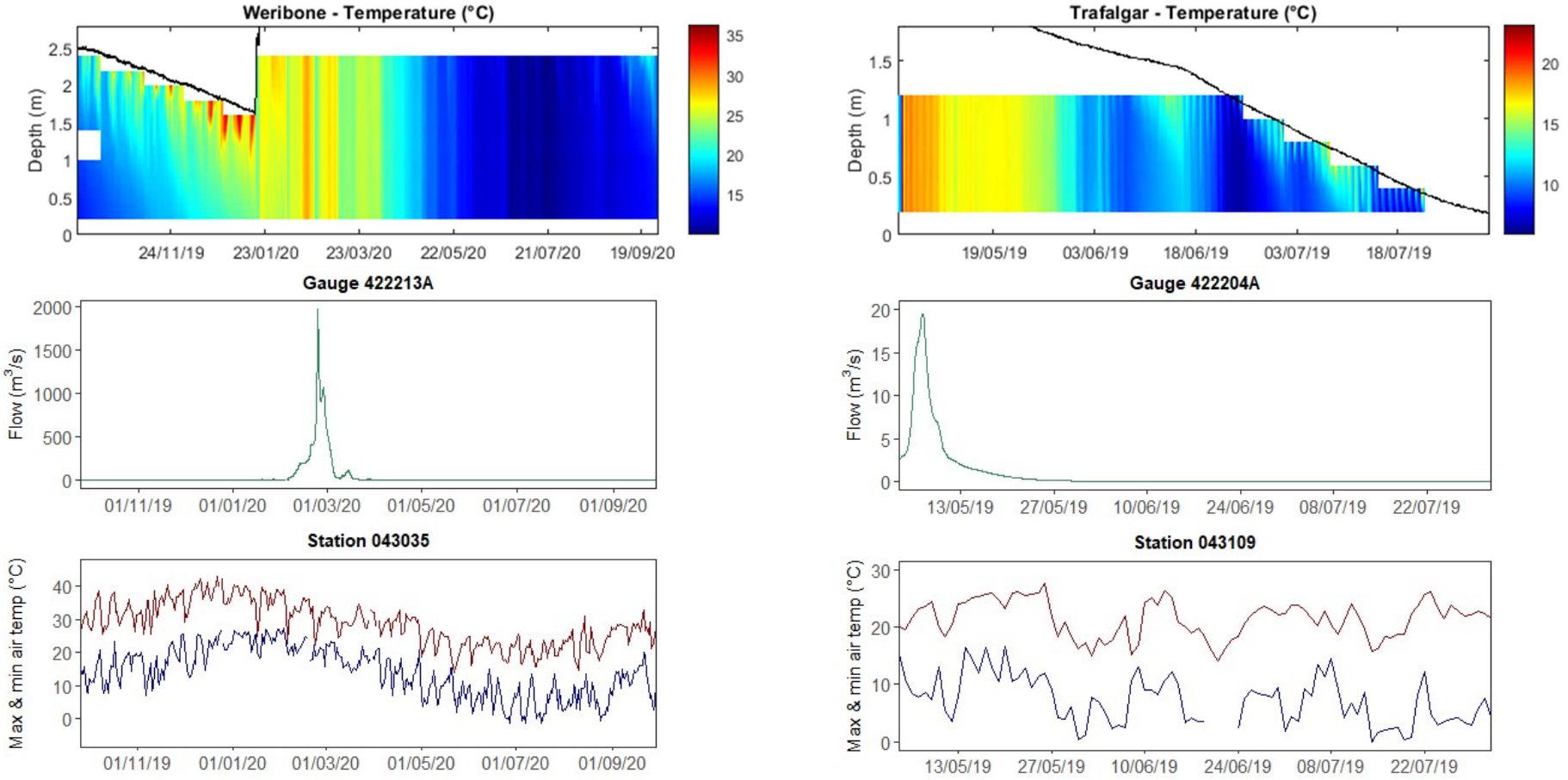

Figure 17: Filled contour plots of water temperature at Weribone (left) and Trafalgar (right), and flow rate and air temperatures from nearby gauges/stations. Black line in contour plot indicates water level.

2.3.2. Flow-mixing criteria

In addition to wind mixing and evaporation cooling, flow rate is another driver for mixing of rivers. Full mixing occurs when the flow exceeds a certain rate that produces turbulent kinetic energy and overcomes the water stability for a specific study site (Eq 1), which can be defined as the flow-mixing criteria for that river reach.

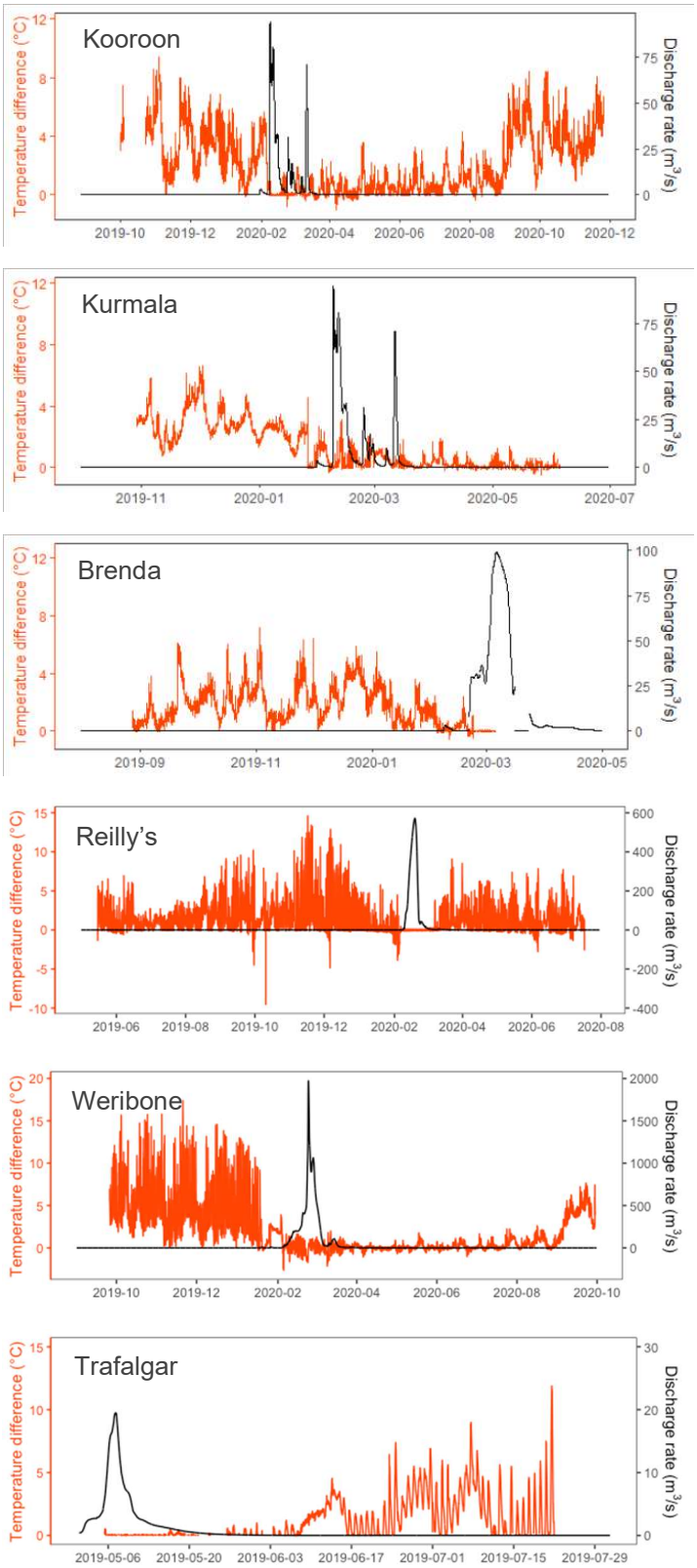

Figure 18*: Temperature difference between top and bottom layer in six pools against flow rate from the nearest gauge.*

When comparing temperature difference between the top and bottom layer at each pool (i.e. the intensity of stratification) with flow from its nearby gauge, Kooroon, Reilly's Weir, Trafalgar and possibly Brenda showed a relatively clear inverse relationship – there was no or very mild stratification (< 1°C difference) during high flows (Figure *18*). Such a relationship was less evident at Kurmala, however this could be due to its closest flow gauge situated over 50 km downstream. At Weribone, the major flood had a long-lasting dampening effect on stratification.

However, there is a concern that the local water balance is not only affected by the upstream gauged flow but also modified by groundwater inputs and water abstraction. For example, a closer look at the gauged flow rate at the upstream of Kooroon and the observed water depth reveals an un-balanced flow relative to water elevation (Figure 19). The water depth increased during the day of 26/Jan/2020 while no gauged flow was observed, and there was a large inflow coming in on 08/Feb/2020 though the water depth only increased by ~0.2 m. This suggests that there may be ungauged flow (such as local rainfall events) or water diversion occurred in the Kooroon catchment, though unfortunately there was no gauge data at the region of study sites to further examine the water balance. This is not an issue when the modelling study focuses on the dry periods when no inflow is used, but requires further investigation when the modelling of flow mixing is required.

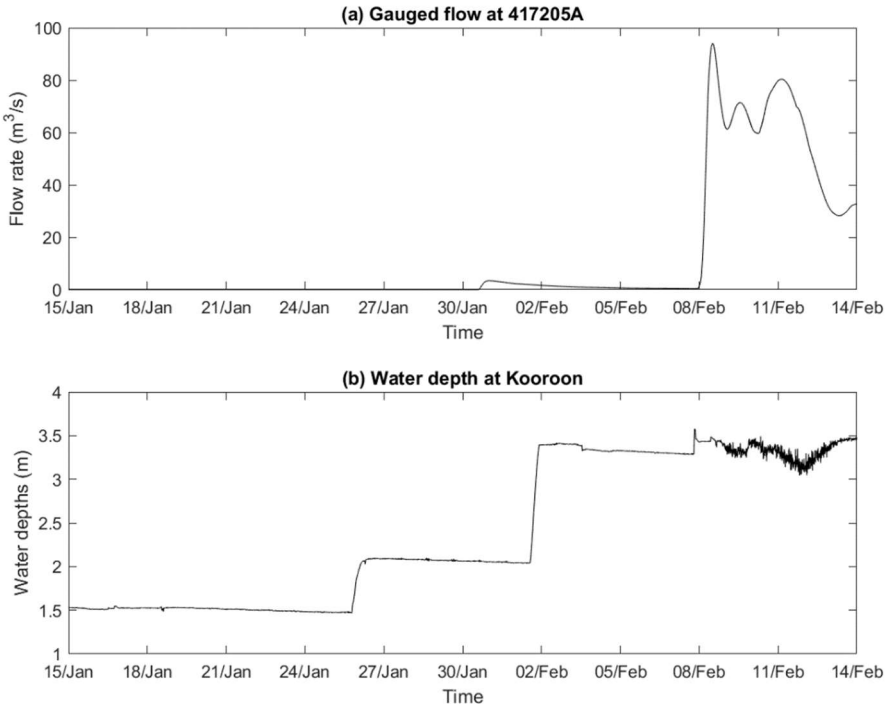

Figure 19: Records of (a) gauged flow at upstream of Kooroon (site 417205A); and (b) observed water depth at Kooroon.

2.3.3. Oxygen dynamics

Overall dissolved oxygen was low and stratification was pronounced in Kooroon, Kurmala and Brenda before the first flow event in 2020 (Figure 20 to Figure 24). This was most prominent at Kurmala, where oxygen saturation within 50cm of the surface remained below 50%. Its oxygen saturation dropped to 0% at times ≥ 1 m below the surface. In comparison, Reilly's Weir was relatively well-mixed.

A few days after the first inflow event in 2020, all sites (excluding Trafalgar where it remained completely dry) experienced a crash in dissolved oxygen, possibly due to hypoxic blackwater events where large quantities of organic material washed in during flooding leading to increased bacterial activities and oxygen depletion. As flow continued, dissolved oxygen recovered and remained well-mixed for several weeks, until stratification recommenced.

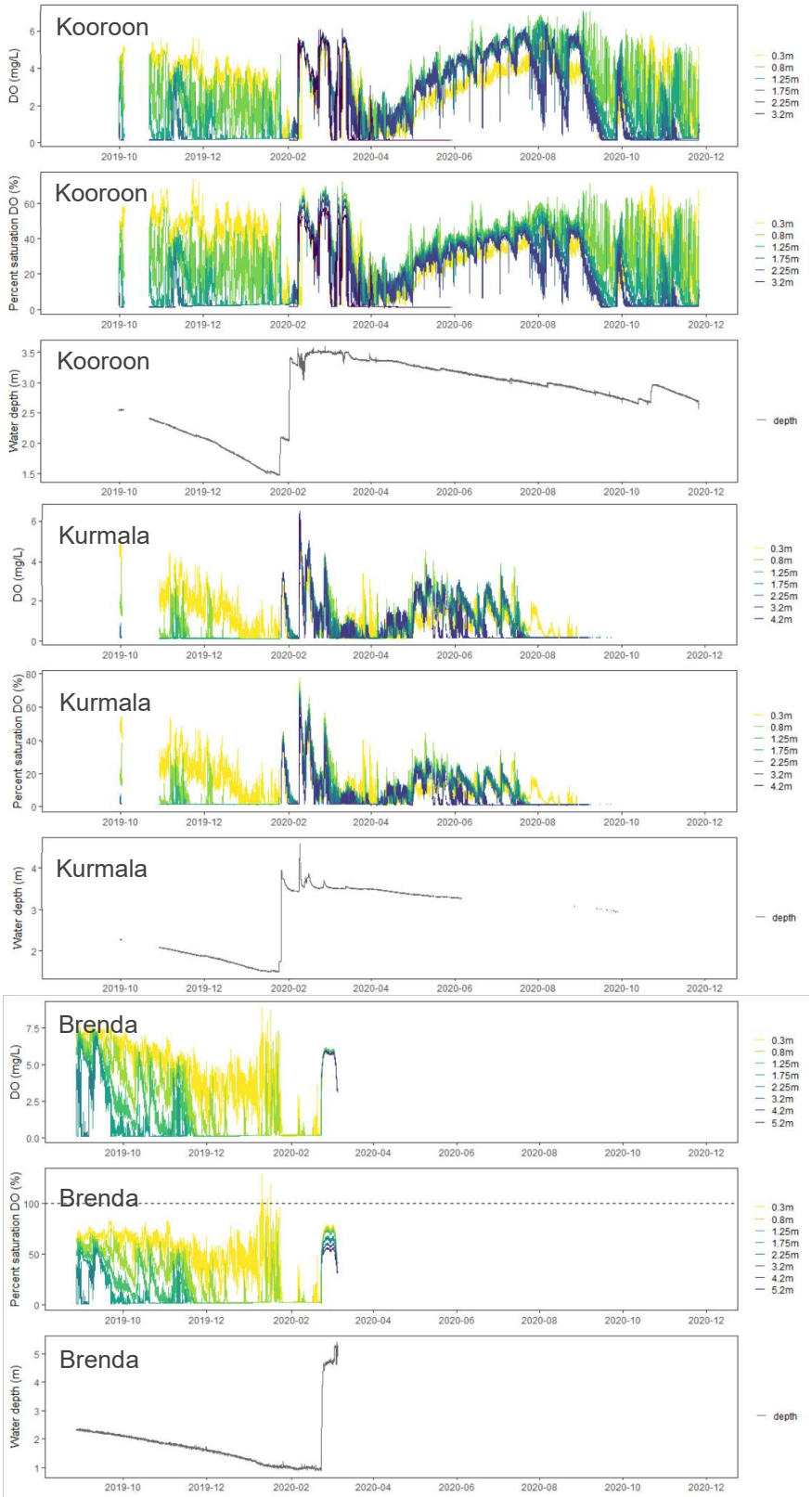

Figure 20: Dissolved oxygen (DO), DO saturation and water depth time-series of Kooroon, Kurmala and Brenda pools. Logger chain node depths in the legend are distance from water surface.

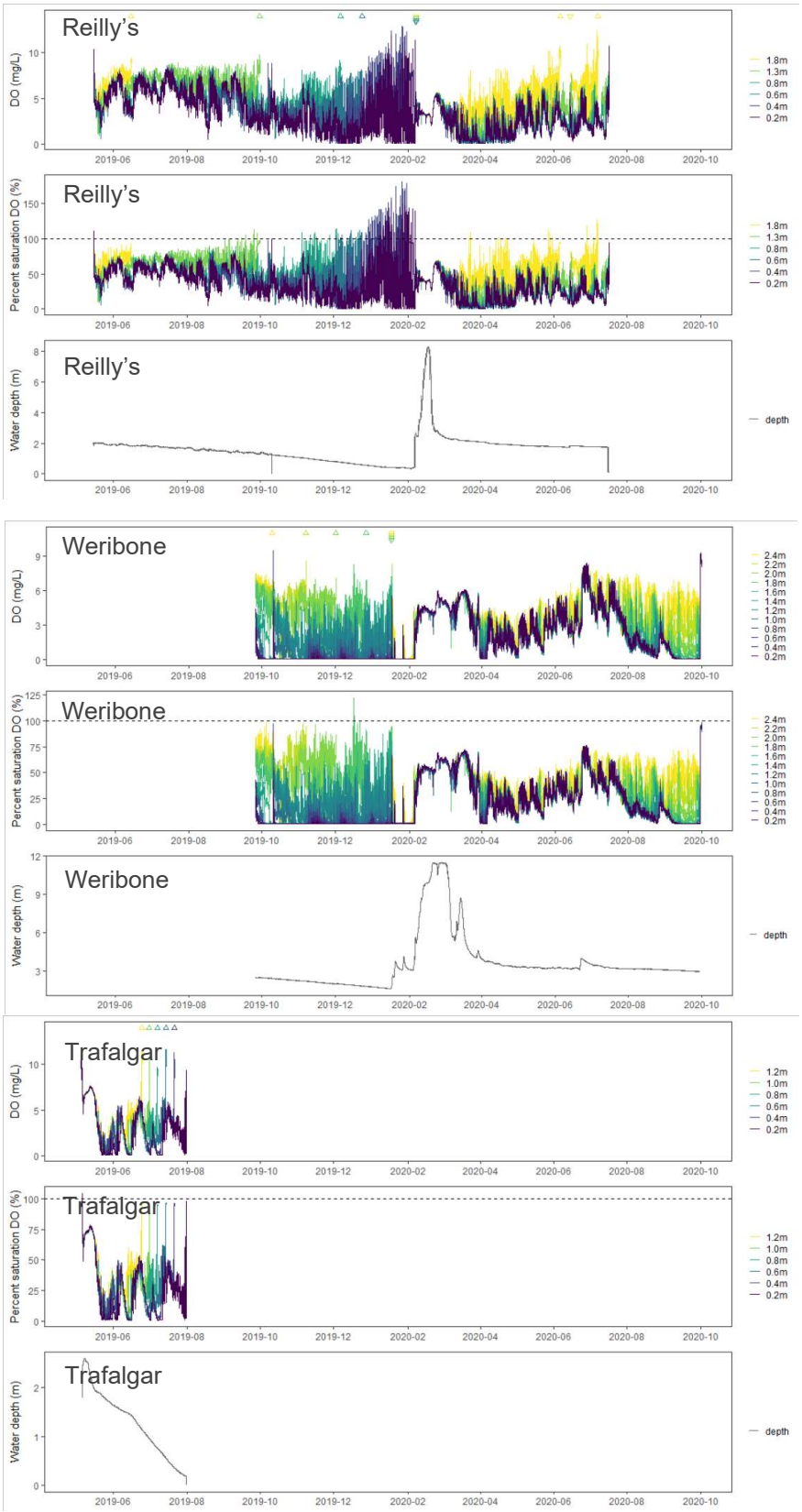

Figure 21: Dissolved oxygen (DO), DO saturation and water depth time-series of Reilly's Weir, Weribone and Trafalgar pools. Logger chain node depths in the legend are distance from substrate. Periods when particular logger node(s) were above water level (data point removed) are indicated between a triangle (△) and an upside-down triangle (▽) on top of each graph.

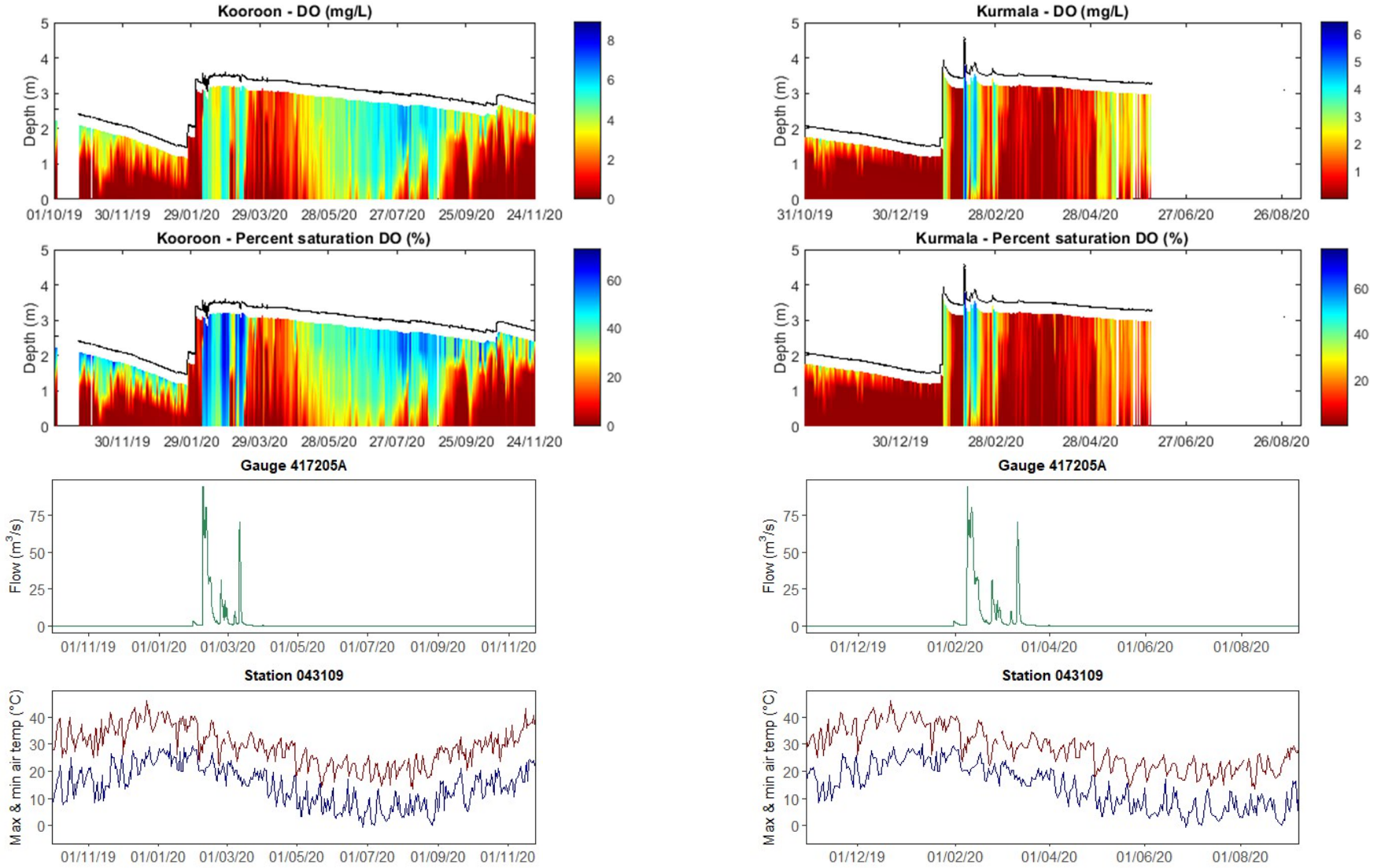

Figure 22: Dissolved oxygen (DO) and percentage saturation of dissolved oxygen at Kooroon (left) and Kurmala (right), and flow rate and air temperatures from nearby station. Black line in contour plot indicates water level. The gap in DO plots between late June to late August at Kurmala was due to water level logger failure.

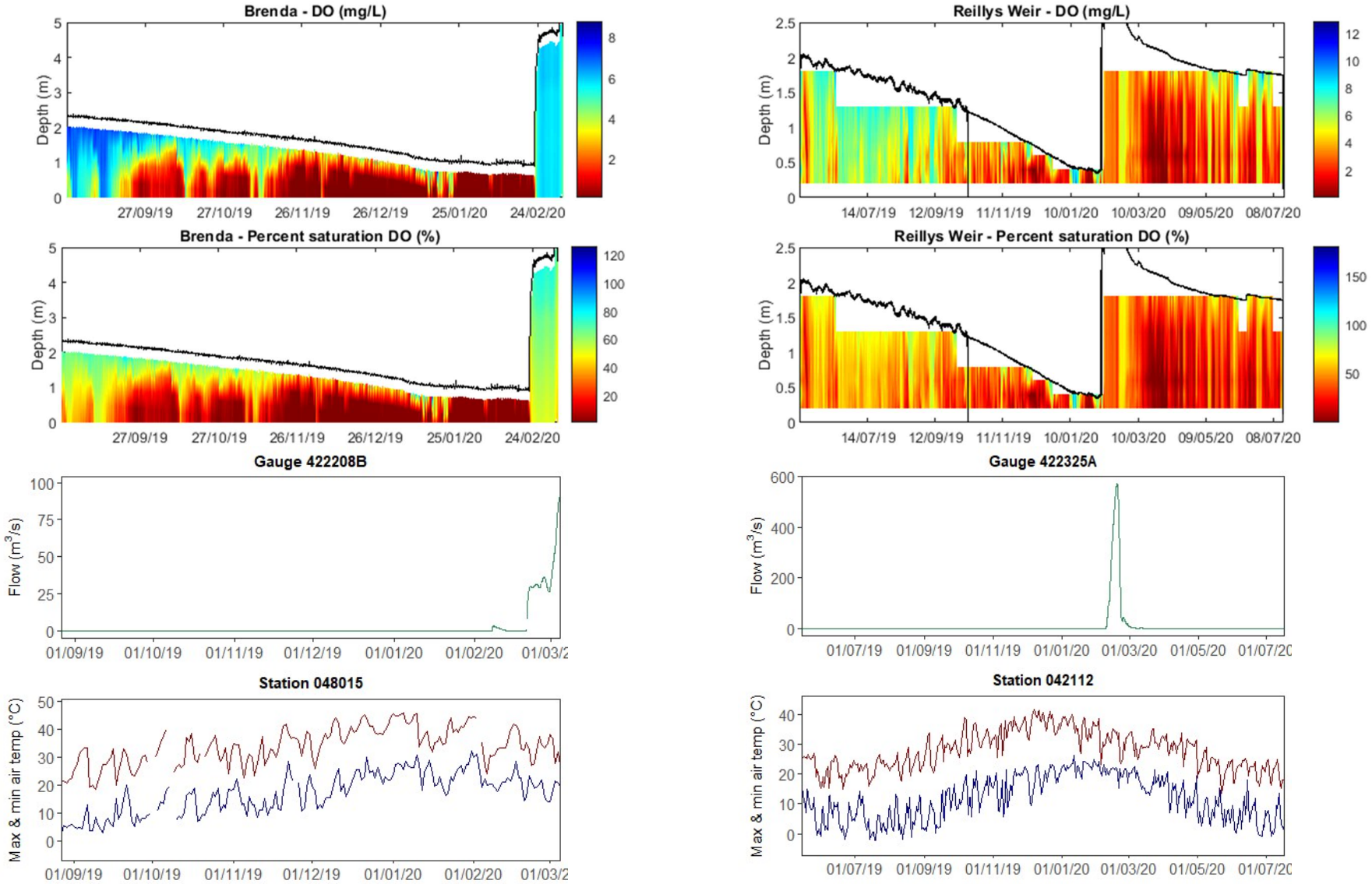

Figure 23: Dissolved oxygen (DO) and percentage saturation of dissolved oxygen at Brenda (left) and Reilly's Weir (right), and flow rate and air temperatures from nearby station. Black line in contour plot indicates water level.

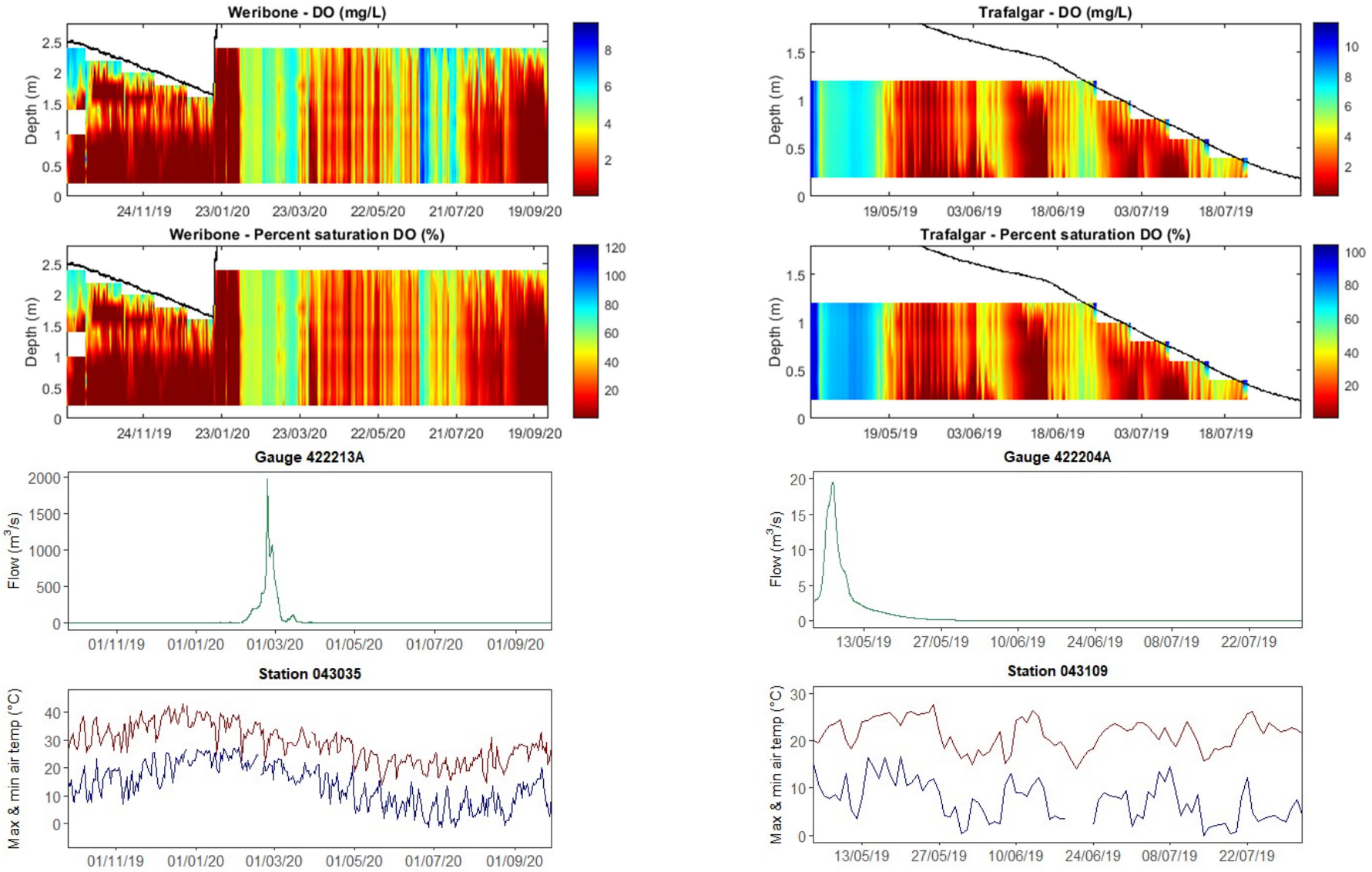

Figure 24: Dissolved oxygen (DO) and percentage saturation of dissolved oxygen at Weribone (left) and Trafalgar (right), and flow rate and air temperatures from nearby stations. Black line in contour plot indicates water level.

2.4. Conceptual basis for modelling waterhole stratification and hypoxia

From the data review a refined conceptual model for heat exchange at the air-water interface and vertical mixing processes of the waterholes is shown below (Figure 25). The specific processes are explored in further detail in the below sections.

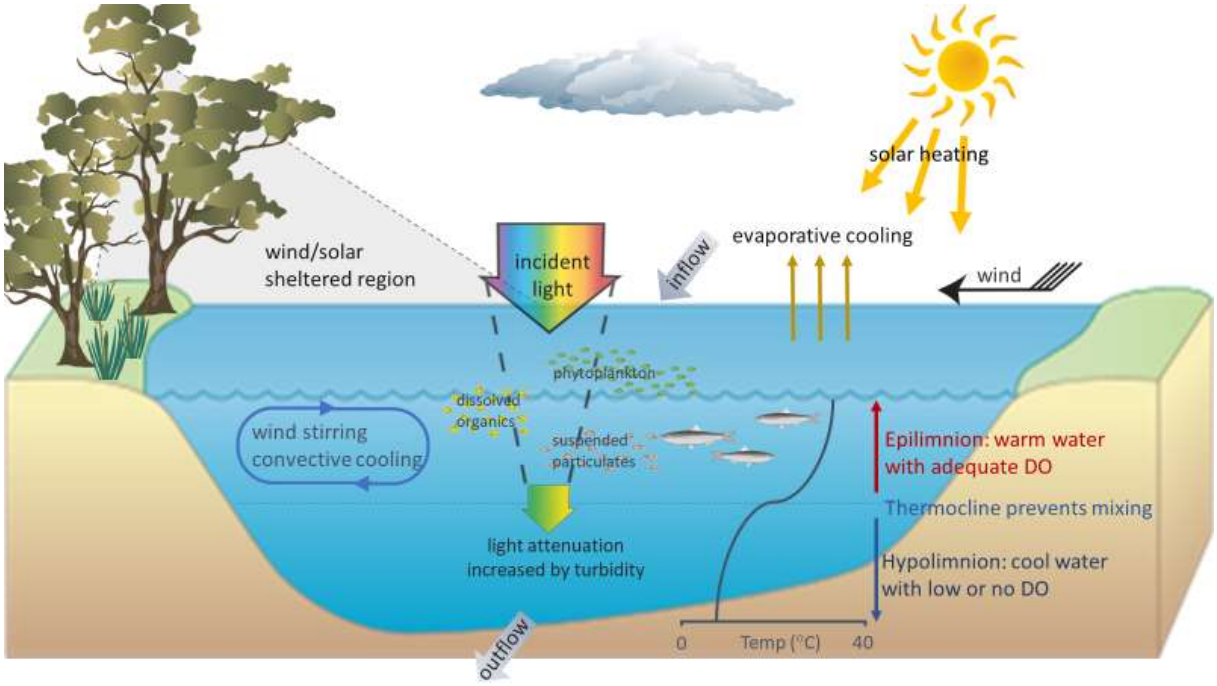

Figure 25: Conceptual model of processes influencing river pool thermal stratification.

2.4.1. Mixing threshold

As identified the Section 2.3.2, flow and surface meteorological conditions will determine the extent of stratification .The mixing criterion developed by Bormans and Webster (1997) can be used to estimate the critical flow required to disrupt thermal stratification in river pools, and is given by:

$$R = \frac{\text{destratifying TKE}}{\text{stratifying thermal energy}} = \frac{U^3}{H(Q_{net} - \frac{2Q_I}{K_W H})\frac{\propto g}{\rho C_p}} \quad (1)$$

where, U is the depth-averaged velocity, H is the water depth, Q_{net} is the net surface heat flux into the water column, Q_I is the net shortwave radiation, K_W is the light attenuation coefficient (m^{-1}), $\propto$ is the thermal expansion coefficient (2.10×10^{-4} ^0C), g is the gravitational acceleration (9.81 ms^{-2}), ρ is the density of water (1000 kg m^{-3}) and C_p is the specific heat capacity of water (4180 J kg^{-1} $^0C^{-1}$). The parameter R is only relevant when the factor in parenthesis is positive; otherwise the water column is losing heat, and stratification will not build up even under low discharge (Maier *et al.,* 2001). In order to use the above equation as a predictive tool, an estimate of Q_{net} in terms of easily available parameters

is needed. Q_{net} can be expressed as the sum of the radiative (short- and long-wave radiation), evaporative and sensible heat fluxes as follows:

$$Q_{net} = Q_I + Q_b + Q_e + Q_s \quad (2)$$

where, Q_I is the net short-wave radiation, Q_b is the net long-wave radiation, Q_e is the latent heat flux due to evaporation and Q_s is the sensible heat flux. The data on Q_I for each site was obtained from the Bureau of Meteorology (BoM). Q_b has been derived using an equation from Hodges (1998), and is given by:

$$Q_b = Q_{emitted} + Q_{absorbed} \quad (3)$$

$Q_{emitted}$ and $Q_{absorbed}$ were estimated as:

$$Q_{emitted} = -\varepsilon_{(water)}\,\sigma(273.2 + T_{(water)})^4 \quad (4)$$

and,

$$Q_{absorbed} = \varepsilon_{(air)}\,\sigma\left(1 + 0.17C_{(cloud)}^2\right)(273.2 + T_{(air\,2)})^4\,(1 - R_{t(lw)}) \quad (5)$$

where, $\varepsilon_{(water)}$ is the emissivity of the water, a non-dimensional constant (0.96), $\varepsilon_{(air)}$ is the emissivity of air derived using formula from Hodges (1998). C_{cloud} is the fractional cloud cover, $T_{(water)}$ is the water surface temperature, $T_{(air\,2)}$ is the air temperature (in Celsius degrees) measured two meters above the water surface, and $R_{t(lw)}$ is the total reflectivity of the water surface for long wave radiation.

The parameters Q_e and Q_s were estimated using the equation from Bormans and Webster (1997), and are given as:

$$Q_e = L_v \rho_a C_E W (q_s - q_a) \quad (6)$$

where, L_v is the latent heat of evaporation, ρ_a is the density of air, C_E is a dimensionless exchange coefficient for evaporative heat exchange, q_s and q_a are the specific humidities estimated from surface water temperatures, air temperature and humidity using the functional form of Kimball *et al.* (1982).

In a similar way, Q_s is estimated as:

$$Q_s = C_p \rho_a C_H W (T_s - T_a) \quad (7)$$

where, C_H is a dimensionless exchange coefficient for sensible heat exchange, W is the wind speed (m s^{-1}), T_s is the water surface temperature (^{0}C) and T_a is the air temperature (^{0}C).

In the case when flow ceases, the turbulent kinetic energy (TKE) that contributes to vertical surface water mixing can be produced by wind stirring or convective cooling which are calculated as:

$$E_{TKE} = 0.5C_k(C_w u_*^3)\Delta t + 0.5C_k(w_*^3)\Delta t \quad (8)$$

where C_k, C_w are mixing efficiency constants, Δt the calculation time step, w_* the velocity scale associated with surface cooling (Imberger and Patterson, 1981), and u_* is the velocity scale associated with wind stress and calculated according to the wind strength at 10 m above the water (U_{10}) and the drag coefficient for momentum (C_D) as:

$$u_*^2 = C_D U_{10}^2 \quad (9)$$

The theoretical critical flow rate (for river flowing condition) and wind speed (for non-flowing conditions) for vertical mixing at a specific waterhole can be therefore obtained from Eq (1) – Eq (9).

2.4.2. Solar heating and light attenuation

Solar radiation is the key driver of the lake thermodynamics and may be input based on daily or hourly measurements from a nearby pyranometer or estimated from the BIRD clear sky model (Bird and Hulstrom, 1981).

The depth of shortwave radiation penetration into the waterhole and through the layers is wavelength specific and depends on the water clarity via the light extinction coefficient K_W (m^{-1}). This can be modelled by two approaches. The first approach assumes that the photosynthetically active radiation (PAR) fraction of the incoming radiation is the most penetrative and follows the Beer-Lambert Law:

$$\emptyset_{PAR}(z) = f_{PAR}\, \emptyset_{SW0} \exp(-K_W z) \quad (10)$$

where z is the depth of any layer from the surface, and K_W is the light extinction coefficient (m^{-1}) and may be set by the user as constant or linked to the AED water quality model in which case the extinction coefficient will change as a function of depth and time according to the concentration of dissolved and particulate constituents. Beer's Law is only applied for the photosynthetically active fraction (PAR) component, f_{PAR}, which is set as 45% of the incident light. The amount of light heating the surface layer, $\emptyset_{SWs}$, is therefore the photosynthetically active fraction that is attenuated across the surface layer depth, z_s, plus the $(1 - f_{PAR})$ fraction, which accounts for near infra-red and ultraviolet bandwidths of the incident shortwave radiation with significantly higher attenuation coefficients (Kirk, 1994).

The second option integrates the attenuated light intensity across the bandwidth spectrum according to the model by Cengel and Ozisk (1984):

$$C_p \rho_i \Delta z_i \frac{dT_i}{dt} = \sum_{l=1}^{Nsw} \emptyset_{SWil}[z_i] - \sum_{l=1}^{Nsw} \emptyset_{SWi-}\ [z_i - 1] \quad (11)$$

where l is the bandwidth index and $\emptyset_{SWil}[z_i]$ is the radiation flux at the top of the i th layer for the l th bandwidth fraction. These processes are wavelength specific and the user specifies the number of simulated bandwidths, N_{sw}, their respective absorption coefficients, K_{wl}, and reflectivity of light at the sediment.

Downwelling PAR quantum irradiance immediately above the surface and through the water column were measured at two waterholes (Kooroon and Kurmala). Light extinction coefficients, K_W(PAR) are calculated according to Beer-Lambert Equation, rearranged as (Christian and Sheng, 2003):

$$K_W\,(\mathrm{PAR}) = -\frac{1}{z}\ln\frac{I_z}{I_0} \quad (12)$$

where z is the depth of interest (m), I_0 is PAR measured at the surface and I_z is PAR measured at depth z. For this calculation, z was taken as the greatest depth at which PAR was measured (when light intensity was less than 1% of the measured surface value). Table 3 shows calculated K_W values for the two waterholes.

Table 3: Calculated light extinction coefficients K_W (m^{-1}) at Kooroon and Kurmala. Values shown are averaged from three replicates.

	Kooroon	Kurmala
January 2006	20.1	12.4
February 2006	30.1	16.7

2.4.3. Solar shading

The river morphology and vegetation also introduce a shading effect in the early morning and late afternoon sun. The relatively short river width means that the river receives direct solar radiation for only a short period in a day: with early morning and late afternoon inputs not reaching the water (Figure *26*, Webb and Zhang, 1997; McJannet *et al*., 2017).

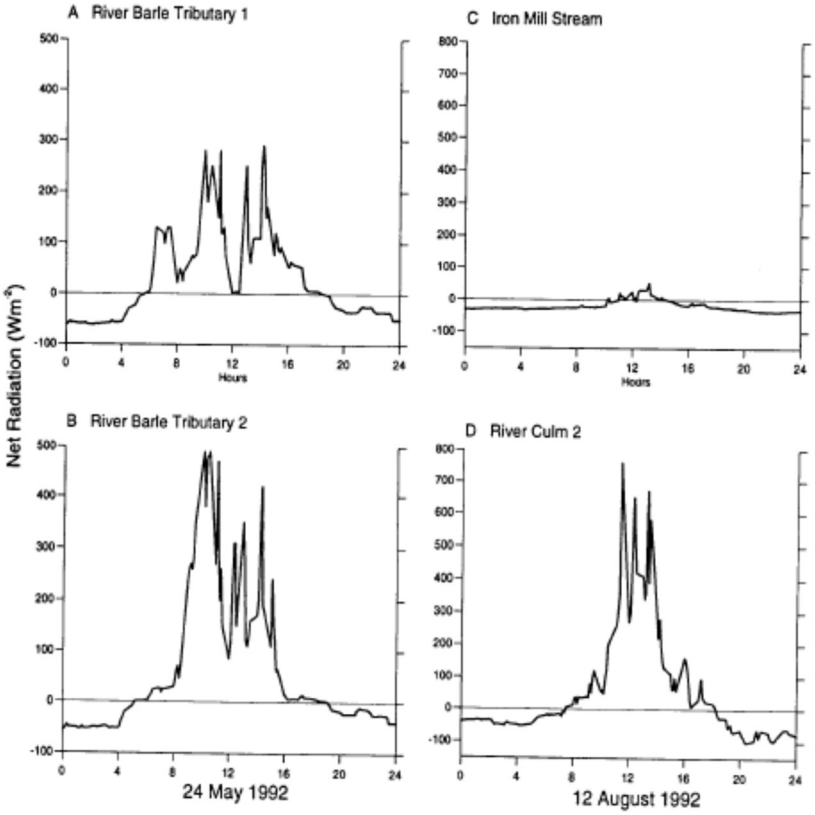

Figure 26*: The effect of river morphology (A: with bank shading, B: no bank shading) and of shading by vegetation (C: with vegetation shading; D: no vegetation shading) on net radiation flux in selected study river reaches. Figure reprinted from Webb and Zhang (1997).*

A study by Garner *et al*. (2017) suggested that channel orientation would have limited impact on net solar radiation received by the water when canopy cover overhanging the stream is <30% (which is the case for sites in this study) or >70%. We also not the meandering nature of these waterholes means that the orientation is heterogenous (changes every ~200 m in the case of Brenda weir pool) and this may be a highly localised effect.

2.4.4. Evaporative cooling and the effect of wind-sheltering

The river hole weather condition could be fundamentally different to the one measured at a regional meteorological station which is usually installed in an exposed area and measured at 10 m above ground, whilst in the rivers the sheltering effects of bank and vegetation need to be considered (Figure *26*). Such sheltering effects can be simulated using several methods in GLM, for example, Hipsey and Sivapalan (2003) presented a simple adjustment to the evaporation model using a shelter index, S_w, to

account for the effect of wind sheltering in small water bodies. S_w ranges from 0 to 1 representing no sheltering through to complete sheltering. The evaporation model using this approximated sheltering index showed excellent agreement with measured evaporation data from a variety of small wind-sheltered water bodies at two agricultural sites, proven to be a useful tool to model evaporation without comprehensive local information. In the study by Hipsey and Sivapalan (2003), S_w for small water bodies fringed by natural vegetation were estimated to be 0.53 – 0.71. These values were used as a reference when applying wind factor $(1 - S_w)$ to the regional weather data during model calibration for the waterholes.

2.4.5. Atmospheric stability

For long time integrations (e.g., seasonal), the bulk-transfer coefficients for momentum (C_D in Eq 9), sensible heat (C_H in Eq 7), and latent heat (C_E in Eq 6) can be assumed approximately constant because of the negative feedback between surface forcing and the temperature response of the waterbody (e.g., Strub and Powell, 1987). At finer timescales (hours to weeks), the thermal inertia of the waterbody is too great, so the transfer coefficients should be specified as a function of the degree of atmospheric stratification experienced in the internal boundary layer that develops over the water (Woolway *et al*., 2017). The stratification in the air column can be parameterised by the Monin-Obukhov stability parameter z/L (Monin and Obukhov, 1954), which is used to define corrections to the bulk aerodynamic coefficients C_H and C_E using the numerical scheme described in Appendix B in Hipsey *et al*. (2019). The transfer coefficients used above are automatically updated if optionally applied within a simulation.

In addition, Eq 6 and Eq 7 apply when sufficient wind exists to create a defined boundary layer over the surface of the water. As the wind tends to zero (the “still-air limit”), Eqs 6 - 7 become less appropriate as they do not account for free convection directly from the water surface. This is a relatively important phenomenon for small water bodies since they tend to have small fetches that limit the energy input from wind.

2.4.6. Oxygen metabolism

Dissolved Oxygen (DO) dynamics respond to processes of atmospheric exchange, sediment oxygen demand, microbial use during organic matter mineralisation and nitrification, photosynthetic oxygen production and respiratory oxygen consumption, chemical oxygen demand, and respiration by other biotic components such as seagrass and bivalves. Other processes impacting the oxygen concentration include the breakdown of DOC by aerobic heterotrophic bacteria to CO_2, whereby a stoichiometrically equivalent amount of oxygen is removed. Chemical oxidation, for example processes such as nitrification or sulfide oxidation, also consume oxygen dependent on the relevant stoichiometric ratio.

The processes described above are superimposed on a dynamic hydro-biogeochemical environment. Atmospheric exchange, for example, are highly linked to the hydrodynamic conditions, affected by winds and currents. The oxygen metabolism in river, lake or wetland is controlled by wind, currents, light & benthic conditions, which alter primary productivity, community respiration, re-aeration and sediment demand (Figure 27).

Atmospheric exchange is typically modelled based on Wanninkhof (1992) and the flux equation of Riley and Skirrow (1974) for the open water:

$$F_{O2} = k_{O2}(C_{air} - C_{water}) \quad (13)$$

where k_{O2} is the oxygen transfer coefficient (m/s), C_{water} (g/m^3) is the oxygen concentration in the surface waters near the interface and C_{air} (g/m^3) is the concentration of oxygen in the air phase near the interface. A positive flux represents input of oxygen from the atmosphere to the water.

One of the key oxygen sinks in the waterhole environment is the sediment oxygen demand (SOD) which, in conjunction with the water stratification, creates a highly hypoxic environment at the bottom of the waterhole and reduces habitat quality for fish. The field data had revealed that SOD in the rivers in the region (Condamine, Balonne and Culgoa; see Davies, 2002) ranged from -70.4 to 4.8 mmol $O_2/m^2/day$.

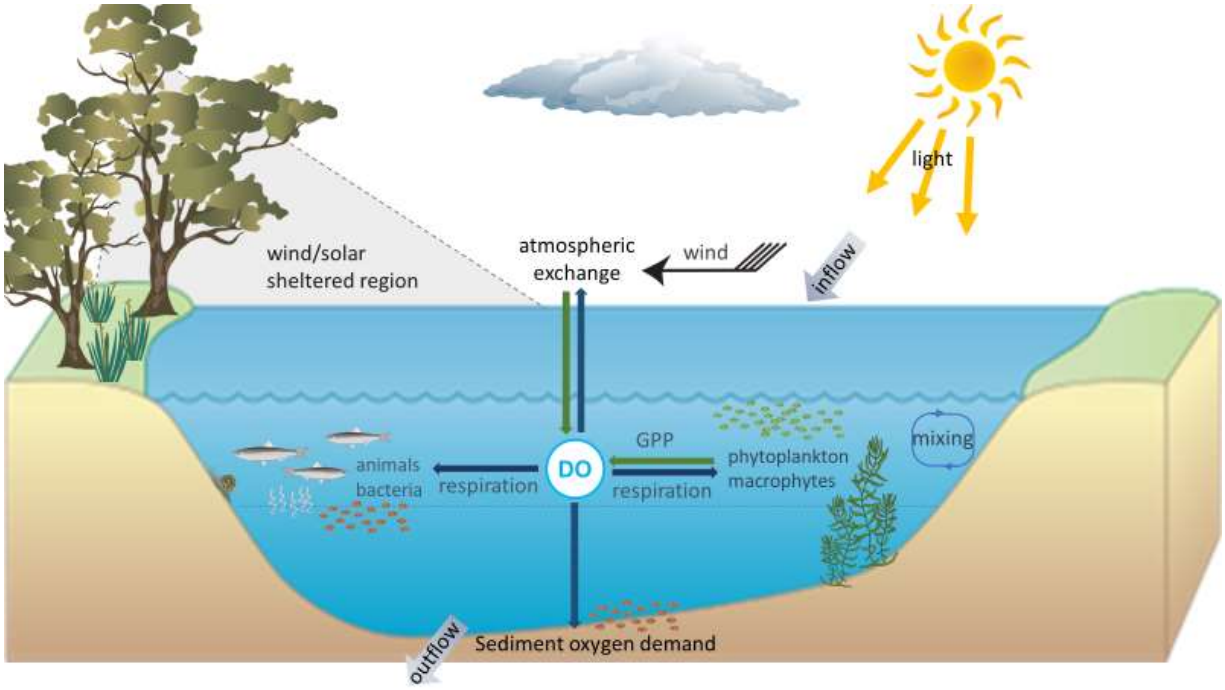

Figure 27: Conceptual model of processes influencing oxygen metabolism in river pools.

These SOD can then be applied in biogeochemical models to estimate the dynamic SOD as a function of the overlying water temperature and dissolved oxygen levels:

$$f_{SOD} = S_{SO} \quad f(T)\, f(DO) \tag{14}$$

where S_{SOD} is a maximum oxygen flux across the sediment-water interface and $f(T)$ and $f(DO)$ are water temperature and DO controlling functions shaping the magnitude of the sediment oxygen demand.

2.5. Waterhole modelling setup and approach

2.5.1. Model platform

In this study we use the General Lake Model (GLM). This 1D stratification model is an open source code designed to simulate the hydrodynamics of lakes, reservoirs and wetlands (Hipsey *et al.*, 2019). GLM computes vertical profiles of temperature, salinity and density by accounting for the effect of inflows/outflows, mixing and surface heating and cooling. GLM incorporates a flexible Lagrangian layer structure similar to the approach of several 1-D lake model designs (Imberger and Patterson 1981; Hamilton and Schladow 1997). The Lagrangian approach allows for layers to change thickness by contracting and expanding in response to inflows, outflows, mixing and surface mass fluxes. Layer thicknesses are adjusted by the model in order to sufficiently resolve the vertical density gradient. Unlike

the fixed grid design where mixing algorithms are typically based on vertical velocities, numerical diffusion of the thermocline is limited, making the GLM approach particularly suited to long-term investigations ranging from seasons to decades, and for coupling with biogeochemical models to explore the role that stratification and vertical mixing play on the dynamics of aquatic ecosystem.

GLM requires a set of meteorological datasets, such as air temperature, short/long wave radiations, humidity, and wind speed/direction, to predict surface thermodynamics and mixing. The BoM regional weather data were approximated to local conditions before being applied to the GLM model (Figure 28). The model was then calibrated against the field temperature profile and surface elevation data to optimise model performance with suitable scaling factor for each climate variable.

The Aquatic Ecodynamics (AED) model was coupled to simulate dissolved oxygen dynamics. The AED modelling library is an open-source community-driven library of model components for simulation of water quality, aquatic ecosystem dynamics as well as terrestrial and aquatic habitats. The AED library consists of numerous modules that are configured according to ecosystem conceptualisations. This application adopts the oxygen module, which simulates dissolved oxygen dynamics accounting for atmospheric exchange and sediment oxygen demand.

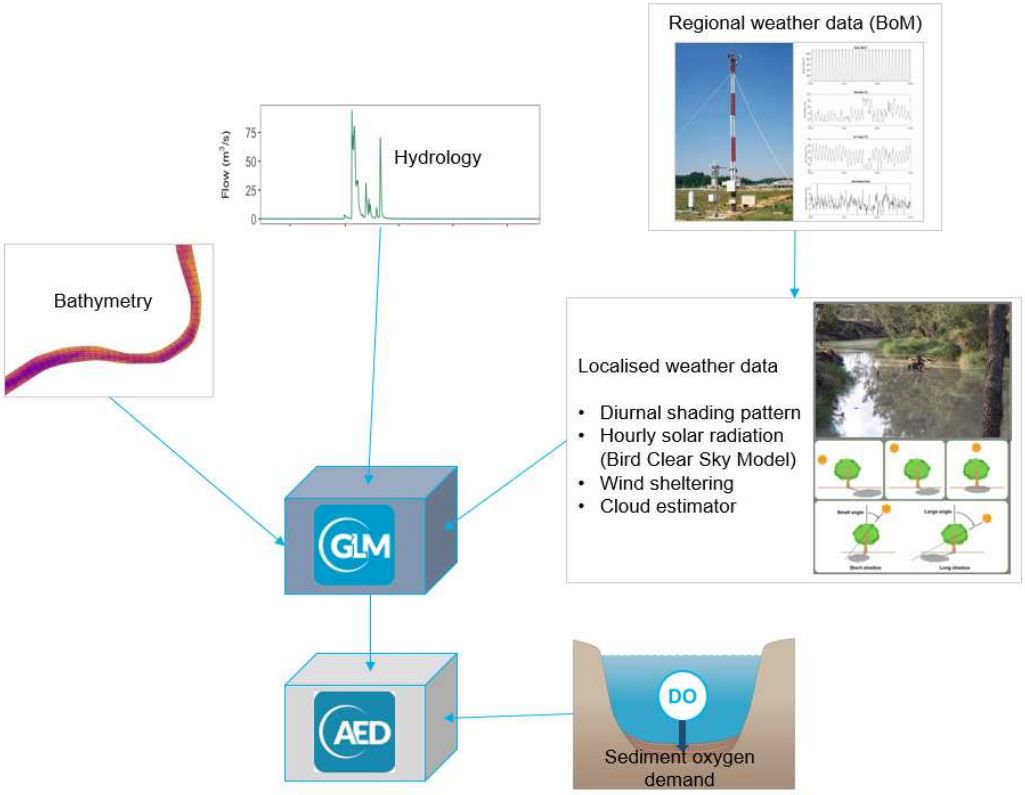

Figure 28: Workflow diagram for the model calibration process.

2.5.2. Weather localisation

Meteorological dataset from BoM St George Airport station (043109) and Miles Constance St (042112) were used as reference conditions as they had the necessary high-resolution data, however initial simulations showed poor predictions when using this directly. An overview of the BoM St George data (Figure 10) indicates a strong diurnal variation with the day/night difference of > 1000 W/m^2 for solar

radiation, > 60% for diurnal humidity and > 10 ˚C for diurnal air temperature. However, the observational data showed that the diurnal mixing was mostly constrained on the top 0.5 - 1.5 m of the water and the range of diurnal changes in surface water temperature is small (Figure 13 and Figure 14), indicating the validity of applying the weather condition from the St George airport need to be further examined. Therefore, the nearby BoM weather datasets were 'localised' to river hole environments by taking the shading and sheltering effects into account. Table 4 lists the BoM dataset used for each climate variable at each site.

Table 4. BoM weather dataset used for each study site. '' indicates data were adjusted for local conditions.*

	Air temperature	Relative humidity	Shortwave radiation	Wind speed	Rain
Kooroon	043109 (St George AP)	043109 (St George AP)	042053 (Flinton)*	043109 (St George AP)*	043109 (St George AP)
Kurmala	043109 (St George AP)	043109 (St George AP)	042053 (Flinton)*	043109 (St George AP)*	043109 (St George AP)
Brenda	043109 (St George AP)	043109 (St George AP)	048212 (Brenda)*	043109 (St George AP)*	043109 (St George AP)
Trafalgar	043109 (St George AP)	043109 (St George AP)	044117 (Dirranbandi)*	043109 (St George AP)*	043109 (St George AP)
Weribone	043109 (St George AP)	043109 (St George AP)	043101 (Weribone TM)*	043109 (St George AP)*	043109 (St George AP)
Reilly's Weir	042112 (Miles Constance)	042112 (Miles Constance)	042098 (Cotswold)*	042112 (Miles Constance)*	042112 (Miles Constance)

Shortwave radiation

Shortwave solar radiation was only available at daily timescale from nearby BOM stations and required disaggregation into hourly intervals. The Bird Clear Sky Model (Bird and Hulstrom, 1981) was used to generate hourly theoretical clear sky radiation for each study site based on latitude, longitude and zenith angle. The daily total clear sky radiation was compared with field daily solar radiation from nearby BOM stations for each site to generate a factor for each day, which were then applied to the hourly clear sky radiation for estimated field hourly radiation. As hourly solar radiation can vary considerably spatially due to changes in cloud cover, solar data were acquired from the nearest BOM station for each site, instead of using St George Airport station for all (Table 4).

Diurnal vegetation shading

The diurnal vegetation shading factor was estimated based on changes of tree shadow length throughout the day due to changes of sun angle. The shadow length is calculated by

$$L = \frac{H}{\tan(a)} \tag{15}$$

where H is tree height, and *a* is the angle between sun and horizon.

For any given day, shadow length is the smallest at midday (12pm), and a factor of 1 was assigned to it. Other times during daylight hours would have a factor greater than 1, which is the ratio of shadow length of that particular hour to the shadow length at midday. The canopy shade percentage at midday was estimated from aerial images for each pool at the logger installation site (Table 5), instead of the whole length of pool, and shade percentage of other times during the day were estimated by applying the shadow length adjustment factor to the shade percentage at midday. An example of adjusted canopy

shade at Brenda on 1/12/2019 is shown in Table 6. The resulting hourly vegetation shade percentage was then applied to the hourly solar radiation time-series described above before feeding into the model. With this approach, the actual tree height is not required as only the adjustment factor is used. However, several assumptions were made: 1) shadow length is a proxy for shade area, which means the surrounding trees/shrubs are assumed to be in a regular rounded shape, as opposed to be in a tall tree form with a bare trunk; 2) vegetation density is similar on both banks. These assumptions are generally met for our study sites based on aerial images and onsite photographs. In addition, due to the windy shape of our pools the orientation of river channel was not considered to impact upon this overall shading pattern significantly.

Table 5: Estimated canopy shade at midday for six pools.

Site	Canopy shade at midday (%)
Kooroon	5
Kurmala	7.5
Brenda	10
Reilly's Weir	10
Trafalgar	10
Weribone	5

Table 6: Example of adjusted canopy shade during daylight hours at Brenda on 1/12/2019.

Date and time	Canopy shade (%)
1/12/2019 6:00	100
1/12/2019 7:00	100
1/12/2019 8:00	100
1/12/2019 9:00	67.7
1/12/2019 10:00	41.2
1/12/2019 11:00	21.3
1/12/2019 12:00	10
1/12/2019 13:00	21.5
1/12/2019 14:00	41.6
1/12/2019 15:00	68.2
1/12/2019 16:00	100
1/12/2019 17:00	100
1/12/2019 18:00	100

Cloud cover

Cloud cover percentage was calculated from the difference between field solar radiation and theoretical clear sky radiation. Since cloud cover could not be calculated during the night, it was assumed to be the same as that of the last daylight hour on that day.

Longwave radiation
Net longwave radiation is described as the balance from incoming flux and efflux (Eq 3). Once the air temperature and local cloud cover were obtained and calculated following the above steps, the longwave radiations from the air to water can then be quantified (Eq 4) and the longwave radiation from water to air can be quantified with the observed surface water temperature (Eq 5).

2.5.3. Model calibration

Water level
Water level was calibrated in GLM 3.1.9 at Kooroon and Kurmala using flow data from the nearby gauge (Moonie_Flinton 417205A). This gauge is located approximately 20 km upstream of Kooroon, but more than 50 KM downstream of Kurmala. As a result, the timing and magnitude in water level change was not expected to match perfectly between modelled and observed at Kurmala.

For the rest of the pools, water level was calibrated without inflow as there was either insufficient field data, or no nearby flow gauge that was fit for purpose. Table 7 shows the calibration period for each site.

Table 7: Calibration period for water level at six study sites.

Study site	Calibration period
Kooroon	1/11/2019 - 5/11/2020
Kurmala	1/11/2019 - 1/6/2020
Brenda	1/10/2019 - 31/1/2020
Reilly's Weir	1/6/2019 - 1/2/2020
Trafalgar	15/6/2019 - 22/7/2019
Weribone	1/10/2019 - 1/1/2020

Temperature
All six pools were calibrated from the dry period between mid/late 2019 and early 2020 before the start of flow events to better capture stratification patterns under no-flow conditions, when fish kill risks are high (Table 8). For pools with longer periods of data (Kooroon and Kurmala), models were also validated until after Cease-to-Flow. To achieve a good fit between modelled and observed thermal patterns, shortwave radiation and wind speed were reduced for all pools (Table 9). Light extinction coefficient was also set to high values to reflect high turbidity in these pools.

Table 8: Calibration and validation period for temperature model at six study sites.

Study site	Calibration period	Validation period
Kooroon	1/11/2019 - 31/12/2019	1/1/2020 - 5/11/2020
Kurmala	1/11/2019 - 31/12/2019	1/1/2020 - 1/6/2020
Brenda	1/10/2019 - 31/1/2020	
Reilly's Weir	1/6/2019 - 1/2/2020	
Trafalgar	15/6/2019 - 22/7/2019	
Weribone	1/10/2019 - 1/1/2020	

Oxygen

Oxygen models were calibrated in AED after the water level and temperature model had achieved satisfactory results. Sediment oxygen demand (`Fsed_oxy` in AED) was calibrated with reference to the range observed in various reaches in the Condamine and Balonne Rivers (Davies 2002). Key parameter values are listed in Table 9.

Table 9: Key parameters in GLM and AED models calibrated for study sites.

	Parameter	Description	Kooroon	Kurmala	Brenda	Reilly's Weir	Trafalgar	Weribone
Water level (GLM)	`rain-threshold`	runoff threshold (m)	0.002	0.005	-	-	-	-
	`catchrain`	runoff from exposed banks of lake area	TRUE	TRUE	-	-	-	-
	`seepage_rate`	seepage rate (m/day)	-0.009	-0.006	-0.007	-0.005	-0.03	-0.006
Temperature (GLM)	`sw_factor`	shortwave factor	0.8	1	1	1	0.9	0.9
	`wind_factor`	wind factor	0.26	0.2	0.2	0.35	0.3	0.2
	`Kw`	light extinction coeff (m^{-1})	10	15	10	5	5	10
	`atm_stab`	atmospheric stability configuration	2	2	2	2	2	2
	`ce`	Latent heat coeff	0.0013	0.0013	0.0013	0.0013	0.0013	0.0013
	`ch`	sensible heat coeff	0.0013	0.0013	0.0013	0.0013	0.0013	0.0013
	`cd`	wind momentum coeff	0.0013	0.0013	0.0013	0.0013	0.0013	0.0013
Oxygen (AED)	`Fsed_oxy`	sediment oxygen demand ($mmol/m^2/day$)	-25	-40	-20	-10	-50	-40
	`Ksed_oxy`	half-saturation concentration of oxygen sediment flux (mmol/m3)	60	60	90	90	60	90
	`theta_sed_oxy`	Arrhenius temperature multiplier for sediment oxygen flux	1.08	1.08	1.08	1.08	1.08	1.08

2.6. Model results

2.6.1. Temperature calibration

Overall, all models have achieved excellent calibration results (Figure 29 to Figure 34; see the Appendix for detailed error analysis and summary of simulation accuracy). The model was able to accurately simulate the range of temperatures observed at each pool, their diurnal fluctuations, strengths of thermal stratification, and mixing dynamics. The water level decreases during dry period due to evaporation and

seepage were also successfully captured. Among the six pools, Kurmala was particularly challenging to calibrate, as the model tended to under-predict in November but over-predict during mid- to late-December (Figure 31). The temperature mooring data at Kurmala showed a relatively stronger stability than other sites with a persist thermal stratification during the study period of November-December …

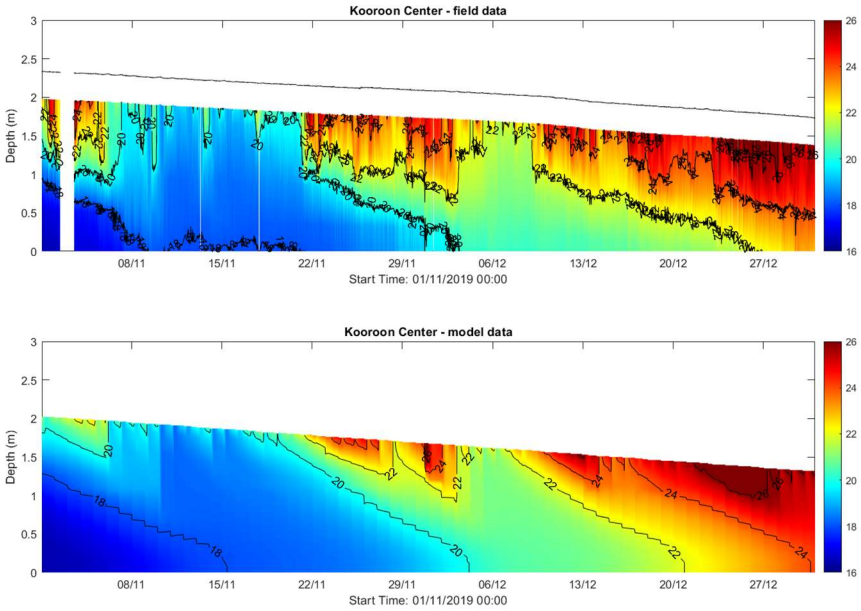

Figure 29: Contour plot of field (top) and simulated (bottom) water temperature at Kooroon. The black line in field data indicates water level. For ease of comparison, top layer was removed in the simulated result to match field data.

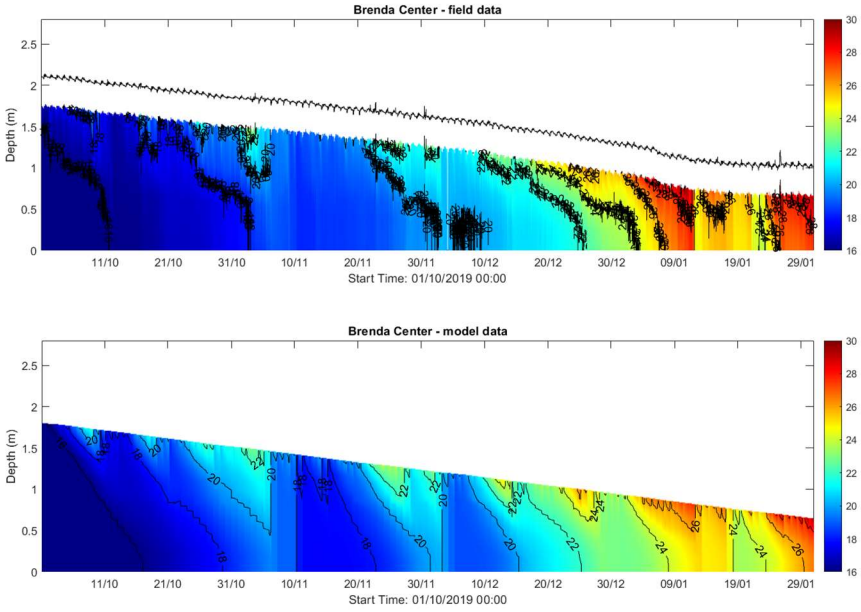

Figure 30: Contour plot of field (top) and simulated (bottom) water temperature at Brenda. The black line in field data indicates water level. For ease of comparison, top layer was removed in the simulated result to match field data.

2019, while all other waterholes presented occasional complete mixing of the water column due to convective overturn or wind stirring. The strong water stability at Kurmala may be due to a strong solar and wind sheltering effects from the shore vegetation, or underground water input to the bottom of the waterhole that sustain the lower water temperature at the bottom. However, we are lack of field data to support these assumptions and had to calibrate the model with the existing weather data. As a result, the calibration at Kurmala was more challenging than other sites.

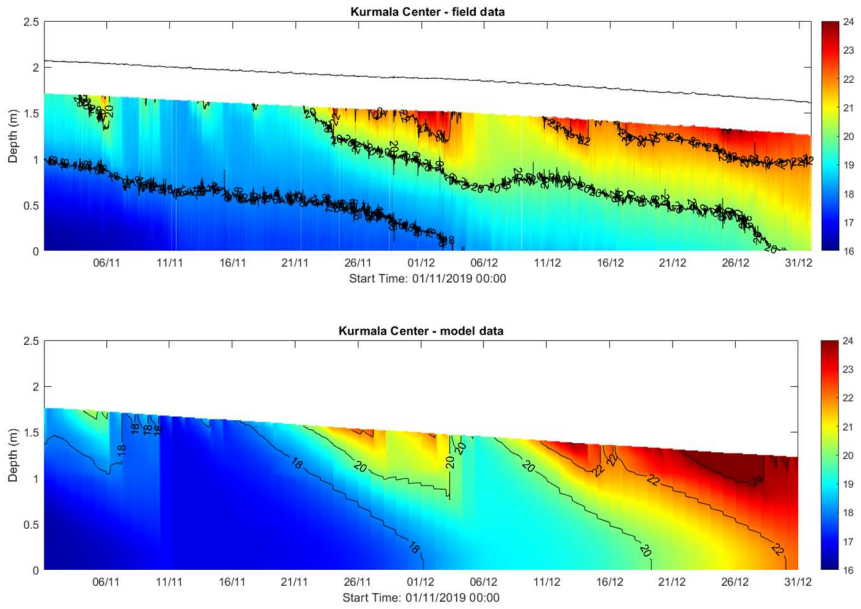

Figure 31: Contour plot of field (top) and simulated (bottom) water temperature at Kurmala. The black line in field data indicates water level. For ease of comparison, top layer was removed in the simulated result to match field data.

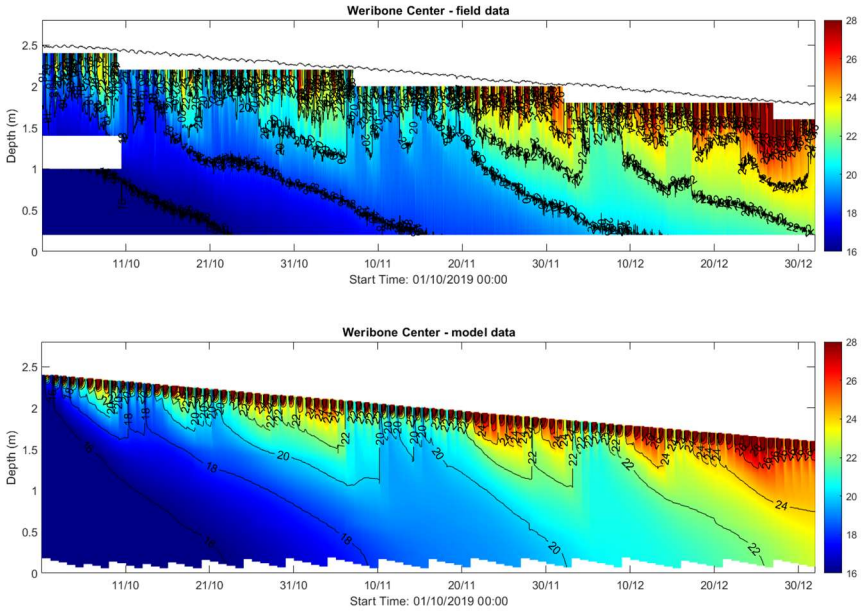

Figure 32: Contour plot of field (top) and simulated (bottom) water temperature at Weribone. The black line in field data indicates water level.

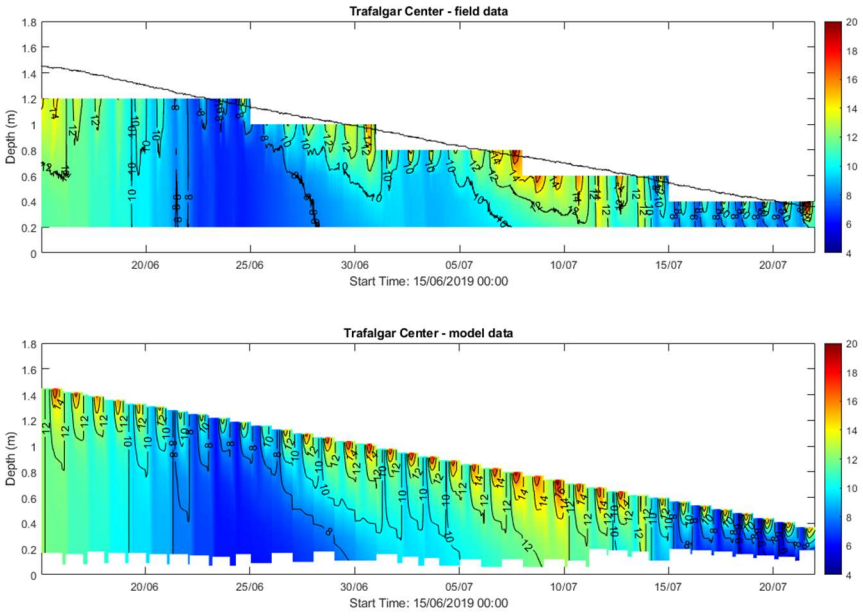

Figure 33: Contour plot of field (top) and simulated (bottom) water temperature at Trafalgar. The black line in field data indicates water level.

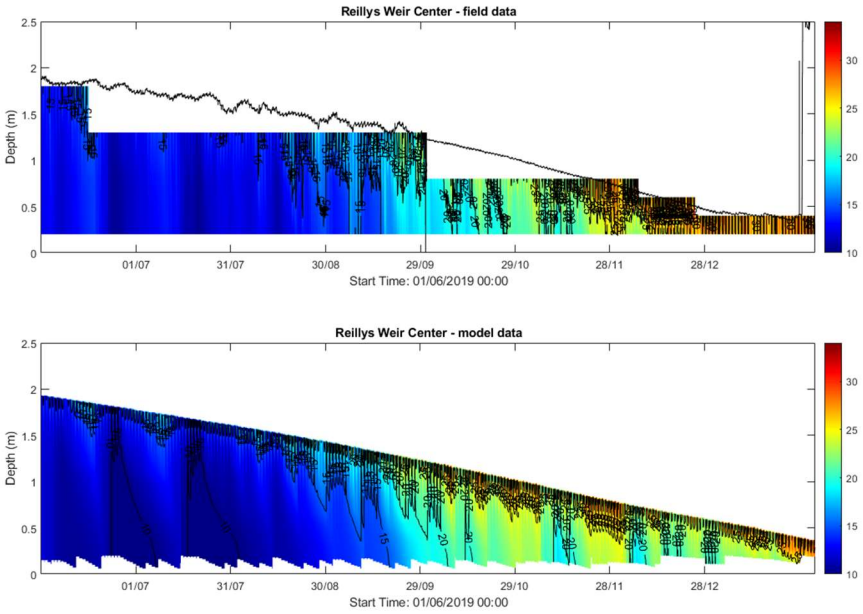

Figure 34: Contour plot of field (top) and simulated (bottom) water temperature at Reilly's Weir. The black line in field data indicates water level.

2.6.2. Temperature validation

Comparison between field and simulated water temperature for Kooroon and Kurmala during the validation period are shown in Figure 35, Figure 36 and Appendix. The model successfully captured the magnitude of water level change due to inflow and precipitation at both pools. At Kooroon, the modelled first inflow (mid-January 2020) was slightly ahead of that observed since the inflow data used was from 20 km upstream (gauge ID 417205A). Temperature profiles were well represented in the model during the wetter period, all through to the recommencement of stratification in September – October. At Kurmala, there was a delay in the first flow event (late-January to early February 2020) in the model due to flow gauge (ID 417205A) being over 50 km downstream of Kurmala. Simulated temperature profiles were generally in agreement with the field data. However, mixing during inflow events were stronger in the field than modelled at both sites.

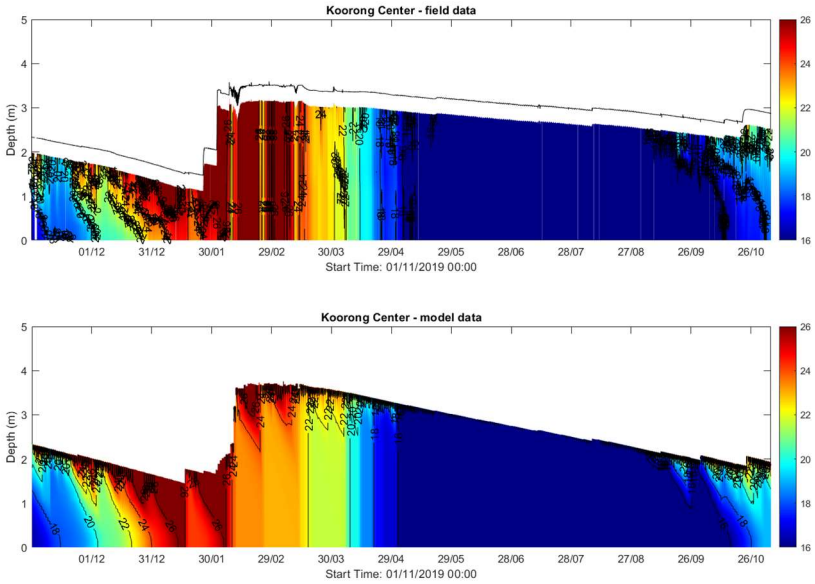

Figure 35: Contour plot of field (top) and simulated (bottom) water temperature at Kooroon. The black line in field data indicates water level.

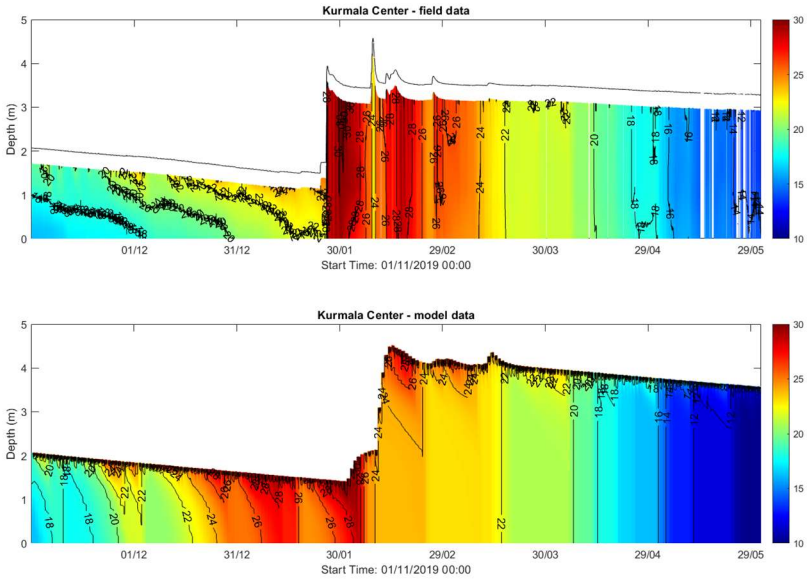

Figure 36: Contour plot of field (top) and simulated (bottom) water temperature at Kurmala. The black line in field data indicates water level.

2.6.3. Oxygen

Overall, most pools achieved good calibration results (Figure 37 to Figure 42; Appendix). The oxygen model was able to simulate the range of oxygen saturations observed in these pools, periods of mixing and hypoxic conditions. At Brenda, the model tended to slightly under-predict at the surface in October 2019, but over-predict in late January 2020, when it was anoxic in the field (Figure 38). The Kurmala model under-predicted near the surface but slightly over-predicted below 1.3m depth at times (Figure 39), which could be related to its temperature model, and/or the unique characteristics of this site. The oxygen logger data at both sites presented a stronger diurnal fluctuations than the model predictions, probably due to the models were run with hourly time steps while the logger data were recorded every 10 minutes, therefore the high frequency events of oxygen changes were overlooked by the model. However, the model still well captured the thermocline and the time evolution of stratification during the study periods.

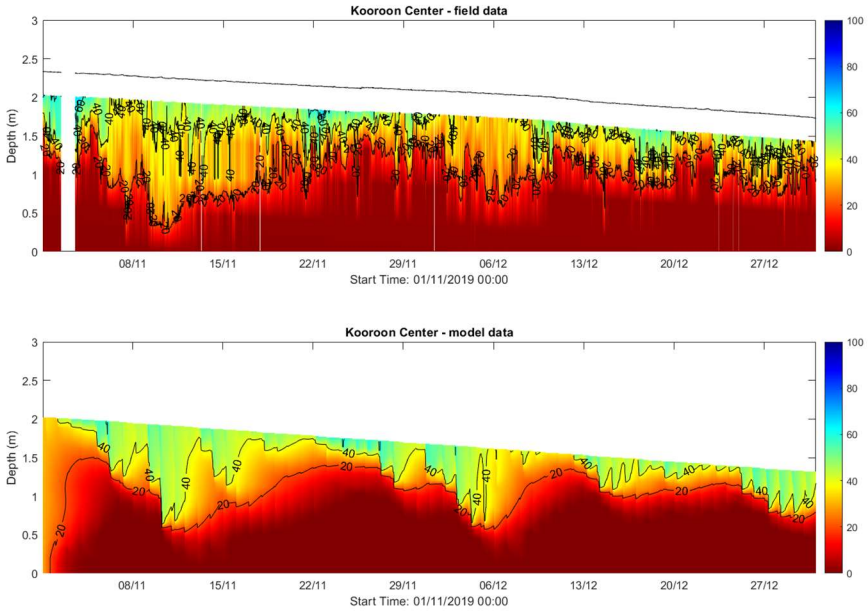

Figure 37: Contour plot of field (top) and simulated (bottom) oxygen percent saturation at Kooroon. The black line indicates water level. For ease of comparison, top layer was removed in the simulated result to match field data.

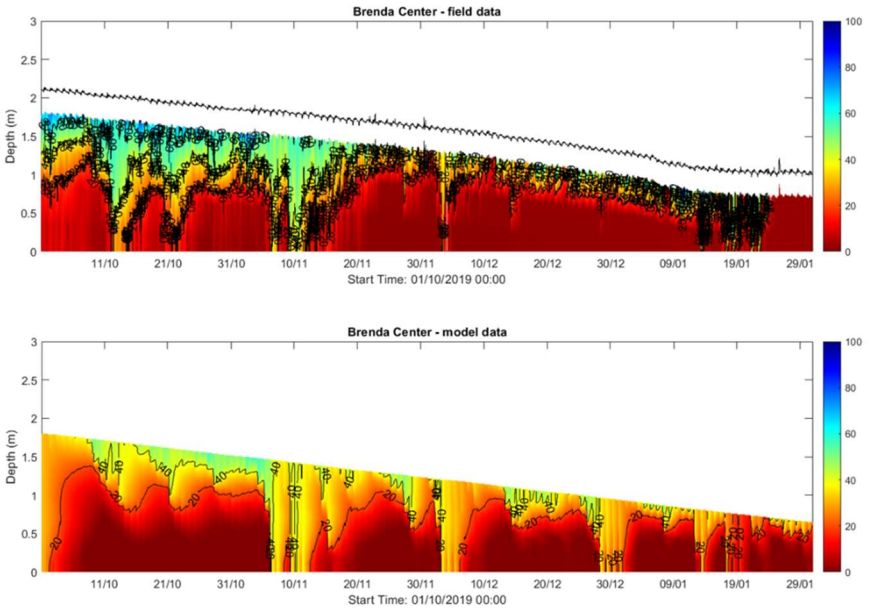

Figure 38: Contour plot of field (top) and simulated (bottom) oxygen percent saturation at Brenda. The black line in indicates water level. For ease of comparison, top layer was removed in the simulated result to match field data.

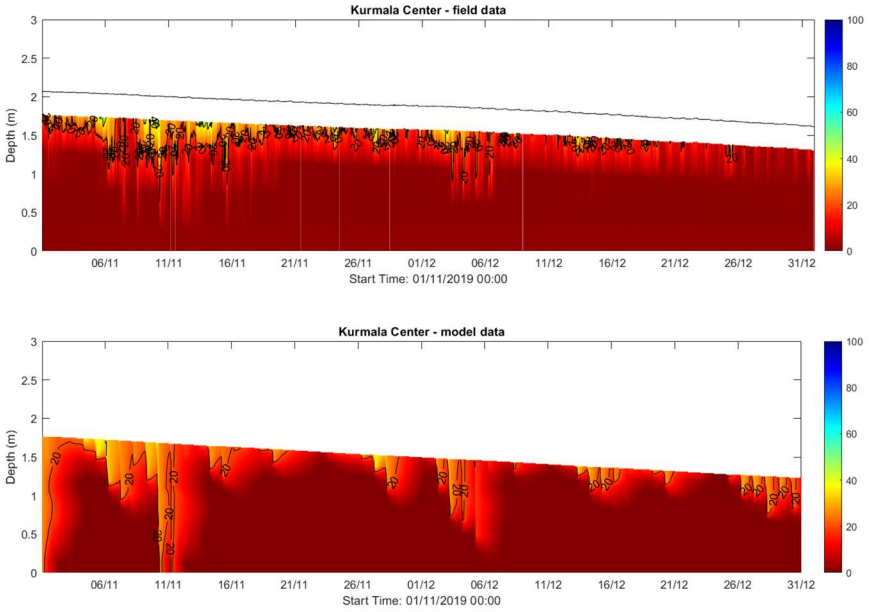

Figure 39: Contour plot of field (top) and simulated (bottom) oxygen percent saturation at Kurmala. The black line in field data indicates water level. For ease of comparison, top layer was removed in the simulated result to match field data.

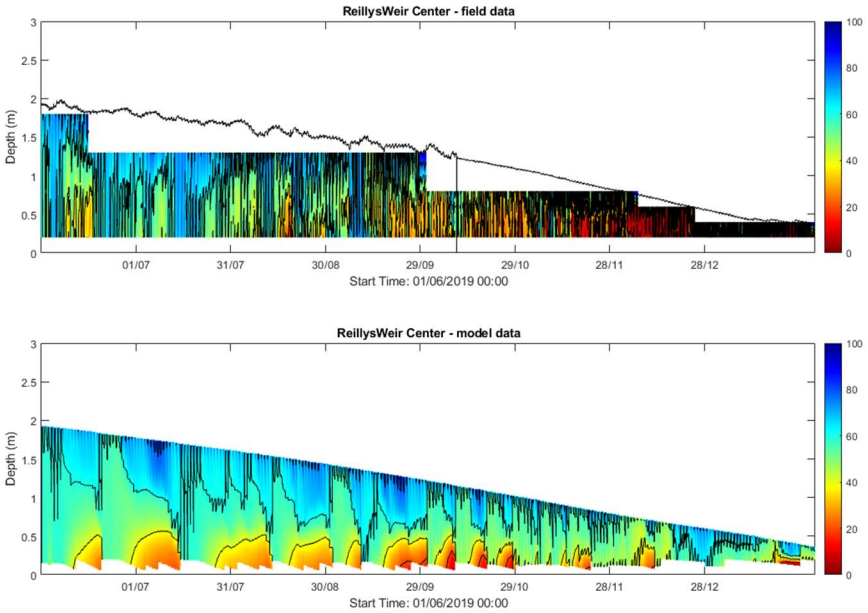

Figure 40: Contour plot of field (top) and simulated (bottom) oxygen percent saturation at Reilly's Weir. The black line in field data indicates water level.

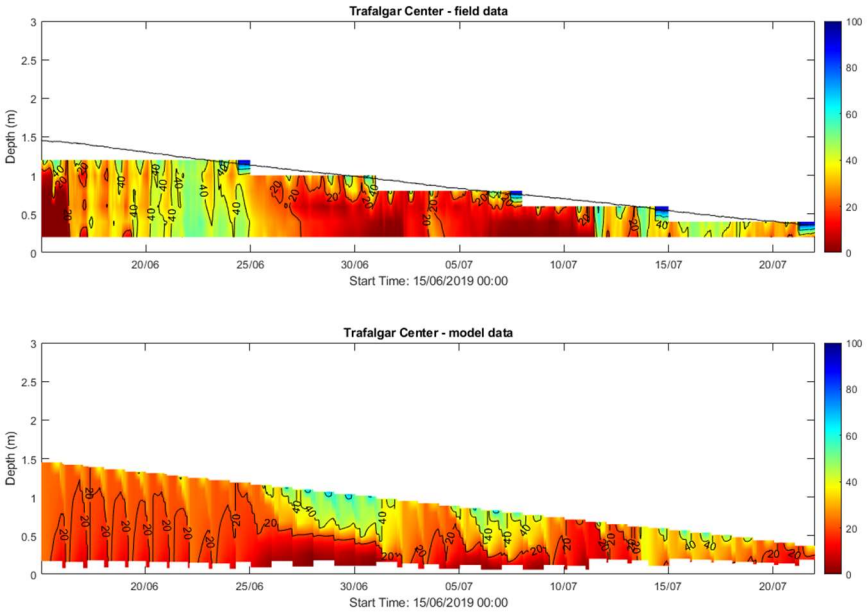

Figure 41: Contour plot of field (top) and simulated (bottom) oxygen percent saturation at Trafalgar. The black line in field data indicates water level.

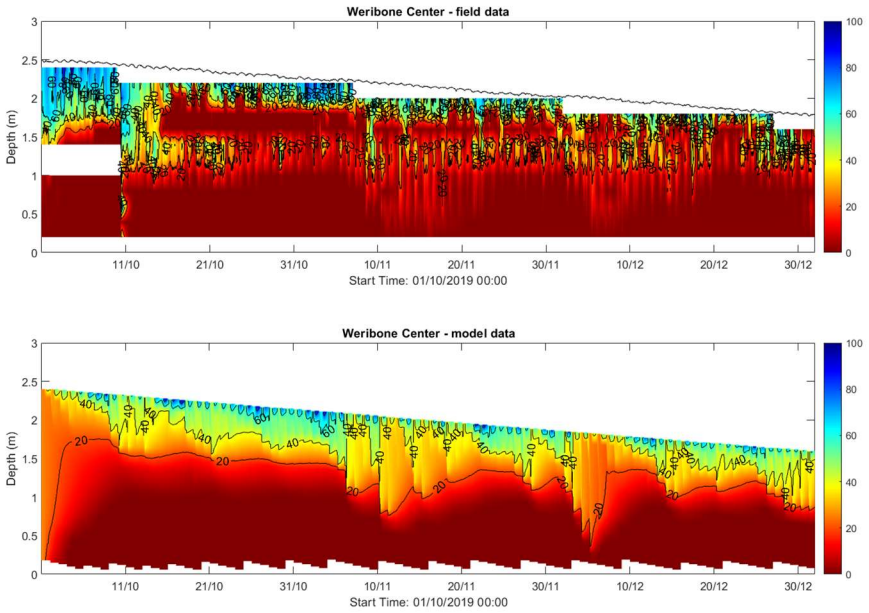

Figure 42: Contour plot of field (top) and simulated (bottom) oxygen percent saturation at Weribone. The black line in field data indicates water level. The layer of zero oxygen at 1.5 – 1.8 m depth was due to logger failure.

2.7. Discussion

2.7.1. Model performance

In general, both temperature and oxygen models performed well in capturing thermal and oxygen stratification and mixing dynamics at all six waterholes. Adjusting regional BOM weather data to local conditions at each site, in particular solar radiation and wind speed, was crucial in resolving heat balance discrepancies. This highlights the distinct local climate each waterhole experiences due to the combined effects of river morphology and canopy cover that provide various degrees of solar shading and wind sheltering. A post-hoc comparison of water temperatures with and without hourly canopy shade at Weribone suggested that even though the estimated canopy shade was only 5% (at midday), by removing the canopy shade, there was an increase in water temperature of approximately 2 – 4°C in warmer months (November – December), and an increase in stratification strength (Figure 43).

It was noted that even after accounting for diurnal vegetation shading, an adjustment factor of less than 1 for shortwave radiation was still required at some sites. This means there were possibly other local factors affecting heat balance components that were not fully resolved in this model, such as shading from elevated riverbanks.

Good performance was achieved at all sites for both the stratification and oxygen model by using a wind adjustment factor between 0.2 and 0.35, which agrees with the reference wind-sheltering index (Hipsey and Sivapalan 2003). The calibrated oxygen demand (Fsed_oxy) was also within the range observed in the Condamine and Balonne rivers from benthic chambers (Davies 2002). However, while a good model fit was achieved by using the reference light extinction coefficient (K_w) at Kurmala, it was less effective for Kooroon. When using the reference K_w for Kooroon (between 20.1 and 30.1, Table 3), the model

tended to cross its mixing threshold more readily than observed, especially on a windy day. Applying a lower wind factor could compensate for this in the stratification model but would subsequently underpredict dissolved oxygen near the surface. A K_w value of 10 was found to produce satisfactory results, which was considerably lower than the calculated value. One possible reason could be that the reference values were derived from measurements taken in January and February, whereas the Kooroon model was calibrated for November and December. A closer inspection of the K_w measurements revealed that there was limited variation among replicates, but large variation between January and February (50% increase from January to February), suggesting considerable temporal variation of K_w at Kooroon.

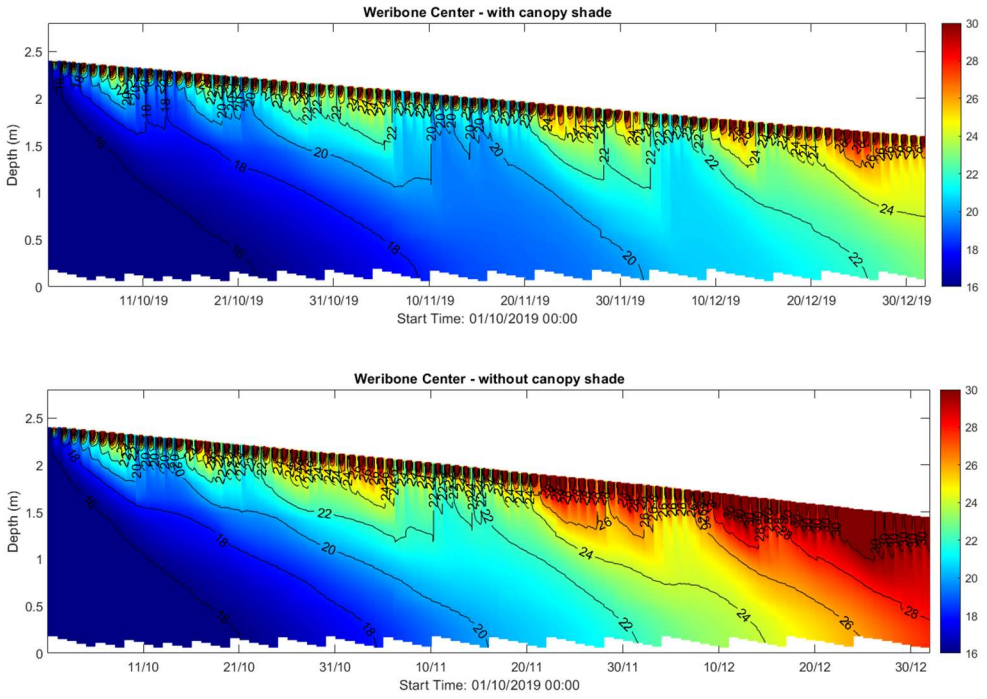

Figure 43: Simulated water temperature at Weribone with hourly canopy shade (5% at midday, top) and without (bottom).

2.7.2. Limitations

Field data review and modelling work suggested the bank shading and wind sheltering effects altered the local weather condition which subsequently affected the vertical mixing of waterholes. However, local weather conditions were approximated from weather records at nearby weather stations, which were mostly between 70 km and 170 km away from study sites. Local measurements of key meteorological parameters such as shortwave radiation and wind speed at the surface of waterholes is therefore recommended to quantify the shading and sheltering effects accurately and improve model robustness.

Field observations and the GLM predictions also indicated high turbidity, high levels of light attenuation, and strong stratification at the surface. Shortwave radiation decayed quickly with water depth, however,

the current monitoring system at Kooroon, Kurmala and Brenda did not record the top 0.3 m layer. Consequently, the models are not calibrated to this top layer. Similarly, at Reilly's Weir, Weribone and Trafalgar, data in the top 0.5 m layer was lost during the dry period due to the logger chain configuration. Key information may be lost not only on thermal stratification in the top layer but also peak water temperatures near the surface which could be an important niche and/or refuge for aquatic life under hypoxic conditions. Therefore, more sensors installed in the top layers is recommended to resolve the sharp stratification phenomenon. Also, better understanding of temporal variability in turbidity driving light attenuation would improve model accuracy.

The main purpose of this modelling study was to capture stratification and oxygen dynamics during the dry period when waterholes are at high risk of developing hypoxia conditions, therefore models were only calibrated to a relatively short period (two to six months). For longer-term simulations that include both the dry and wet periods, flow gauge data in the vicinity of each pool are needed.

It is important to note that for the three pools with less accurate bathymetry data, i.e. Reilly's Weir, Trafalgar and Weribone, a generic lake morphometry was assumed, only considering the overall length, width and depth of each pool. It was discovered during the calibration process that lake morphometry has a considerable effect on temperature profiles through time. Therefore, incorporating bathymetric data is recommended to further improve model reliability at these sites.

Water level was calibrated without distinguishing natural or anthropogenic causes, such as groundwater seepage or water abstraction by local residents, respectively.

Finally, the oxygen model adopted here was simplified by not accounting for littoral productivity that can add oxygen to the water under in certain configurations.

Extending the approach to use a 3-D hydrodynamic model (e.g. TUFLOW-FV) is also recommended to explore the spatial variability within pool reaches and to allow site-specific restoration scenarios to be explored.

2.7.3. Implications for management

This modelling study has highlighted some considerations for the management of oxygen and temperature regimes to support fish in refuge waterholes. The results suggest that even a small increase in waterhole shading can significantly reduce peak water temperature and the duration of stratification raises possibilities that restoration of riparian vegetation or even in emergency situations, artificial shading of waterholes, could help lessen risk to fishes during climate extreme events (Figure 44). Similarly, given the importance of local wind conditions in governing stratification, the feasibility of local solutions to alter wind speeds at the surface of waterholes could offer innovative management possibilities worthy of future consideration.

Finally, given extreme limitation of waterhole dissolved oxygen at times that we both measured and modelled, and the critical role of these waterholes in maintaining viable populations of fishes in dryland rivers, on occasion it may become necessary to implement artificial mixing (Figure 45). This approach was implemented by the New South Wales Government during the extremes of the 2018-2020 drought to help reduce the risks of additional mass fish kills in the Darling River system (Baldwin, 2019). However further research, potentially including use of our models to simulate their effects, are required to understand the effectiveness of artificial aeration in waterholes in providing benefits to fishes.

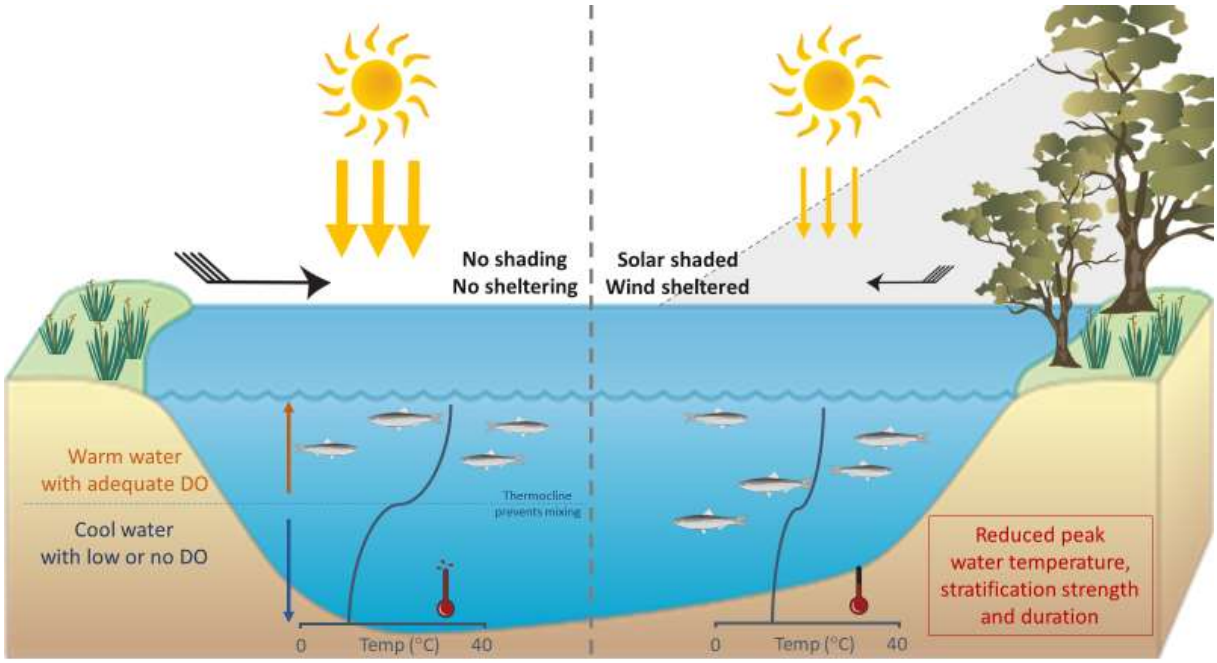

Figure 44. Conceptual diagram showing the effects of vegetation shading on waterhole stratification.

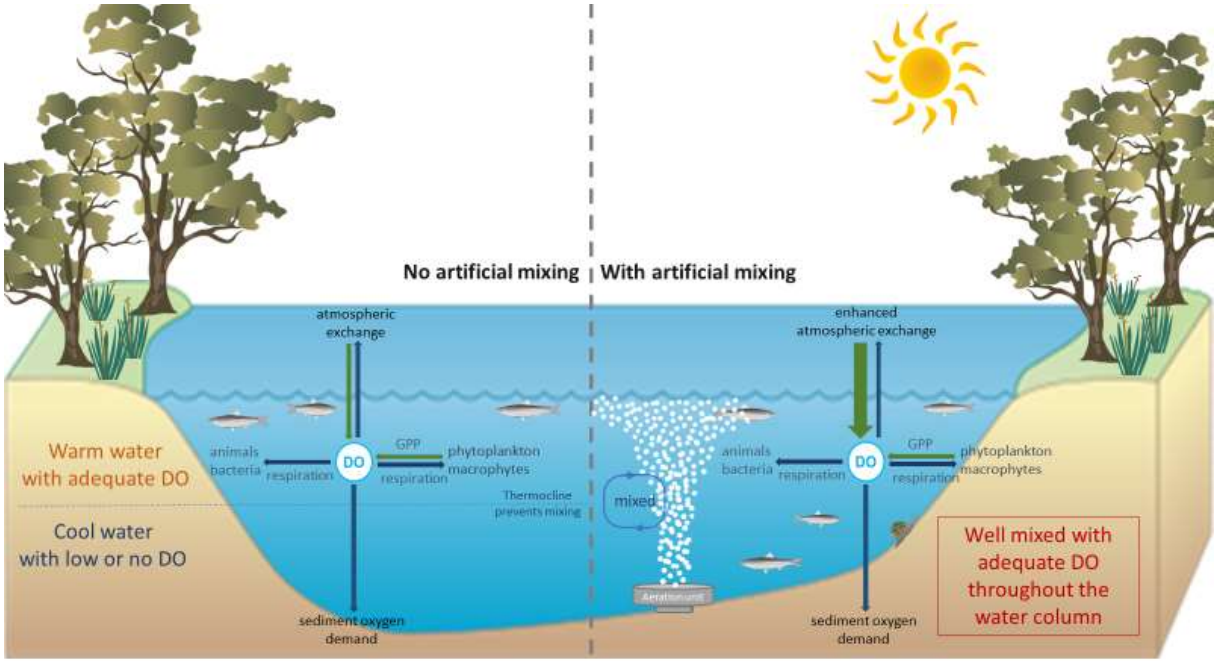

Figure 45. Conceptual diagram showing the effects of artificial mixing on waterhole oxygen dynamics.

3. Assessing fish-kill risk in inland river waterholes: linking ecophysiology and ecohydrology in Northern MDB rivers

3.1. Introduction

Anthropogenic climate change threatens to significantly reduce the functionality of freshwater ecosystems and the biodiversity that they support (Bond *et al.*, 2008, Pittock *et al.*, 2011). Unprecedented rates of climate warming have contributed to an increased frequency, intensity and duration of droughts, as well as increased rates of evapotranspiration, reductions in groundwater recharge and significant increases in mean water temperatures (Aldous *et al.*, 2011). In addition, agricultural, domestic and industrial extraction requirements contribute to a growing pressure on freshwater rivers and catchments in Australia's Murray Darling Basin. The complexity of maintaining water security in a highly dynamic and rapidly changing waterway has placed aquatic species that depend on this system under intense pressure. Naturally extreme hydrological flow regimes, combined with large scale infrastructure such as dams and weirs, have resulted in a significant loss of connectivity and increased isolation of refuge waterholes in the northern MDB. These waterholes serve as critical refugia for freshwater fish species during extended dry periods. However, during protracted low-flow periods, these refuge waterholes can become highly stratified (Section 2.1) making them susceptible to acute hypoxic events that can result in mass fish kills. Understanding the tolerance of key fish species in the MDB for low aquatic oxygen and elevated water temperatures can help to define the physiological boundaries constraining animal health and survival in waterholes. In this section, we combine fish ecophysiological data from three key native species and one invasive fish species with the waterhole models developed in Section 2 to develop a habitat suitability index that can be used to understand waterhole health now and into the future.

Aquatic hypoxia and water temperature are the principal environmental factors affecting the aerobic functioning of water-breathing ectotherms (Ern, 2019). As ectotherms, fish performance typically increases with increasing environmental temperature up to an optimum after which further increases in

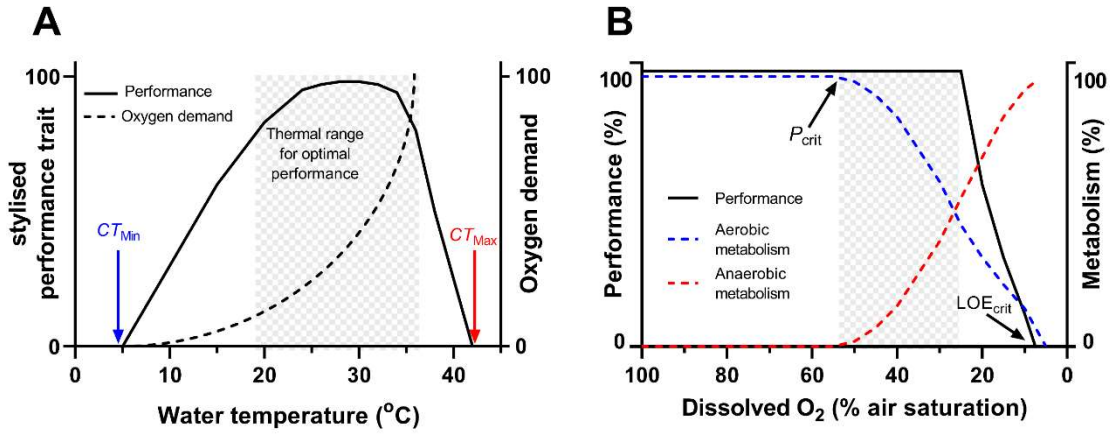

Figure 46: Fish physiological performance is tightly linked to both environmental temperature and aquatic oxygen levels. (A) As ectotherms, physiological performance and oxygen demand increase with increasing environmental temperature up to a performance optimum (grey shaded area). When increasing oxygen demands can no longer be met, performance declines. (B) For most fish, performance is defended against declining aquatic oxygen levels until energy demands cannot be met through aerobic metabolism alone (P_{Crit}). Use of anaerobic metabolism can sustain performance for a short time (grey shaded area), but not indefinitely (LOE_{crit}).

environmental temperature are accompanied by a sharp drop in performance (Figure 46A). Likewise, their requirement for oxygen to fuel aerobic performance is also positively correlated with environmental temperature. Increasing water temperatures directly increases the demand for oxygen by fish, but decreasing oxygen solubility means that oxygen availability declines with increasing temperature. The link between water temperature and reduced oxygen availability during hypoxia has formed the basis of a controversial oxygen and capacity limitation of thermal tolerance hypothesis (Portner *et al.*, 2010) which suggests that the maximum thermal tolerance of ectotherms is dependent on their ability to maintain oxygen supply to fuel aerobic metabolism.

Hypoxia compounds the negative effects of elevated temperature on fish performance. Most fishes will maintain aerobic performance with decreasing oxygen availability until such time that energy requirements cannot be met from aerobic metabolism alone (Figure 46B). At this point (termed P_{Crit}) fish increasingly rely on anaerobic metabolism to supply the energy needed to sustain performance. However, anaerobic energy production is inefficient and physiologically costly, and fish are generally unable to sustain performance for long. Fish will attempt to improve oxygen supply by gulping air at the air-water interface (air surface respiration, ASR) and increasing gill ventilation rates. For most fish, an inability to supply sufficient oxygen to fuel performance rapidly results in the collapse of physiological function (LOE_{crit}). As such, the combined effects of elevated water temperature and hypoxia are likely to act synergistically on fish.

Species-specific maximum thermal and minimum DO tolerance limits should at least reflect the local range of conditions experienced by a population, and possibly by the species over its entire geographic range (Bennett *et al.*, 2019). The difference between the environmental conditions experienced by a population and their tolerance limits may be considered their 'safety margin' (Deutsch *et al.*, 2008). Narrow safety margins occur when experienced environmental conditions approach an animals' maximum tolerance limits; consequently, fish with narrow thermal and/or oxygen safety margins are likely at risk from acute extreme environmental events such as heat waves or hypoxic blackwater events. Conversely, species with broad safety margins are likely to be resilient against acute environmental changes. Importantly, physiological plasticity of both thermal and hypoxia tolerances can result in commensurate shifts in maximum tolerance limits over time such that safety margins are preserved against predictable fluctuations in environmental conditions.

In present study, we determined the maximum thermal tolerance limits, minimum dissolved oxygen tolerance limits, the oxygen dependence of thermal tolerance and aerial surface respiration threshold for four key fish species in the Queensland MDB: golden perch (*Macquaria ambigua*), Murray cod (*Maccullochella peelii*), bony bream (*Nematalosa erebi*) and common carp (*Cyprinus carpio*).

3.2. Fish physiology tests

3.2.1. Experimental design and fish collection

Juvenile and adult carp (n = 7, 15 – 20 cm standard length) bony bream (n = 8, 10 – 20 cm standard length) were collected from Dirranbandi and Hebel waterholes and Beardmore Dam using boat electrofishing. Fish were sorted by size into 80 L carboys containing water from collection sites, and transported by road to the Biohydrodynamics Laboratory at the University of Queensland. Fish were held in 400 L tanks at 28°C in filtered Brisbane tap water. Juvenile golden perch (n = 100, 2 – 5 cm standard length) were purchased from a commercial hatchery (Narrabri Fish Farm) and transported to The University of Queensland. Fish were randomly distributed between six 40 L glass aquaria in a 1000 L recirculating system (n = 16 – 18 per tank) with Brisbane carbon-filtered tap water. Three tanks were set to 20°C and three to 28°C. Juvenile and sub-adult Murray cod (n = 40, 0.5 - 20cm) were purchased from multiple commercial hatcheries (9Dorf Farms, Lilydale and Granite Belt Fish Hatchery, Severnlea, QLD, Australia). Cod were housed in 400 L tanks or 40 L tanks according to body size, with half of the

tanks set at 28°C and the other half at 20°C. common carp and cod were fed commercial fish pellets and bony bream and golden perch were fed frozen brine shrimp daily until satiation. Water changes were conducted at least weekly. Fish were held at their respective temperatures for at least four weeks prior to testing. All fish were tested at their acclimation temperatures and all data are reported as means ± standard error unless otherwise stated.

3.2.2.Physiological tests

Maximum thermal tolerance (CT_{max})

Fish were placed into a 45 L test tank maintained at their acclimation temperature for up to 1 h to habituate. Fish were tested in groups of 3 – 4 individuals at a time depending on the species. Temperature was maintained using two submersible 600 W heaters (Aqua Logic, San Diego, USA). Dissolved oxygen concentration (as % air saturation) was monitored using Firesting (Pyroscience, Aachen, Germany) and Fibox (PreSens, Germany) oxygen meters and maintained above 85% by bubbling oxygen from an oxygen cylinder directly into the water bath as needed. A submersible water pump was used to ensure mixing throughout the water bath and a customised cover was created and placed 1 cm below the surface of the water to stop fish from utilising aquatic surface respiration throughout each test. CT_{max} was determined by increasing temperature in the water bath by 0.3°C min^{-1} until they lost equilibrium (LOE), defined as being unable to maintain dorsal-ventral orientation for more than three seconds. Fish were then removed from the test tank and body mass (g) and standard length (cm) was measured. They were then transferred to an aerated water bath at their acclimation temperature until they recovered (~15 min).

Oxygen limited thermal tolerance (PCT_{max})

The oxygen-dependence of thermal tolerance was determined by performing a CT_{max} test at multiple levels of dissolved oxygen (100, 30, 50 and 16% air saturation). Oxygen levels were chosen as representative of conditions in the northern MDB where carp, bony bream and golden perch are known to inhabit. Oxygen levels in the water bath were maintained by bubbling nitrogen gas into the water. Once the desired oxygen level was reached, fish were placed into a 45 L water bath for 1 h to habituate prior to the CT_{max} test being carried out. Fish were tested in groups of 3 – 4 individuals at a time depending on the species. Following LOE, fish were immediately transferred to an aerated water bath for recovery. Body mass (g) and standard length (cm) were measured for each fish after recovery. PCT_{max} was defined as the lowest oxygen tension that caused a significant decrease in a species CT_{max} under normoxic conditions (Ern *et al.*, 2016).

Hypoxia tolerance (LOE_{crit})

Hypoxia tolerance was assessed by lowering oxygen levels in the testing tank with nitrogen gas until fish could no longer maintain equilibrium. Fish were tested in groups of 3 – 4 individuals at a time depending on the species. Fish were transferred into the water bath containing air-saturated water at their acclimation temperature for 1 h to habituate. Nitrogen gas was bubbled into the water to decrease oxygen from 100% to 0% saturation over approximately 90 – 120 min (McNeil *et al.*, 2007). Fish behaviour (gill ventilation rate and attempted use of air-surface respiration) during testing was monitored through one side of the water bath covered with mirror film that prevented fish from being disturbed by the observer. The oxygen saturation where fish lost equilibrium was recorded as LOE_{crit}. Following LOE, fish were immediately transferred to an aerated water bath for recovery. Body mass (g) and standard length (cm) were measured for each fish.

Aquatic surface respiration (ASR)
ASR was recorded during hypoxia tolerance testing. Fish were tested in groups of 2-5. The aquatic oxygen concentration where fish were first observed to actively seek to gulp at the surface of the water. Fish could not access the surface layer of water due to the presence of a submerged lid.

3.2.3.Results

Critical thermal tolerance limits
Fish species were held under the same thermal conditions for at least four weeks prior to testing to facilitate thermal acclimation. While upper thermal tolerance metrics can vary across populations, life history stages, with genotype, etc., immediate antecedent thermal conditions typically account for the majority of variation in this trait. Therefore, differences in thermal tolerance across species most likely reflect actual species differences at the specific acclimation temperatures used.

Carp had the highest CT_{max} of all four species acclimated to 28°C (40.34 ± 0.14°C), followed by golden perch (39.71 ± 0.06°C) and then bony bream (38.2 ± 0.24°C) and Murray cod (38.23 ± 0.12°C) (Figure 47A). The thermal tolerance limits of fish acclimated to 20°C were approximately four degrees lower than those of fish acclimated to 28°C.

Oxygen-dependent thermal tolerance (PCT_{max})
Bony bream, golden perch and Murray cod all displayed oxygen-dependent thermal tolerance, with CT_{max} estimates declining with aquatic oxygen levels below 50% AS. PCT_{max} (Figure 47B,C), the aquatic oxygen concentration where thermal tolerance first declined significantly from that at normoxia, was 30% air saturation for golden perch and Murray cod, and 16% air saturation for bony bream. However, these values should be interpreted cautiously given the small number of dissolved oxygen levels tested. Carp did not display oxygen dependent thermal tolerance and so their thermal tolerances were unaffected by ambient oxygen levels.

Hypoxia tolerance (LOE_{Crit})
Minimum tolerable dissolved oxygen concentrations were on average < 10% air saturation for all four study species (Figure 47D). Carp were exceptionally tolerant of low dissolved oxygen concentrations (LOE_{crit} = 1.05 ± 0.1% AS. The three native species had a similar LOE_{crit} which was on average ~ 7% AS for 28°C acclimated animals (bony bream: 8.4 ± 0.99% AS; golden perch: 6.08 ± 0.27% AS; Murray cod: 6.73 ± 0.54% AS) and ~5% AS for golden perch and Murray cod acclimated to 20°C (golden perch: 5.43 ± 0.09% AS; Murray cod: 4.56 ± 0.37% AS).

Air surface respiration
Fish utilised a variety of behaviours to compensate for declining oxygen concentrations in LOE_{crit} tests. The onset of air-surface respiration is a reliable estimate of the point at which normal aerobic functions can no longer be sustained by dissolved oxygen supplies alone. There was substantial interindividual variability in the DO level at which ASR commenced. For 28°C acclimated animals, golden perch first attempted ASR at the highest average DO level (22.26 ± 4.1% AS), followed by carp (19.44 ± 5.01% AS), bony bream (17.58 ± 3.8% AS) and Murray cod (13.56 ± 1.8% AS) (Figure 47E). There was a significant effect of acclimation temperature on ASR by golden perch, with 20°C animals having a lower first ASR point (12.67 ± 1.14% AS) than 28°C acclimated animals. There was no effect of acclimation temperature on ASR in Murray cod, with 20°C acclimated animals having a similar ASR point to 28°C acclimated animals (12.38 ± 2.95% AS).

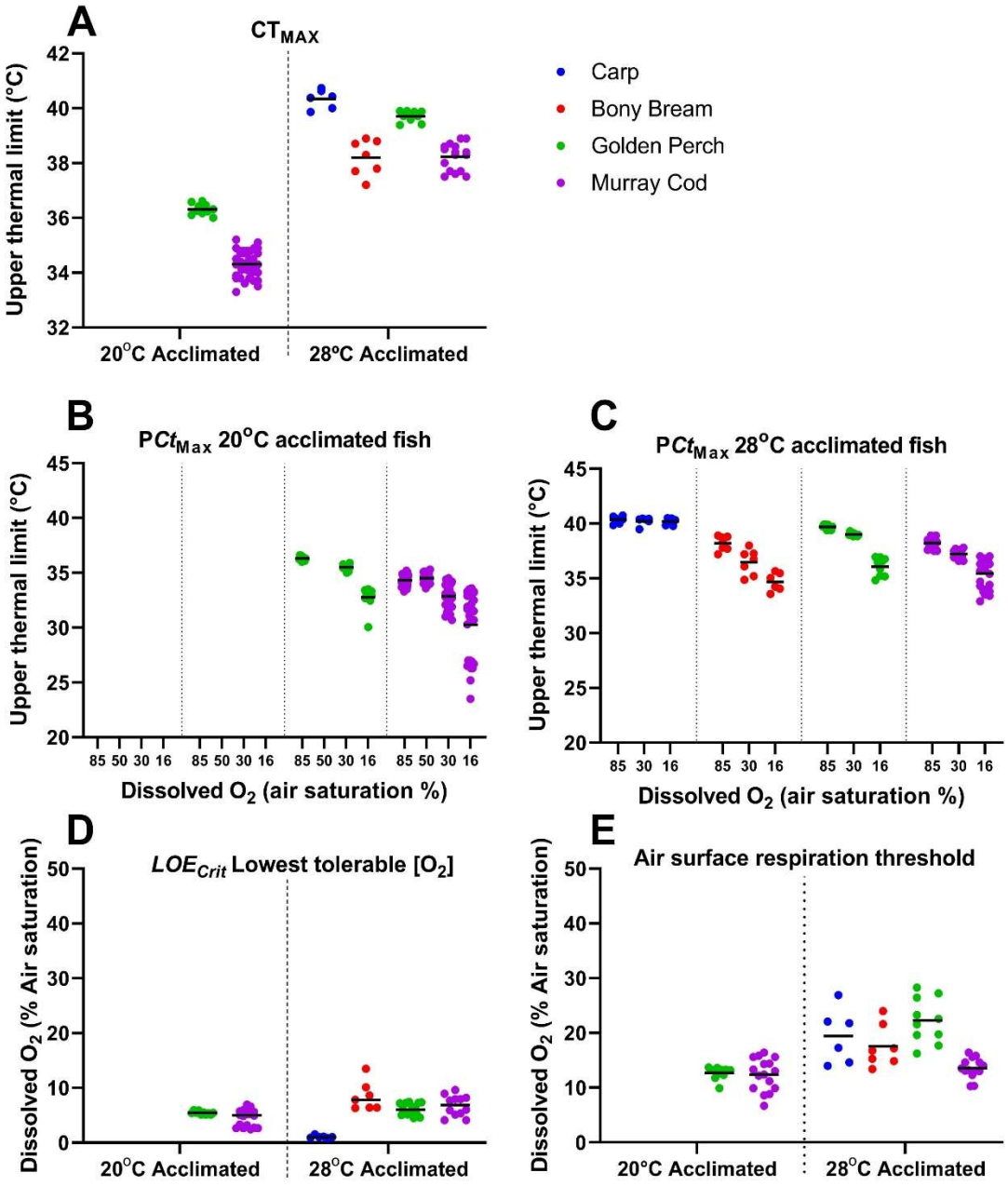

Figure 47: (A) Upper thermal tolerance limits (CT_{max}), (B-C) oxygen-dependent thermal tolerance in 20°C-acclimated fish (B) and 28°C-acclimated fish (C), (D) lowest tolerance dissolved oxygen level (LOE_{crit}) and (E) air-surface respiration threshold for four key fish species in the Queensland MDB. Data are presented as individual data points. N = 6 -30 per species. Horizontal black lines represent treatment means.

3.2.4. Discussion

The physiological tolerance metrics examined here reflect lethal incipient levels - the point immediately preceding death. In reality, animals would rarely experience these conditions in their environments and the difference between the absolute physiological tolerance limit and maximum environmental limit reflects the organisms' physiological safety margin. For all of the examined fish species, the maximum thermal tolerances of fish acclimated to 'summer-like' temperatures were well above those recorded in

the environment suggesting that water temperatures are likely within the thermal safety margin for all study species and consequently, high water temperatures on their own are unlikely to lead to significant fish kill events at these sites. Aquatic oxygen levels, on the other hand, were at or below the lowest tolerable levels for the native species over much of the six waterholes and for protracted periods (narrow safety margins). Native fish displayed hypoxia avoidance behaviours (air surface respiration) at between 15 and 30% air saturation indicating the point at which aquatic oxygen alone can no longer fully support aerobic activities. Combined with field data, these results suggest that native fish are likely exposed to physiologically stressful dissolved oxygen concentrations in many of the waterholes over much of the year. Importantly, during low flow periods, there is a high risk of acute, hypoxia-related fish kills at many of these sites. For carp, however, their capacity to utilise anaerobic respiration for extended periods of time means that they are more tolerant of low dissolved oxygen levels and potentially less likely to succumb to hypoxic blackwater events as readily as the native species.

All three native species displayed a strong oxygen dependence of thermal tolerance, suggesting that interactions between these two abiotic factors need to be considered when assessing physiological tolerance capacities. Importantly, because low dissolved oxygen levels decreased upper thermal tolerance limits for the three native fish species, aquatic hypoxia is likely to reduce the thermal safety margins for these species and make them more likely to experience thermal stress with acute warming events (heat waves). Carp thermal tolerance was unaffected by aquatic oxygen levels, which means that oxygen availability is unlikely to constrain thermal limits in this species.

Use of behavioural compensation strategies and physiological plasticity can ameliorate some of the effects of chronic temperature and hypoxia stress in fish. The current study did not consider compensatory strategies that may alter tolerance thresholds and this is an important consideration for future studies.

3.3. Fish Habitat Suitability Index

Using the above-described waterhole ecohydrology model (Section 2) and fish ecophysiological tolerance limits, we can explore the impact that variability in habitat condition likely has for critical species of interest. Based on a literature review and the physiological data from Section 3.2 that describes the physiological responses of fish acclimated to 28°C to acute temperature and oxygen stress, we developed a Habitat Suitability Index (HSI) algorithm in the AED model library, where 1 indicates optimal conditions and 0 unsuitable.

Specifically, for a given fish species, f, the approach works by first computing the critical oxygen saturation as a function of temperature, O_{PCTmax}, and then assumes suitability follows a Michaelis-Menten formulation in response to dissolved oxygen levels relative to this value:

$$O^f_{PCTmax}[T] = O_{crit} - \propto_f (T_{max} - T) \tag{16}$$

$$HSI_f = \begin{cases} 0, & O < O_{crit} \\ f\left[O^f_{PCT}\right]_f, & O_{crit} \le O \le O^f_{PCTmax} \\ 1, & O > O^f_{PCTmax} \end{cases} \tag{17}$$

$$f\left[O^f_{PCTmax}\right]_f = \frac{\left(O - O^f_{PCTmax}\right)}{\left(K_O + O - O^f_{PCTmax}\right)} \left\{ \frac{\left(100 - {}^f_{PCTmax}\right)}{\left(K_O + 100 - {}^f_{PCTmax}\right)} \right\}^{-1} \tag{18}$$

where:

HSI_f: Fish habitat suitability index, for species *f*
O: Oxygen saturation (%)
O_{crit}: Critical oxygen saturation causing mortality (%) *
T: Water temperature (°C)
T_{max}: Maximum temperature (°C) **
O^f_{PCTmax}: Critical oxygen saturation at temperature (%)
K_O: Half-saturation mediating oxygen sensitivity (%)
$\propto_f$: Thermal sensitivity coefficient

* O_{crit} = LOE_{crit} at the 28 °C acclimation temperature.

** T_{max} = CT_{max} minus 2 °C which assumes that physiological functions are likely compromised before incipient lethal temperatures.

The approach to the calculation is based on the "Oxygen Limitation Hypothesis", which emphasizes that metabolism is constrained by oxygen availability, especially at high temperatures or during intense activity (Rubalcaba *et al*., 2020). Whole-organism fish metabolism is known to scale prediatbly with temperature, and Rubalcaba *et al*., (2020) show that under oxygen limitation it follows a Michaelis-Menten kinetic rate limitation form. Our HSI computation is not directly aiming to capture the metabolic rate response of a fish to oxygen, and so we cannot use the kinetic rate limitation formula provided in Rubalcaba *et al*., (2020), however in Eq 18 we adopted a Michaelis-Menten form linking HSI and oxygen in order to ensure consistency with the theoretical model of metabolism and respiration.

The associated parameter values set for each fish species are listed in Table 10 below. O_{crit} and T_{max} map directly to the experimental results whilst the values of K_O and $\propto_f$ remain unquantified and therefore they were computed based on a manual fitting of Eq 16 and 18 to the available experimental data summarised in Figure 47. Whilst the algorithm did not perfectly fit the laboratory data in all cases the resultant functions generated closely followed the desired intent of capturing the species-specific interactive effects of temperature and oxygen on metabolism (Figure 48). In this figure, note how the results show the relative tolerance of Carp to low oxygen conditions, and the difference in sensitivity of Carp compared to Bony Bream in terms of how their oxygen tolerance declines at higher temperatures.

Table 10: Parameter values for Habitat Suitability Index (HSI) model of each species.

	$\propto_f$	O_{crit} (%)	K_O (%)	T_{max} (°C)
Carp	1	1	2	39
Bony bream	11	8	20	32
Golden perch	15	7	10	34
Murray cod	11	8	20	32

The HSI was used in the dynamic model simulations (which predict the O and T values needed for HSI calculation) to define unacceptable (HSI ≤ 0.2), habitable (0.2 < HSI < 0.8) and optimal conditions (HSI ≥ 0.8) (Figure 48). The resultant index was computed within the model domain at each depth level and at each time step, and used to track habitat suitability over time for each waterhole. We highlight these classifications are arbitrary, and are simply introduced to provide a useful way to compare how certain hydro-climatological conditions shift the relative suitability of a system from an oxygen and temperature point of view.

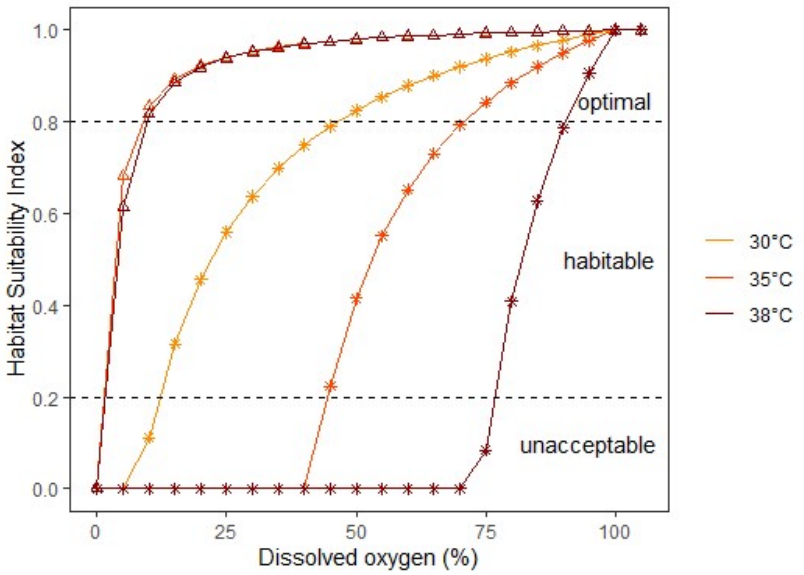

Figure 48: HSI functions for bony bream (*) and common carp (∆) which define optimal, habitable and unacceptable conditions based on their physiological tolerances of oxygen concentration at different temperatures. Only three temperature levels are shown as an example. For native species such as bony bream, tolerance to hypoxic conditions reduces with increasing temperature. As common carp can tolerate extremely low oxygen levels and high temperatures, their HSI functions observe minimal changes with increasing temperature.

Further, as we have bathymetric data for these waterholes, we were able to compute from the model the HSI-weighted "habitable volume" within each waterhole for each species. The total HSI-weighted habitable volume (V_f^{hsi}) of species f in a waterhole is calculated by multiplying the volume of water (V) in a simulated vertical layer, c, by the value of HSI for that layer, and summing across all layers:

$$V_f^{hsi} = \sum_c HSI_c \;\; V_c \tag{19}$$

In our analysis we then inferred from the time-series of habitable volume that periods with a rapid decline in this value (V^{hsi}) would have a high risk of fish-kill occurrences.

3.4. Model application and fish-kill risk assessment

The resultant HSIs and HSI-weighted habitable volume for common carp, bony bream and golden perch at each waterhole are shown in Figure 49 to Figure 54. Murray cod is not shown here as it has very similar physiological thresholds to bony bream. As expected, common carp had the largest amount of good quality habitat in all waterholes compared to native species such as bony bream and golden perch, due to its incredible tolerance to high temperature and low oxygen levels. Kurmala experienced the harshest condition among six waterholes, with its optimal habitat (HSI > 0.8) confined to the top 20 – 30 cm of water column for native species during most of November and December 2019. The calculated habitable volume for bony bream had dropped to zero on two occasions during this period, suggesting high risk of fish-kill events.

For Weribone, Trafalgar and Reilly's Weir, habitable volumes should be interpreted with caution as there was less accurate bathymetry data available and the morphology of these waterholes was approximated in the model.

In summary, the model has shown that while the upper maximum thermal tolerances of all species were well above those recorded in the natural waterholes, the very low dissolved oxygen (DO) levels recorded had the potential to push the native fish species (but not carp) close to their minimum tolerable oxygen limits, particularly in warmer waters. Importantly, waterhole oxygen data shows that for most of the available volume, waterholes were highly hypoxic, being ≤2 mgL^{-1} DO (25% air saturation) for extended periods of time, resulting in very low habitat quality indices.

3.5. Model limitations

Our models were comprehensively validated against temperature and oxygen data that was collected in 6 different waterholes. The fish hypoxia and thermal tolerance thresholds identified in the lab were then applied to predict habitat quality and *infer* fish-kill risk. Importantly, this approach takes into consideration that the physiological tolerance limits measured in standard tests are incipient *lethal* limits and that physiological compromise likely occurs before animal reach these points. Furthermore, whether a fish-kill event occurs is also likely influenced by the cumulative exposure of fish to poor water quality (antecedent conditions), which is subject to their use of avoidance behaviour and physiological plasticity.

Exposure to chronic hypoxia (<2 mgL^{-1}) can be outright lethal to some fish species (Vaquer-Sunyer & Duarte, 2008). For others, it can cause protracted physiological stress which can render them more susceptible to infection and disease, and/or compound the effects of secondary stressors such as heatwaves or toxicants (Abdel-Tawwab *et al.*, 2019). Deleterious effects of exposure to hypoxia include a reduction in aerobic scope (the capacity to sustain aerobic activities such as feeding, reproduction and movement (Claireaux and Lefrançois, 2007; Stefensen, 2006; Poulsen *et al*., 2011), and increased reliance on anaerobic metabolism resulting in acidosis, oxygen debt and reduction in swimming performance (Dutil *et al*., 2007). However, most species have at least some capacity to adjust their behaviour and/or physiology to improve their performance under chronic low DO.

Fish responses to chronic low O_2 conditions can include behavioural adjustments (e.g. moving to a more favourable environment, utilising aquatic surface respiration (ASR), becoming inactive to reduce metabolic (oxygen) demands, physiological compensation (e.g. increased oxygen carrying capacity, acclimation of metabolic rate to manage aerobic scope, changes in cardiac output, increased gill ventilation) and/or morphological (e.g. increased heart size, increased gill surface area)). Deleterious effects of exposure to hypoxia include reduction in aerobic scope and increased reliance on anaerobic metabolism resulting in acidosis, oxygen debt and reduced swimming performance. Our current model does not account for avoidance behaviour which may be an important determinant of a species resilience to the harsh conditions they experience once flow ceases.

For this reason, the results are suitable for facilitating comparative analyses between waterholes, rather than for absolute prediction of the number and frequency of fish-kill events. Further work to use and validate the model against real-world data sets showing fish behaviour (including avoidance behaviour) and fish kills can help refine its accuracy. Laboratory experimental tests exploring the effects of chronic exposure to low oxygen can also help to refine the habitat suitability algorithm.

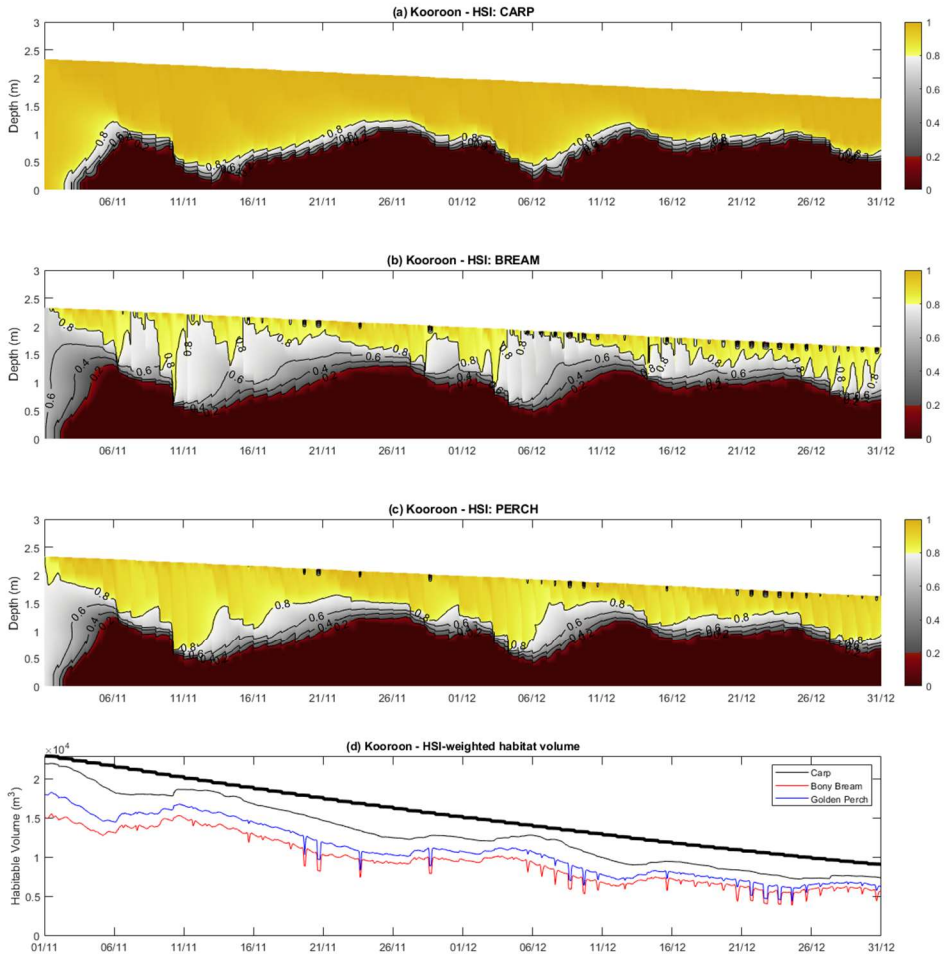

Figure 49: Habitat Suitability Index (HSI) and HSI-weighted habitat volume for common carp, bony bream and golden perch at Kooroon in 2019. A HSI value of 1 indicates optimal habitat conditions while 0 indicates unacceptable conditions. Black thick line in the bottom graph indicates total volume of water.

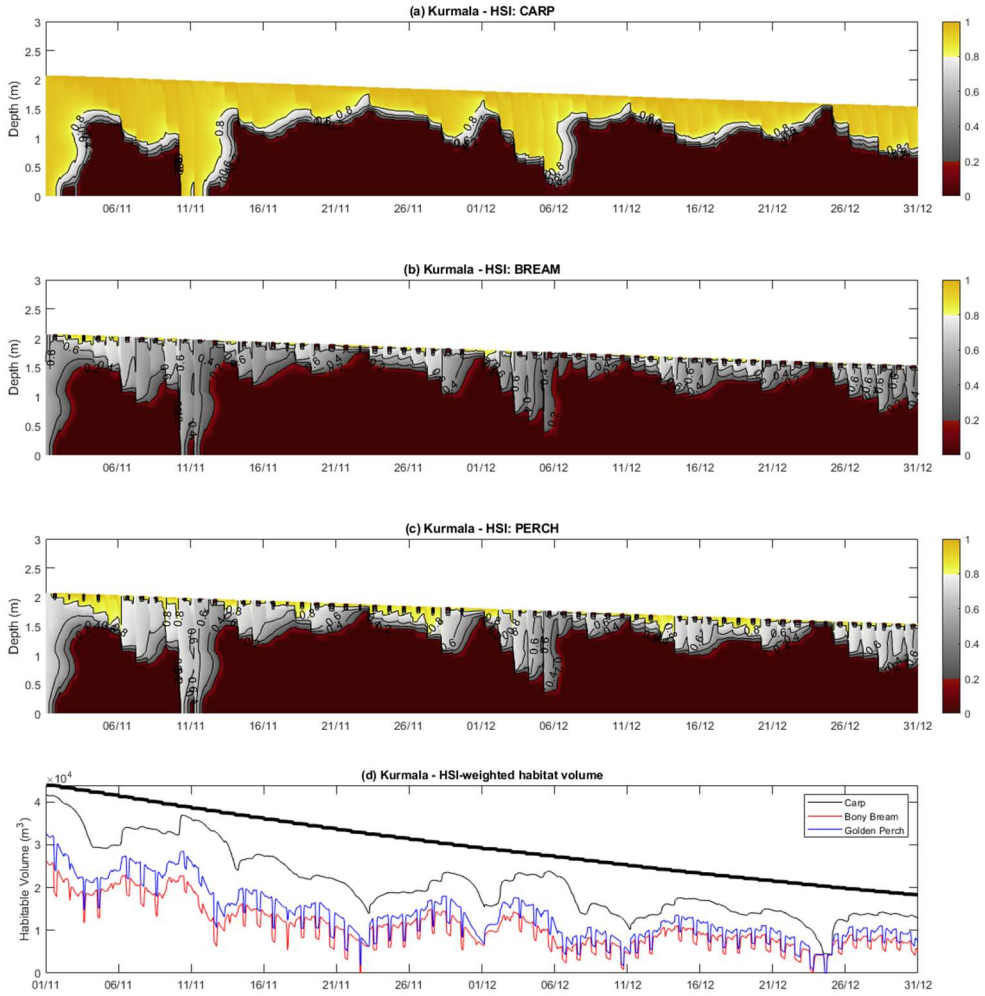

Figure 50: Habitat Suitability Index (HSI) and HSI-weighted habitat volume for common carp, bony bream and golden perch at Kurmala in 2019. A HSI value of 1 indicates optimal habitat conditions while 0 indicates unacceptable conditions. Black thick line in the bottom graph indicates total volume of water.

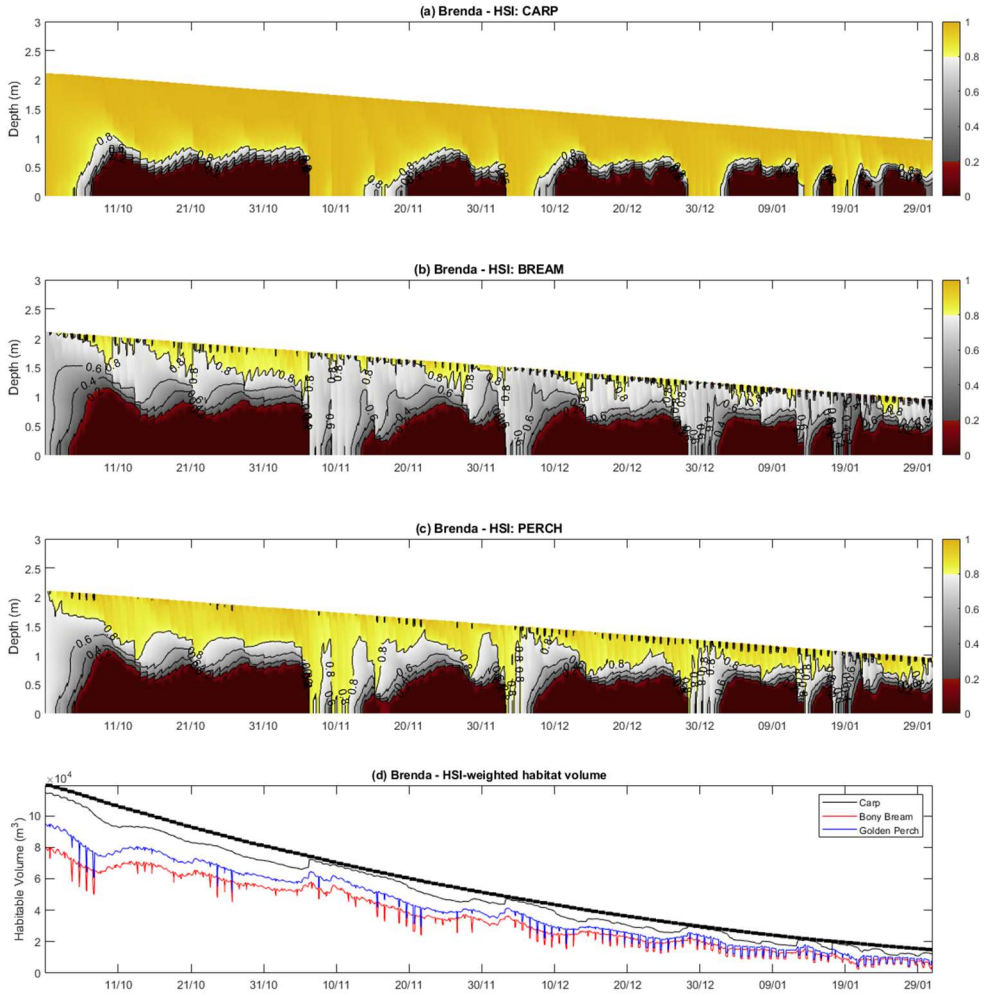

Figure 51: Habitat Suitability Index (HSI) and HSI-weighted habitat volume for common carp, bony bream and golden perch at Brenda in 2019 - 2020. A HSI value of 1 indicates optimal habitat conditions while 0 indicates unacceptable conditions. Black thick line in the bottom graph indicates total volume of water.

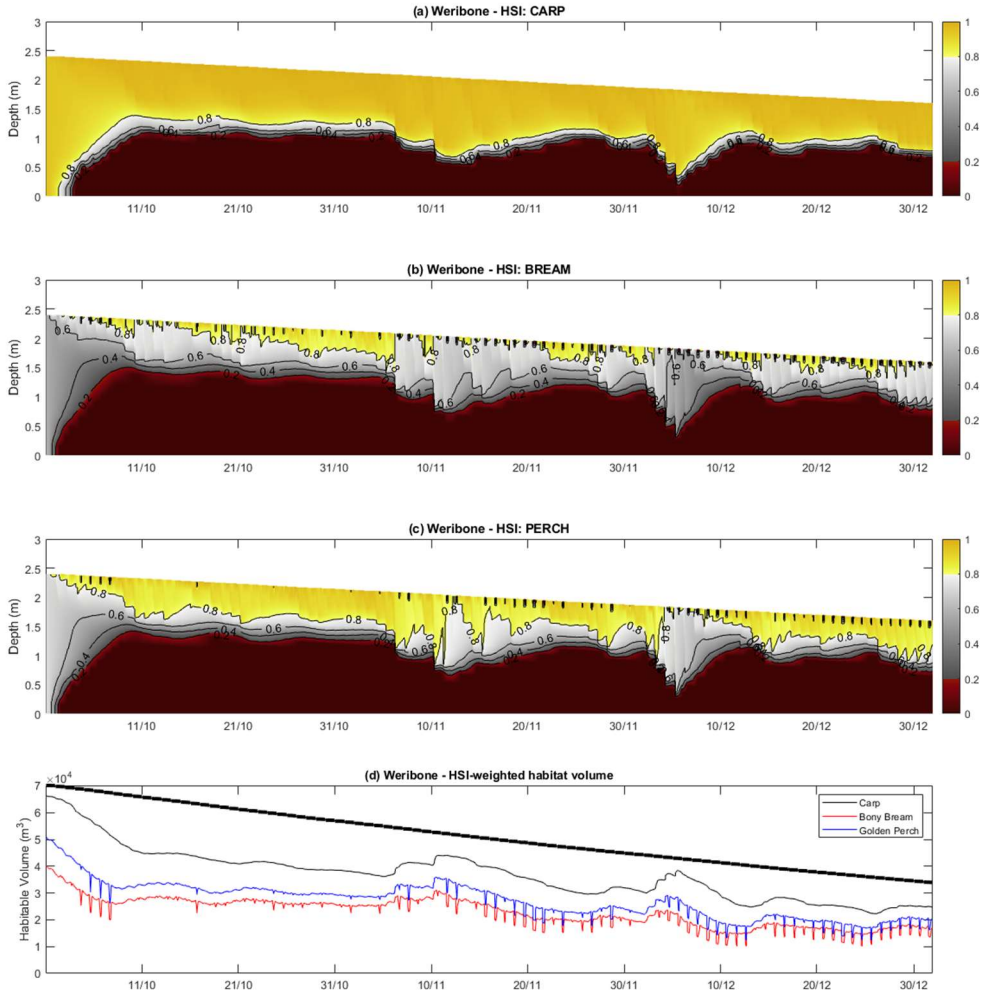

Figure 52: Habitat Suitability Index (HSI) and HSI-weighted habitat volume for common carp, bony bream and golden perch at Weribone in 2019. A HSI value of 1 indicates optimal habitat conditions while 0 indicates unacceptable conditions. Black thick line in the bottom graph indicates total volume of water.

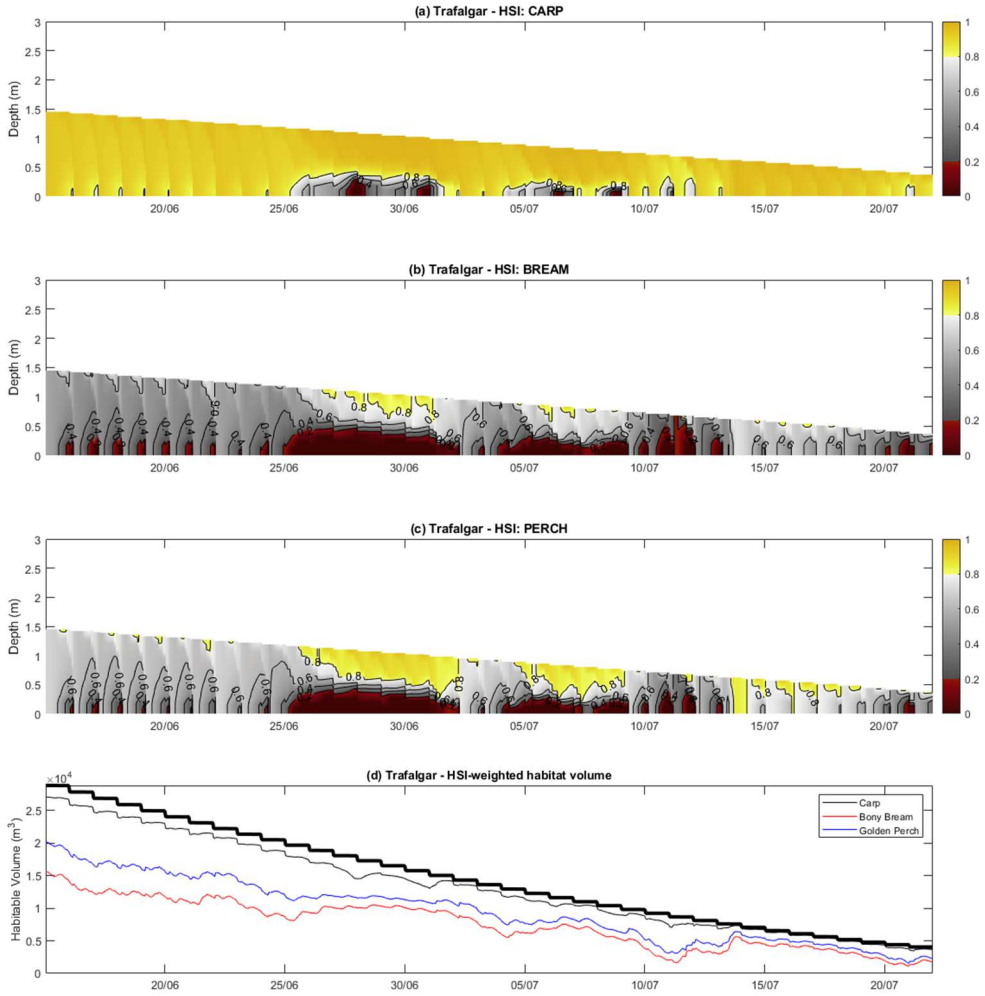

Figure 53: Habitat Suitability Index (HSI) and HSI-weighted habitat volume for common carp, bony bream and golden perch at Trafalgar in 2019. A HSI value of 1 indicates optimal habitat conditions while 0 indicates unacceptable conditions. Black thick line in the bottom graph indicates total volume of water.

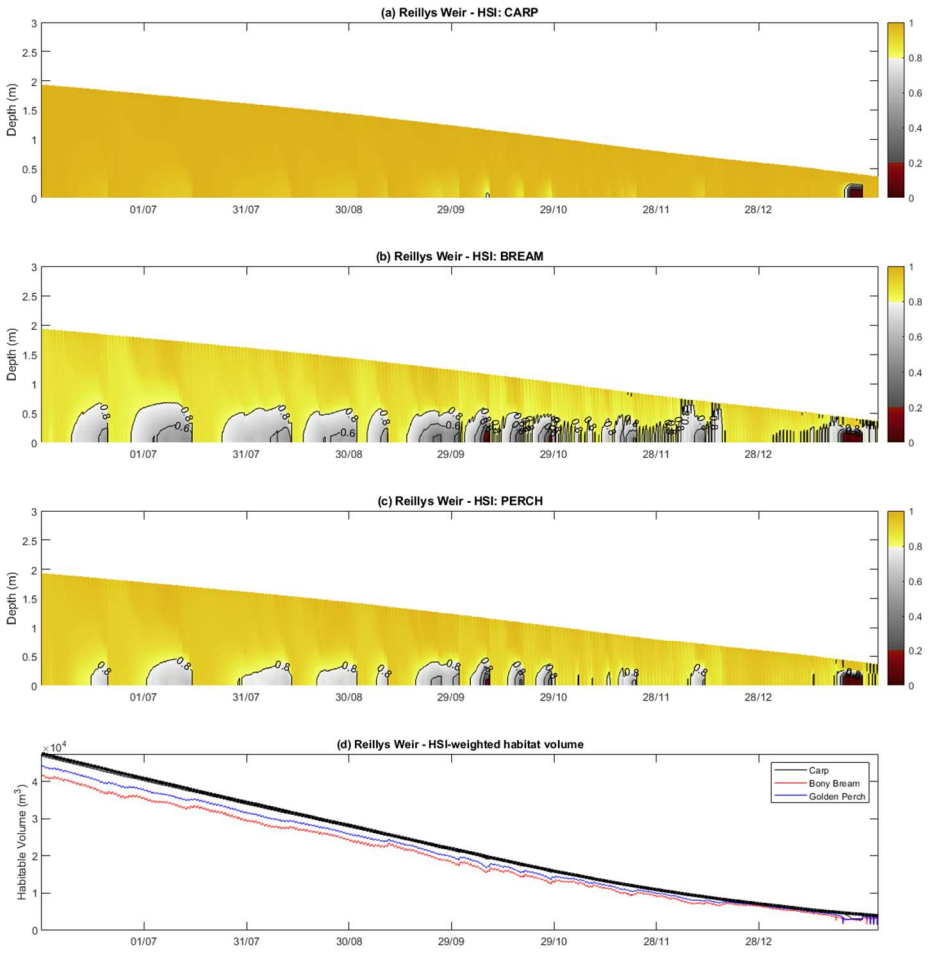

Figure 54: Habitat Suitability Index (HSI) and HSI-weighted habitat volume for common carp, bony bream and golden perch at Reilly's Weir in 2019 - 2020. A HSI value of 1 indicates optimal habitat conditions while 0 indicates unacceptable conditions. Black thick line in the bottom graph indicates total volume of water.

4. Climate change risk assessment

4.1. Introduction

Dryland rivers with non-perennial flow are widespread throughout the world's arid and semi-arid regions. These rivers have intermittent and highly unpredictable flow, often linked to highly irregular rainfall events (Acuña *et al*., 2014). In these systems, fish utilise remnant waterholes as refugia during drought periods in order to survive (Perry and Bond, 2009). As water levels recede during dry period, both the quantity and quality of habitat can decrease, sometimes with environmental conditions exceeding species tolerances (Sheldon *et al*., 2010).

Climate extremes over recent Australian summers have perpetrated mass fish kills, with graphic media coverage and widespread public and political concern. Crashes in dissolved oxygen concentrations have been implicated as causes of such fish kills, but our understanding of the role of oxygen dynamics of waterholes shaping the vulnerabilities of fishes in these systems remains limited.

We calibrated physical process models with detailed field measurements of oxygen profiles in representative waterholes during and after severe drought (Section 2). We also quantified critical oxygen concentration thresholds in relation to temperature for dominant native and exotic fishes (Section 3.2). Models and ecophysiology were combined to generate fish death risk models (Section 3.3 and 3.4) and these were used to simulate risks at one study site, Kooroon, under future climate. Results indicate risk drivers and highlight when and where mitigation is needed to prevent further catastrophic dryland river fish kills.

Anticipated changes in climate can impact on waterholes via a variety of mechanisms (Figure 55). In this section, the sensitivity of waterhole fish habitat is explored under climate change scenarios.

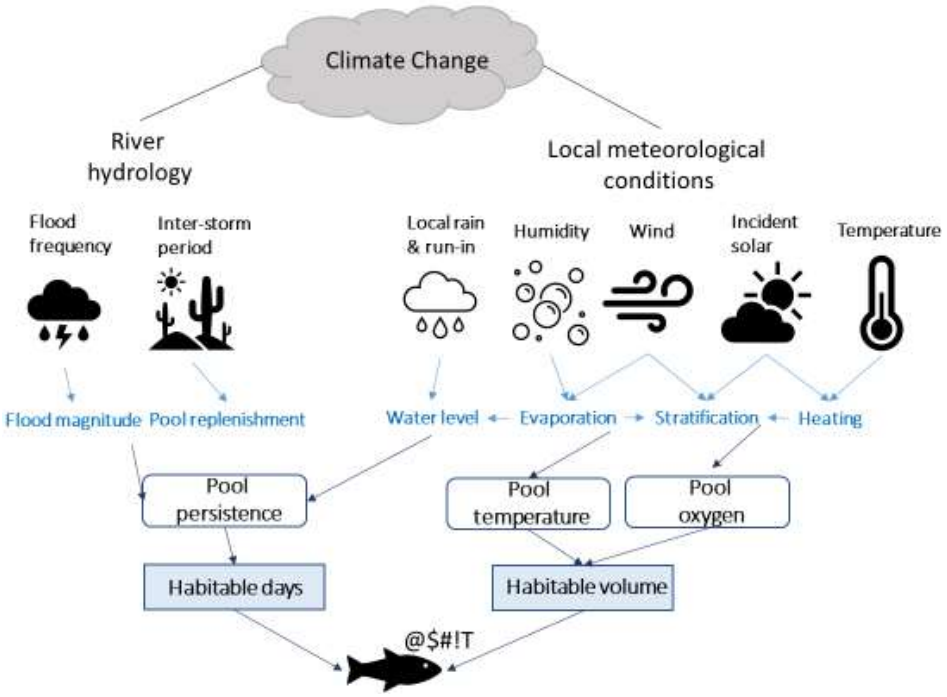

Figure 55: Conceptual diagram showing pathways where climate change may influence fish habitat quantity and quality in dryland river waterholes.

4.2. Climate change modelling approach

Gridded climate projection data were acquired from The Long Paddock website (https://www.longpaddock.qld.gov.au/qld-future-climate/dashboard), which includes mean air temperature, relative humidity, surface wind speed, solar radiation and precipitation from 1980 to 2099. The climate model outputs used in this study to illustrate the approach for waterhole risk assessment was ACCESS 1.0, and we chose the high Representative Concentration Pathway (RCP) 8.5.

Climate point data were extracted for Kooroon, and monthly mean percentage difference between the 20-year average of future (2080 – 2099) and current (2001 – 2020) was calculated for each climate variable, except wind speed where gridded data was unavailable. This percentage change in future climate was then applied to the current local climate at each pool to simulate temperature and oxygen concentrations, as well as habitat suitability index and habitable volume for each fish species. For wind speed, the seasonal absolute change projected for Moonie River Basin was applied as an offset in our model. Incoming longwave radiation was calculated using method described in Section 2, based on projected air temperature. Table 11 shows the factors applied to the current climate for Kooroon.

Table 11: Projected climate change in 2080 – 2099 relative to 2001 – 2020 under RCP 8.5 at Kooroon.

Month	Mean air temperature (%)	Relative humidity (%)	Shortwave radiation (%)	Rain (%)	Wind Speed (m/s)
1	12.3	7.9	-4.6	45.1	-0.1
2	11.3	9.6	-4.9	68.1	-0.1
3	14.2	1.8	4.5	8.4	-0.05
4	19.5	1.9	1.7	-7.2	-0.05
5	26.9	-3.6	4.7	-51.3	-0.05
6	28.7	-4.7	1.3	-23.1	0.044
7	33.9	-4.7	1.7	-22.9	0.044
8	29.4	-3.5	1.2	-18.5	0.044
9	24.4	-9.8	4.4	-52.7	0.11
10	23.3	-13.3	4.5	-20.2	0.11
11	18.4	2.8	-1.8	13.9	0.11
12	14.8	4.6	-3.3	26.0	-0.1

4.3. Climate change scenario results and discussion

Results suggest under RCP 8.5, water temperature will increase 2°C - 10°C at Kooroon by 2080 – 2099, with the most significant increase between June and November (Figure 56). In December and January, the entire water column may be above 30°C as water level decreases. The surface layer may reach

38°C, which is nearly at the upper limit of tolerance for some native species even if oxygen levels were optimal. Dissolved oxygen will increase near the surface but waterholes will remain hypoxic through much of their water column for most of the year (Figure 57). The resultant HSIs for both native and invasive species indicate a decline in habitat quality, particularly around the middle depth layers (Figure 58), likely as a result of the increase in temperature that cannot be compensated by the increase in oxygen levels. Consequently, habitable waterhole volume for all studied species is expected to decrease under future climate, with markedly increased risks of fish kill events as habitable volume falls to zero more frequently for native species during drought (Figure 59).

Overall, the results indicate that climate change increases fish-kill risks in ephemeral river waterholes typical of the Northern MDB. These results highlight the need for a mitigation strategy to improve habitat quality and reduce fish-kill risks in dryland rivers in the face of climate change. Although the current climate change study was only focused on one waterhole, Kooroon, this waterhole provided fish with above-average habitat condition among the six waterholes. Such fish-kill risks at Kurmala, for example, appear to be greater than at Kooroon. In addition, the current model considered only local-scale changes in climate in a snapshot of time, without accounting for cumulative effects on river hydrology (such as increase in drought duration and frequency) which will further reduce quantity and quality of habitat.

4.4. Next steps and recommendations for future work

The analysis in this section provides a conceptual framework for risk assessment and shows how the model approach can be used to ascertain the nature of future risks in dryland river waterholes. The results provide initial insights into the mechanisms by which climate change can amplify the existing risks of fish kills.

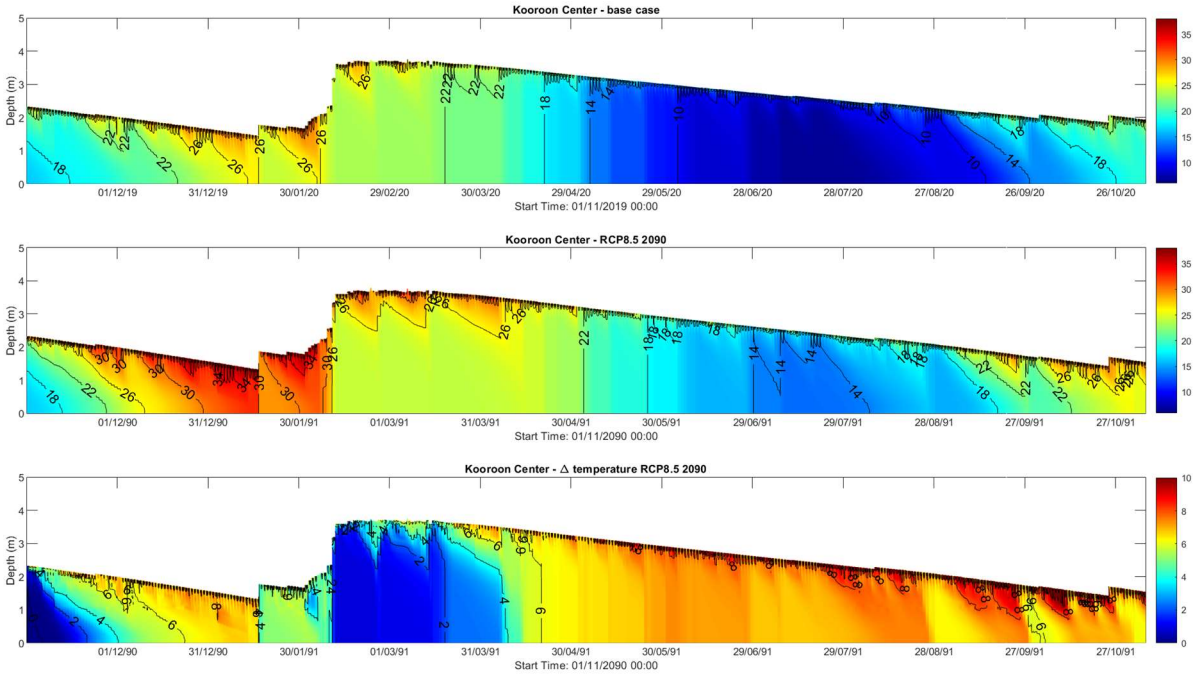

Figure 56: Comparison of water temperature between current climate (top), future climate (2080 – 2099) under RCP 8.5 (middle), and delta changes (bottom) at Kooroon.

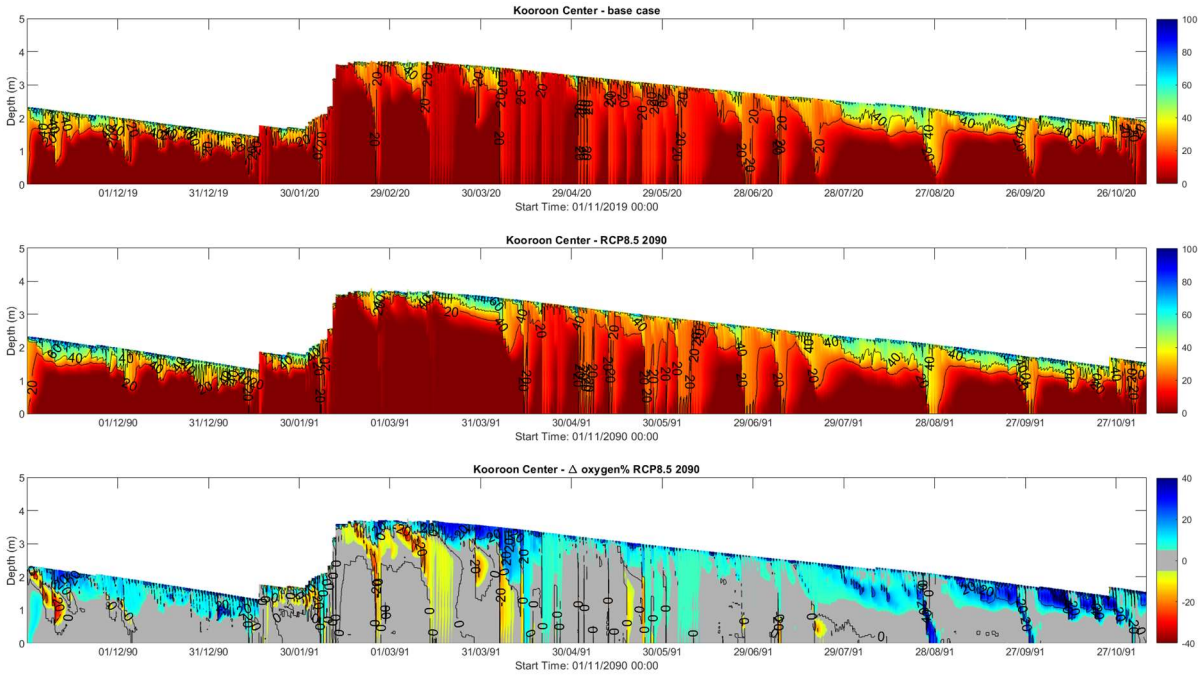

Figure 57: Comparison of oxygen percent saturation between current climate (top), future climate (2080 – 2099) under RCP 8.5 (middle), and delta changes (bottom) at Kooroon.

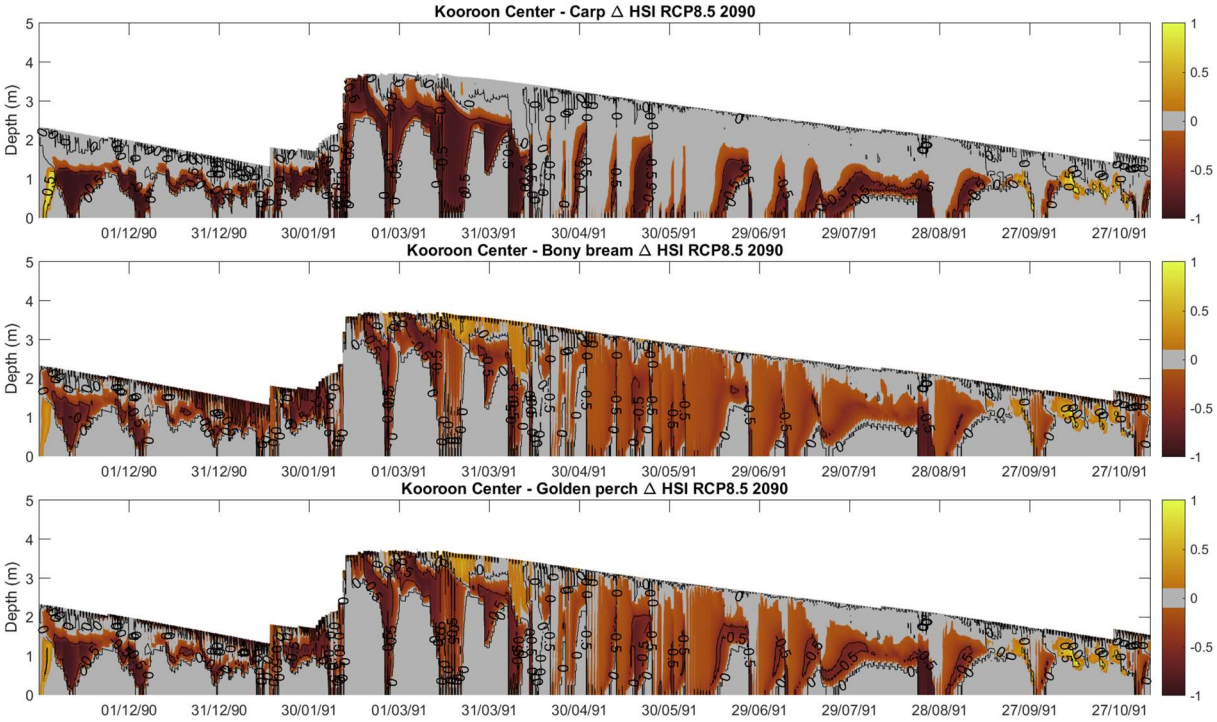

Figure 58: Delta changes in HSI between current climate and future climate (2080 – 2099) under RCP 8.5 at Kooroon waterhole for common carp, bony bream and golden perch. A value of -1 represents optimal habitat at present becoming unacceptable due to climate change, while a value of 0 represents no change in habitat quality.

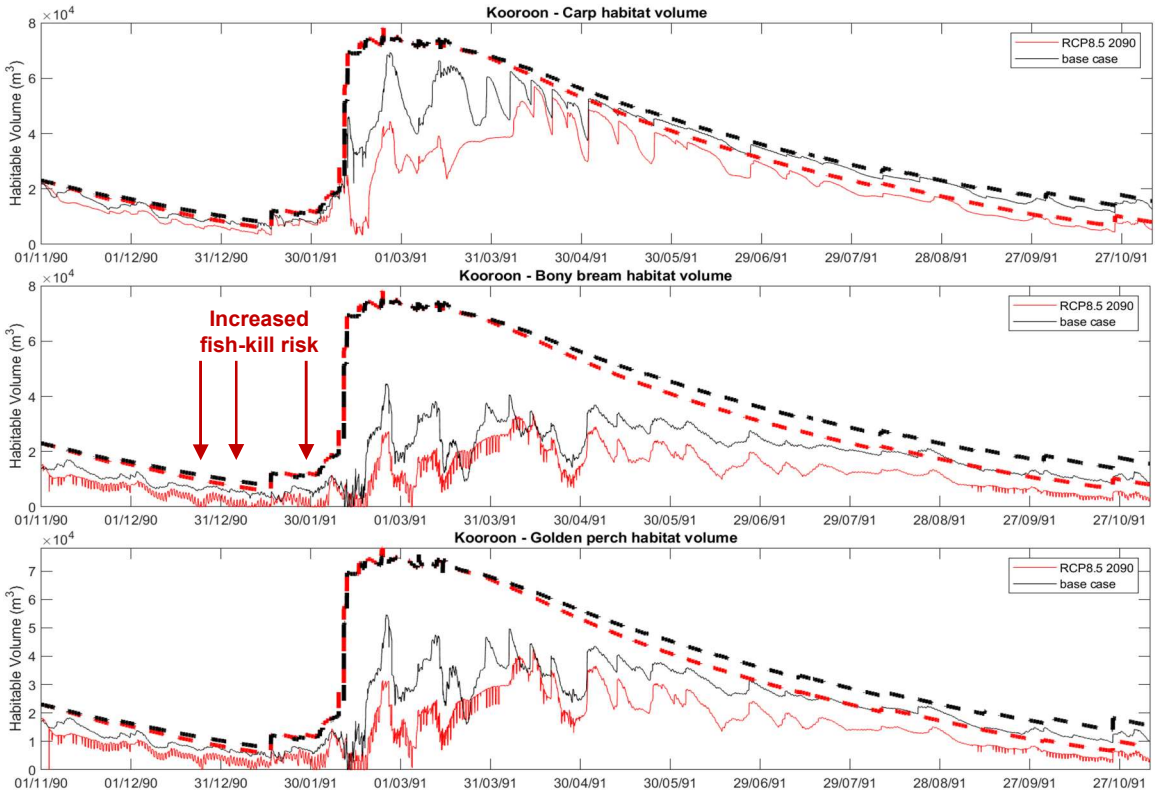

Figure 59: Comparison of HSI-weighted habitable volumes between current climate and future climate (2080 – 2099) under RCP 8.5 at Kooroon for common carp, bony bream and golden perch. Thick dashed lines indicate total volume of water.

We do not suggest these results reflect the exact conditions that would be experienced in the 2090's as obviously many other factors impacting catchment and river hydrology will impact upon waterhole persistence by that time. The results however do demonstrate that shifts in stratification phenology within waterholes brought about by a warming climate will only further stress fish communities by reducing habitable volumes compared to present conditions. The extent of the habitat reduction will depend on the specific trajectory of climate change that we follow, noting that in this study we have chosen the upper extreme scenario (RCP8.5) for illustrative purposes. As confidence in this model approach is further developed, it is recommended a more comprehensive climate change risk assessment could be undertaken, considering the range of plausible climate scenarios and addressing uncertainty in these projections using prediction ensembles and uncertainty analysis methodologies to better quantify future likely states.

Whilst this analysis is exploratory in nature, the results do importantly identify that, even if mass fish-kill events may be avoided by highly susceptible native species using avoidance behaviours, future climate conditions are very likely to overall favour common carp which are capable of tolerating high temperature and very low oxygen concentrations. Figure 59 suggests that climate change will have less of an impact impact on common carp's habitable volume through much of the year, especially during hot and dry periods, compared to native species that are more sensitive. The cumulative effect of this is that over time native species may struggle to maintain viable populations in their shrinking and/or degrading habitat, while common carp populations out-compete and dominate in these waterholes, resulting in a loss of biodiversity.

Perhaps one of the best options for helping native fish adapt to the increasing climate change risks, is carp management approaches that can successfully reduce the high carp biomass. These results show that carp management options that have the potential to increase anoxia in waterholes are likely to harm native fish (via their lower tolerance of anoxia than carp) and favour the survival of carp that have resisted the management intervention. The potential use of a lethal virus for carp biocontrol in these remote rivers is an example of a management option that is being considered by the National Carp Control Plan. With limited access and poor visibility due to high turbidity in remote waterholes, this creates a situation where there is little chance of successful dead carp biomass removal, and carp mortality events can further aggravate existing low oxygen conditions (Hipsey and Brookes, 2019). Managing carp in ways that could avoid any increase anoxia in these rivers is therefore recommended, and where possible build resilience in native populations by having restocking strategies in place after carp removal.

5. References

Abdel-Tawwab, M., Monier, M.N., Hoseinifar, S.H. and Faggio, C., 2019. Fish response to hypoxia stress: growth, physiological, and immunological biomarkers. *Fish Physiology and Biochemistry* 45, 997–1013.

Acuña V., Datry T., Marshall J., Barceló D., Dahm C.N. and Ginebreda A., 2014. Why should we care about temporary waterways? *Science*, 343, 1080–1081.

Aldous, A., Fitzsimons, J., Richter, B. and Bach L., 2011. Droughts, floods and freshwater ecosystems: evaluating climate change impacts and developing adaptation strategies. *Marine and Freshwater Research* 62, 223–231.

Baldwin, D.S., 2019. Stratification, mixing and fish deaths in the lower Darling River. Technical Report prepared for the Murray-Darling Basin Authority. 68 pp.

Bird R.E. and Hulstrom R.L., 1981. A Simplified Clear Sky Model for Direct and Diffuse Insolation on Horizontal Surfaces. SERI/TR-642-761, Solar Energy Research Institute, Golden, Colorado, USA.

Bennett, S., Duarte, C.M., Marbà, N. and Wernberg, T., 2019. Integrating within-species variation in thermal physiology into climate change ecology. *Philosophical Transactions of the Royal Society B: Biological Sciences* 374, 20180550.

Bond, N.R., Lake, P.S. and Arthington, A.H., 2008. The impacts of drought on freshwater ecosystems: an Australian perspective. *Hydrobiologia* 600, 3–16.

Bond, N.R., Balcombe, S.R., Crook, D.A., Marshall, J.C., Menke, N. and Lobegeiger, J.S., 2015. Fish population persistence in hydrologically variable landscapes. *Ecological Applications* 25, 901–913.

Bormans, M. and Webster, I.T., 1997. A mixing criterion for turbid rivers. *Environmental Modelling and Software* 12, 329–333.

Brookes, J. D. and Hipsey, M. R., 2019. Water quality risk assessment of carp biocontrol for Australian waterways. Technical Report for the Fisheries Research and Development Corporation. Environment Institute, University of Adelaide, Adelaide, South Australia.

Cengel, Y.A. and Özişik, M.N., 1984. Solar radiation absorption in solar ponds. *Solar Energy* 33, 581–591.

Christian D. and Sheng Y.P., 2003. Relative influence of various water quality parameters on light attenuation in Indian River Lagoon. *Estuarine Coastal and Shelf Science* 57, 961–971.

Claireaux, G. and Lefrançois, C., 2007. Linking environmental variability and fish performance: integration through the concept of scope for activity. *Philosophical Transactions of the Royal Society B* 362, 2031–2041.

Davie, A.W. and Pera, J.B., 2021. The Fish Health Risk Indicator: linking water quality and river flow data with fish health to improve our predictive capacity around fish death events. *Marine and Freshwater Research* 73, 193–199.

Davies P.M. 2002. Measures of benthic metabolism as indicators of ecological health of rivers and streams of the Condamine-Balonne and Maranoa catchments. Unpublished technical report.

Deutsch, C.A., Tewksbury, J.J., Huey, R.B., Sheldon, K.S., Ghalambor, C.K., Haak, D.C. and Martin, P.R. 2008. Impacts of climate warming on terrestrial ectotherms across latitude. *Proceedings of the National Academy of Sciences* 105: 6668–6672.

Dutil, J. D., Sylvestre, E. L., Gamache, L., Larocque, R. and Guderley, H., 2007. Burst-coast use, swimming performance, and metabolism of Atlantic cod (*Gadus morhua*) in sub-lethal hypoxic conditions. *Journal of Fish Biology* 71, 1–13.

Ern, R., 2019. A mechanistic oxygen- and temperature-limited metabolic niche framework. *Philosophical Transactions of the Royal Society B: Biological Sciences* 374, 20180540.

Ern, R., Norin, T., Gamperl, A.K. and Esbaugh, A.J., 2016. Oxygen dependence of upper thermal limits in fishes. *The Journal of Experimental Biology* 219, 3376–3383.

Garner, G., Malcolm, I.A., Sadler, J.P. and Hannah, D.M., 2017. The role of riparian vegetation density, channel orientation and water velocity in determining river temperature dynamics. *Journal of Hydrology* 553, 471–485.

Gleiss, A., Lear, L., Morgan, D. and Hipsey, M.R., 2021. A description of the surface water hydrology of dry-season refuge pools in the Fitzroy River, Western Australia. Harry Butler Institute Technical Report prepared for the WA Department of Water and Environmental Management.

Hamilton, D.P. and Schladow, S.G., 1997. Prediction of water quality in lakes and reservoirs. Part I—Model description. *Ecological Modelling* 96, 91–110.

Hipsey, M. R., and Sivapalan, M. 2003. Parameterizing the effect of a wind shelter on evaporation from small water bodies, *Water Resources Research* 39, 1339.

Hipsey, M.R., Bruce, L.C., Boon, C., Busch, B., Carey, C.C., Hamilton, D.P., Hanson, P.C., Read, J.S., de Sousa, E., Weber, M. and Winslow, L.A., 2019. A General Lake Model (GLM 3.0) for linking with high-frequency sensor data from the Global Lake Ecological Observatory Network (GLEON). *Geoscientific Model Development* 12, 473–523.

Hodges, B., 1998. Heat budget and thermodynamics at a free surface: some theory and numerical implementation (revision 1.0 c) ED 1300 BH. Centre for Water Research Technical Report, University of Western Australia.

Imberger, J. and Patterson, J.C., 1981. A dynamic reservoir simulation model-DYRESM:5. In: H.B. Fischer (ed.), Transport Models for Inland and Coastal Waters. Academic Press, New York: 310-361.

Kimball, B., Idso, S. and Aase, J., 1982. A model of thermal radiation from partly cloudy and overcast skies. *Water Resources Research* 18, 931–936.

King, A. J., Tonkin, Z. and Lieshcke, J., 2012. Short-term effects of a prolonged blackwater event on aquatic fauna in the Murray River, Australia: Considerations for future events, *Marine and Freshwater Research* 63(7), 576–586.

Kirk, J.T.O., 1994. Light and photosynthesis in aquatic ecosystems. Cambridge University Press.

Knighton, A. D., and Nanson, G.C., 2000. Waterhole Form and Process in the Anastomosing Channel System of Cooper Creek, Australia. *Geomorphology* 35, 101–117.

Liu, J., Wang, B., Oldham, C.E. and Hipsey, M.R., 2020. Unravelling the metabolism black-box in a dynamic wetland environment using a hybrid model framework: Storm driven changes in oxygen budgets. *Science of The Total Environment* 723, 138020.

Maier, H.R., Burch, M.D. and Bormans, M., 2001. Flow management strategies to control blooms of the cyanobacterium, *Anabaena circinalis*, in the River Murray at Morgan, South Australia. *River Research and Applications* 17, 637–650

Markfort, C.D., Perez, A.L.S., Thill, J.W., Jaster, D.A., Porte-Agel, F. and Stefan, H.G., 2010. Wind sheltering of a lake by a tree canopy or bluff topography. *Water Resources Research* 46, W03530.

Marshall, J.C., Menke, N., Crook, D.A., Lobegeiger, J.S., Balcombe, S.R., Huey, J.A. et al., 2016. Go with the flow: the movement behaviour of fish from isolated waterhole refugia during connecting flow events in an intermittent dryland river. *Freshwater Biology* 61, 1242–1258.

Marshall, J.C., Lobegeiger, J.S. and Starkey, A., 2021. Risks to fish populations in dryland rivers from the combined threats of drought and instream barriers. *Frontiers in Environmental Science* 9, 671556.

Mcgregor, G.B., Marshall, J.C., Lobegeiger, J.S., Holloway, D., Menke, N. and Coysh, J., 2018. A risk-based ecohydrological approach to assessing environmental flow regimes. *Environmental Management* 61, 358–374.

McJannet, D., Hawdon, A., Van Niel, T., Boadle, D., Baker, B., Trefry, M. and Rea, I., 2017. Measurements of evaporation from a mine void lake and testing of modelling approaches. *Journal of Hydrology* 555, 631–647.

McNeil, D.G. and Closs, G.P., 2007. Behavioural responses of a south-east Australian floodplain fish community to gradual hypoxia. *Freshwater Biology* 52, 412–420.

MDBA, 2019. Climate change and the Murray–Darling Basin Plan.

Monin, A.S. and Obukhov, A. M., 1954. Basic laws of turbulent mixing in the atmosphere near the ground. *Jr. Akad. Nauk SSSR Geofiz. Inst*. 24, 163–187.

Negus, P.M. et al., 2019. Queensland's eastern Murray-Darling riverine ecosystems: Threats and condition, Q-catchments Technical Report. Brisbane.

Perry G.L. and Bond N.R., 2009. Spatially explicit modeling of habitat dynamics and fish population persistence in an intermittent lowland stream. *Ecological Applications* 19, 731– 746.

Pittock, J. and Finlayson, C.M., 2011. Australia's Murray–Darling Basin: freshwater ecosystem conservation options in an era of climate change. *Marine and Freshwater Research* 62, 232–243.

Portner, H.O. and Peck, M.A., 2010. Climate change effects on fishes and fisheries: towards a cause-and-effect understanding. *Journal of Fish Biology* 77, 1745–1779.

Poulsen, S.B., Jensen, L.F., Nielsen, K.S., Malte, H., Aarestrup, K. and Svendsen, J.C., 2011. Behaviour of rainbow trout Oncorhynchus mykiss presented with a choice of normoxia and stepwise progressive hypoxia. *Journal of Fish Biology* 79, 969–979.

Riley, J.P. and Skirrow, G. (eds), 1975. Chemical Oceanography. Academic Press, London.

Rubalcaba, J.G., Verberk, W.C., Hendriks, A.J., Saris, B. and Woods, H.A., 2020. Oxygen limitation may affect the temperature and size dependence of metabolism in aquatic ectotherms. *Proceedings of the National Academy of Sciences* 117, 31963–31968.

Sheldon F., Bunn S.E., Hughes J.M., Arthington A.H., Balcombe S.R. and Fellows C.S., 2010. Ecological roles and threats to aquatic refugia in arid landscapes: dryland river waterholes. *Marine and Freshwater Research* 61, 885– 895.

Steffensen, J. F., 2006. Oxygen consumption of fish exposed to hypoxia: are they all oxyregulators or are any oxyconformers? In Fish Physiology, Toxicology, and Water Quality. Proceedings of the Ninth International Symposium, Capri, Italy (Brauner, C. J., Suvajdzic, K., Nilsson, G. and Randall, D., eds), pp. 239–250. Athens, GA: Ecosystems Research Division

Strub, P. T. and Powell, T. M., 1987. Surface temperature and transport in Lake Tahoe: inferences from satellite (AVHRR) imagery. *Cont. Shelf Res*. 7, 1001–1013.

Vaquer-Sunyer, R. and Duarte, C.M., 2008. Thresholds of hypoxia for marine biodiversity. *Proceedings of the National Academy of Sciences* 105, 15452–15457.

Vertessy, R., Barma, D., Baumgartner, L., Mitrovic, S., Sheldon, F. & Bond, N. 2019. Independent Assessment of the 2018-19 fish deaths in the lower Darling: Final Report.

Vilas, M.P., Marti, C.L., Oldham, C.E. and Hipsey, M.R., 2018. Macrophyte-induced thermal stratification in a shallow urban lake promotes conditions suitable for nitrogen-fixing cyanobacteria. *Hydrobiologia* 806, 411–426.

Wallace, J., Waltham, N., Burrows, D. and McJannet, D., 2015. The temperature regimes of dry season waterholes in tropical northern Australia: potential impacts on fish refugia. *Freshwater Science* 34, 663–678.

Wallace, J., Waltham, N., and Burrows, D., 2017. A comparison of temperature regimes in dry-season waterholes in the Flinders and Gilbert catchment in northern Australia. *Marine and Freshwater Research* 68, 650–667.

Waltham N., Burrows, D., Butler, B., Wallace, J., Thomas, C., James, C. and Brodie, J., 2013. Waterhole ecology in the Flinders and Gilbert catchments. A technical report to the Australian Government from the CSIRO Flinders and Gilbert Agricultural Resource Assessment, part of the North Queensland Irrigated Agriculture Strategy. CSIRO Water for a Healthy Country and Sustainable Agriculture flagships, Australia.

Wanninkhof, R., 1992. Relationship between wind speed and gas exchange over the ocean. *Journal of Geophysical Research: Oceans* 97, 7373–7382.

Webb, B. W. and Zhang, Y., 1997. Spatial and seasonal variability in the components of the river heat budget. *Hydrological Processes* 11, 79–101.

Woolway, R. I., Verburg, P., Merchant, C. J., Lenters, J. D., Hamilton, D. P., Brookes, J., Kelly, S., Hook, S., Laas, A., Pierson, D. and Rimmer, A., 2017. Latitude and lake size are important predictors of over-lake atmospheric stability, *Geophysical Research Letters* 44, 8875–8883.

6. Appendix - General Lake Model performance assessment

The following plots show the correlation and distributional comparison between the model and data. Table A1 summarises the model error metrics for the different simulations reported in Section 2.

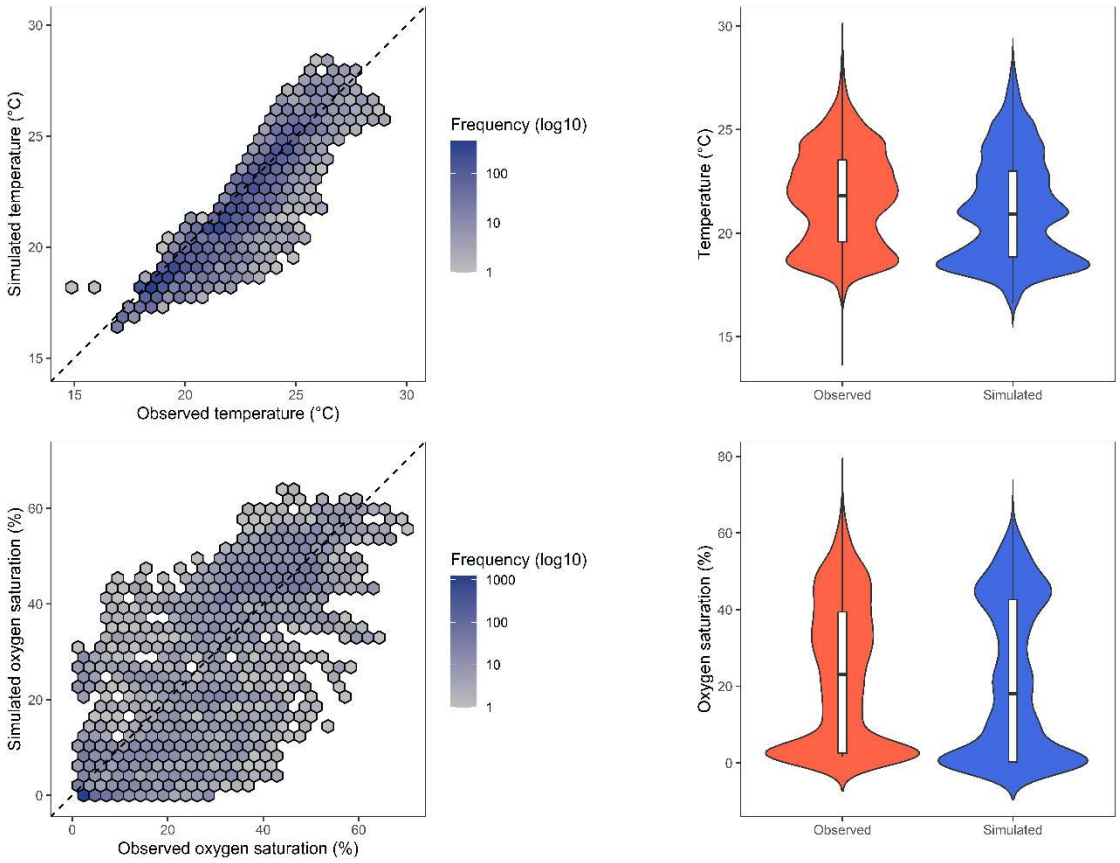

Figure A1. Hexagonal bin plot (left) and violin plot (right) for modelled and field data at Kooroon during calibration period (1/11/2019 - 31/12/2019).

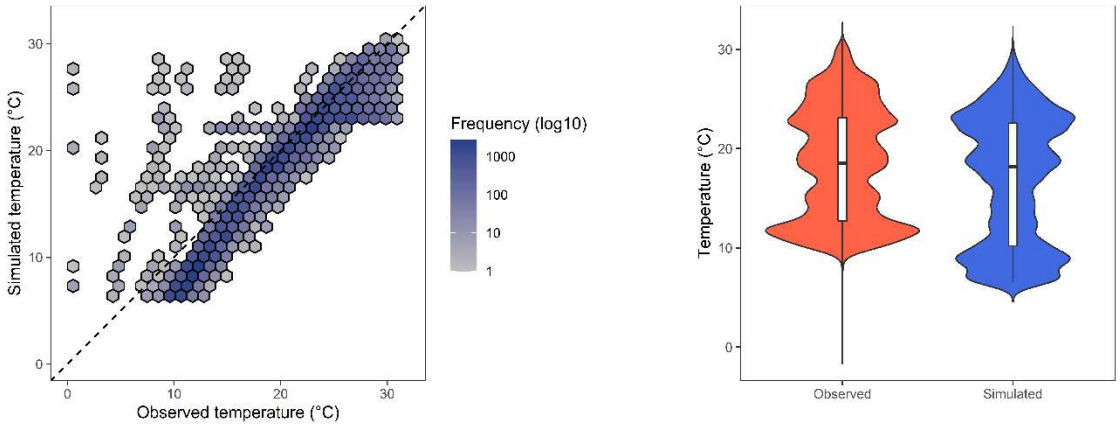

Figure A2. Hexagonal bin plot (left) and violin plot (right) for modelled and field data at Kooroon during calibration and validation period (1/11/2019 - 5/11/2020).

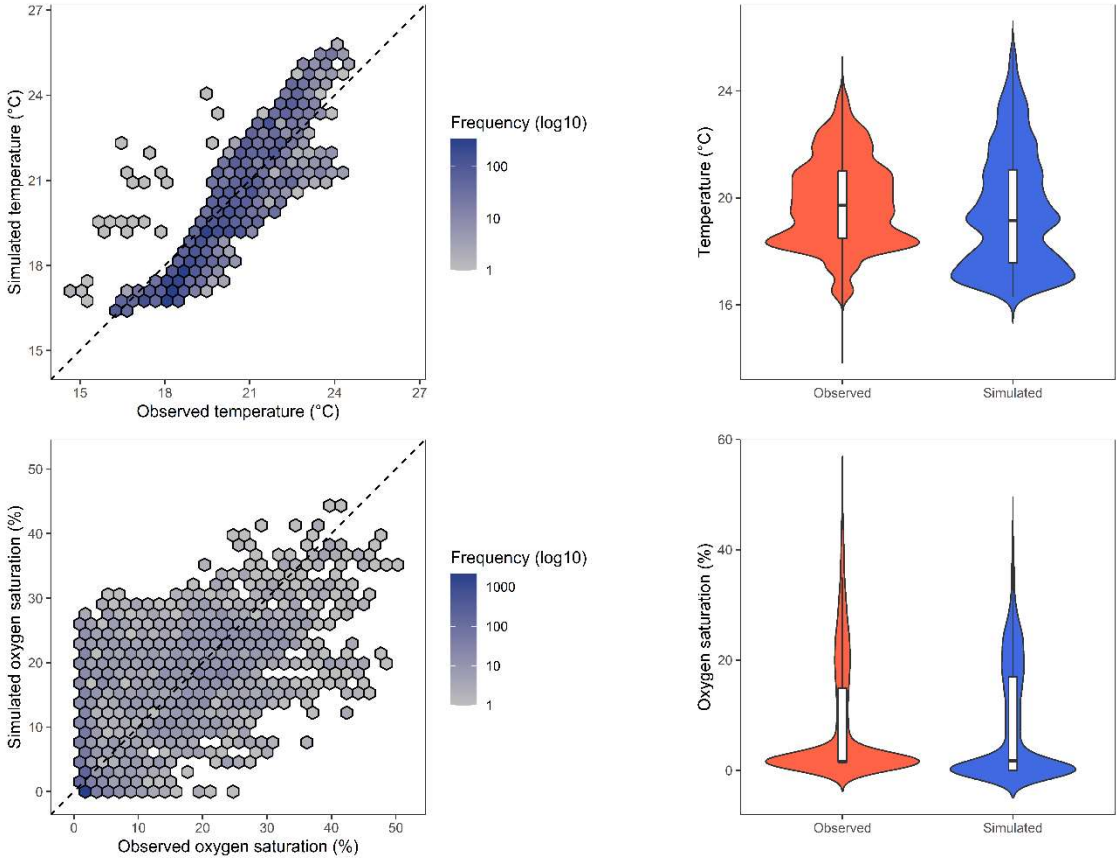

Figure A3. Hexagonal bin plot (left) and violin plot (right) for modelled and field data at Kurmala during calibration period (1/11/2019 - 31/12/2019).

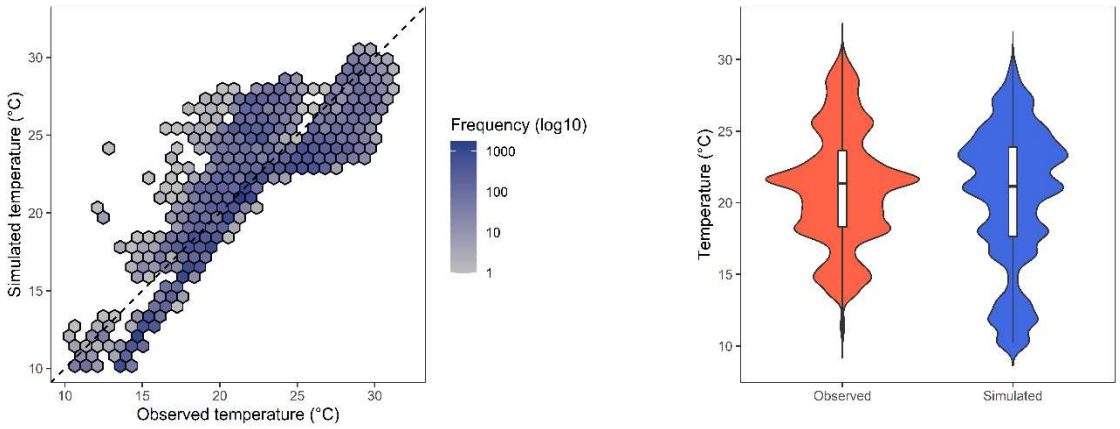

Figure A4. Hexagonal bin plot (left) and violin plot (right) for modelled and field data at Kurmala during calibration validation period (1/11/2019 - 1/6/2020).

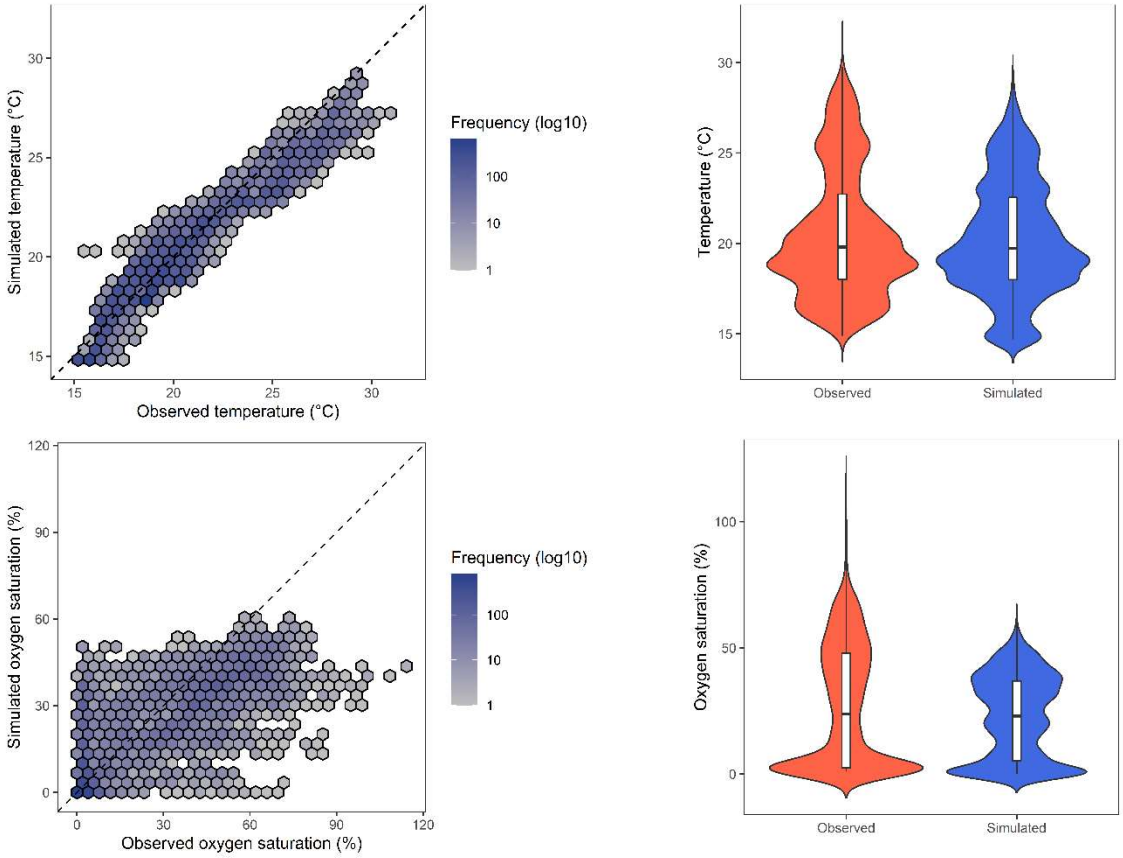

Figure A5. Hexagonal bin plot (left) and violin plot (right) for modelled and field data at Brenda during calibration period (1/10/2019 - 31/1/2020).

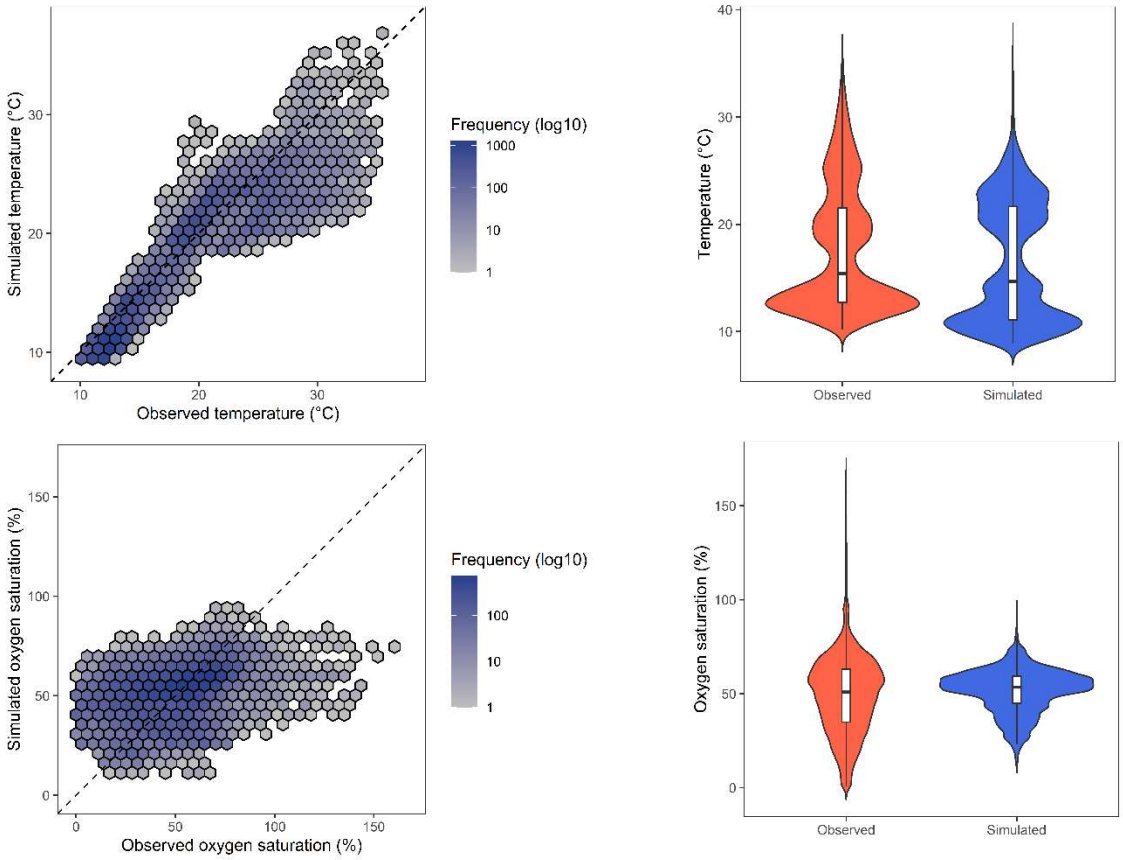

Figure A6. Hexagonal bin plot (left) and violin plot (right) for modelled and field data at Reilly's Weir during calibration period (1/6/2019 - 1/2/2020).

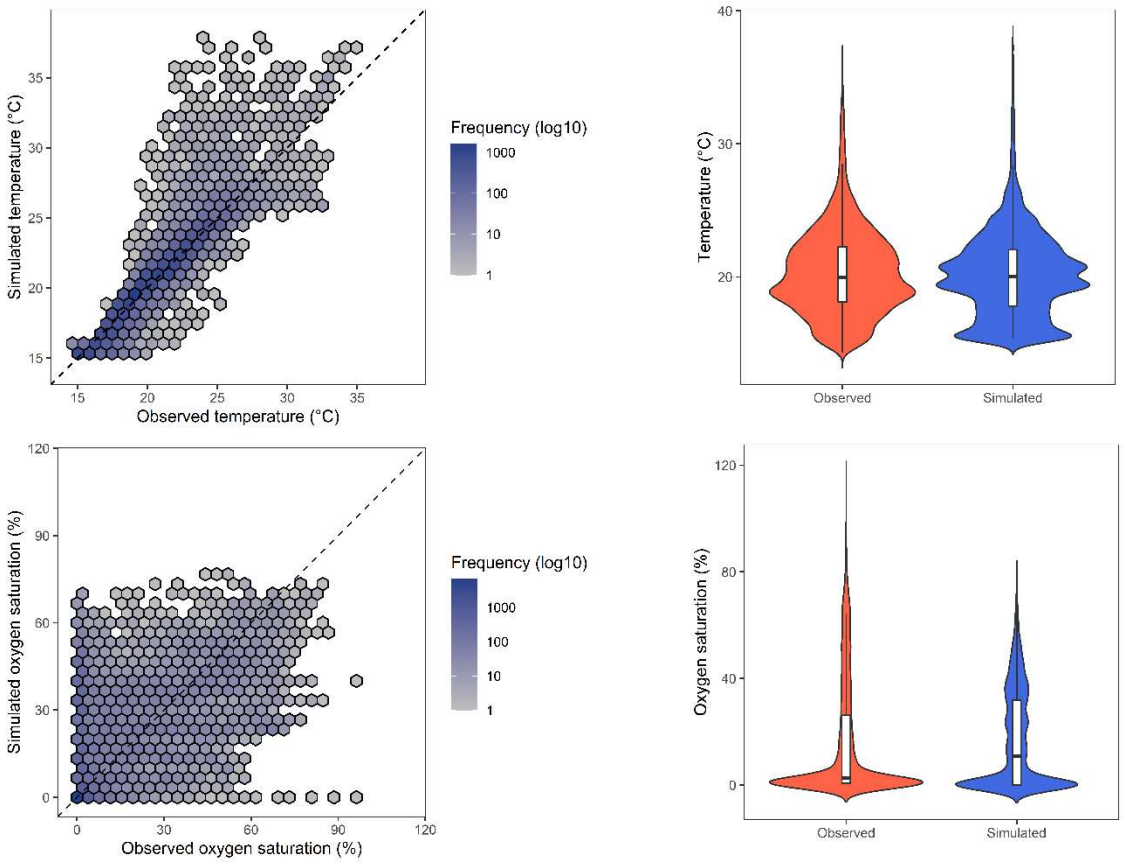

Figure A7. Hexagonal bin plot (left) and violin plot (right) for modelled and field data at Weribone during calibration period (1/10/2019 - 1/1/2020).

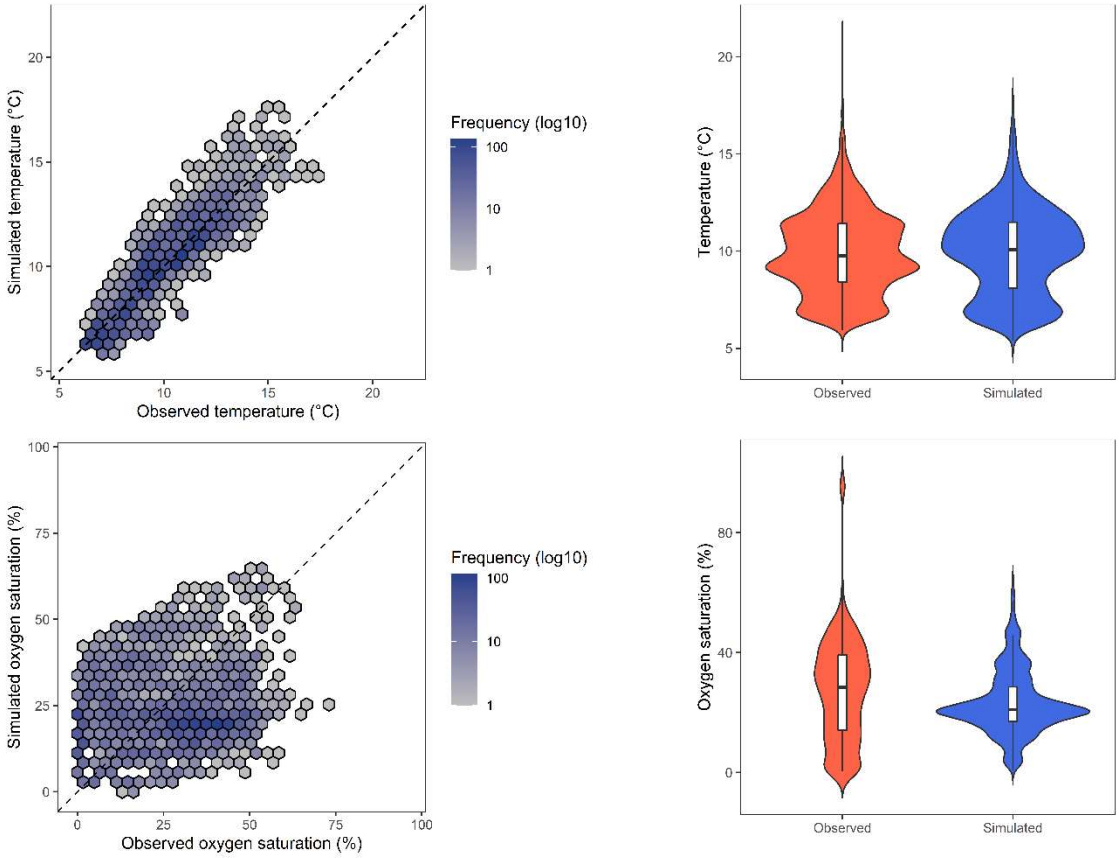

Figure A8. Hexagonal bin plot (left) and violin plot (right) for modelled and field data at Trafalgar during calibration period (15/6/2019 - 22/7/2019).

Table A1. Correlation coefficients (R) between modelled and field data at six waterholes.

	Water level	Temperature	Oxygen
Kooroon	0.995	0.94	0.85
Kooroon long-term	0.82	0.97	-
Kurmala	0.995	0.92	0.77
Kurmala long-term	0.81	0.88	-
Brenda	0.99	0.96	0.76
Reilly's Weir	0.99	0.94	0.37
Weribone	0.998	0.94	0.58
Trafalgar	0.999	0.92	0.13